CHALMERS

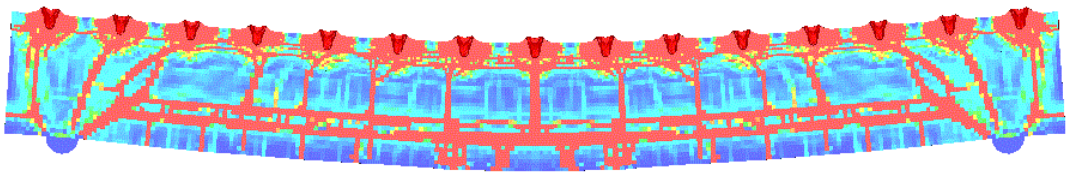

Concrete Structures Subjected to Blast and Fragment Impacts

Numerical Simulations of Reinforced and Fibre-reinforced Concrete

ULRIKA NYSTRÖM

Department of Civil and Environmental Engineering
Division of Structural Engineering, Concrete Structures
CHALMERS UNIVERSITY OF TECHNOLOGY
Göteborg, Sweden 2008

THESIS FOR THE DEGREE OF LICENTIATE OF ENGINEERING

Concrete Structures Subjected to Blast and Fragment Impacts

Numerical Simulations of Reinforced and Fibre-reinforced Concrete

ULRIKA NYSTRÖM

Department of Civil and Environmental Engineering
Division of Structural Engineering, Concrete Structures
CHALMERS UNIVERSITY OF TECHNOLOGY
Göteborg, Sweden 2008

Concrete Structures Subjected to Blast and Fragment Impacts
Numerical Simulations of Reinforced and Fibre-reinforced Concrete
ULRIKA NYSTRÖM

ISSN 1652-9146
Lic 2008:4
Department of Civil and Environmental Engineering
Division of Structural Engineering, Concrete Structures
Chalmers University of Technology
SE-412 96 Göteborg
Sweden
Telephone: + 46 (0)31-772 1000

Cover:
Numerical simulation result of wall-strip response when subjected to combined blast and fragment loading.

Chalmers Reproservice
Göteborg, Sweden 2008

Concrete Structures Subjected to Blast and Fragment Impacts
Numerical Simulations of Reinforced and Fibre-reinforced Concrete

ULRIKA NYSTRÖM
Department of Civil and Environmental Engineering
Division of Structural Engineering, Concrete Structures
Chalmers University of Technology

ABSTRACT

Concrete is widely used in design of protective structures due to its good energy-absorbing characteristics under high pressures and, when properly reinforced, ductile behaviour. Nevertheless, the response of concrete structures subjected to severe dynamic loading differs from their static behaviour, on a structural level but also on a material level. The addition of steel fibres in the concrete may improve the energy-absorbing characteristics of plain concrete, which is especially true for the tensile behaviour. The fracture energy for steel-fibre reinforced concrete may be many times higher already for low dosages of fibres compared to plain concrete.

In design of protective structures it is important to identify the possible threats and their risk of occurrence to be able to characterise the design loads. Often this involves the effects of cased charges, i.e. combined blast and fragment loading. While the structural behaviour for blast load and single fragment impacts is relatively well understood, the response under combined loading, including the blast and multiple impacts of fragments, is not yet clear.

The theoretical bases for concrete material behaviour, weapon load characteristics, and their effect on the structural response are treated in this licentiate thesis. In addition, three numerical studies are presented, whose aim is to increase the understanding of impact and impulsive loading and the subsequent response of a concrete element. The first numerical study was a comparative investigation of the relative effect on the impact resistance when adding steel fibres to concrete. It was concluded that the depth of penetration of the striking projectile was only slightly influenced by the addition of fibres, while the sizes of the front- and rear-face craters were decreased. The second numerical study involved combined blast and fragment loading of a reinforced concrete wall strip, and it was seen that the total damage of the wall strip subjected to the combined loads was highly related to the damage caused by the fragment impact alone. Furthermore, the mid-point deflection in combined loading was larger than the sum of mid-point deflections in blast and fragment loading, indicating synergetic effects of the two loads. In the third numerical study the effect of reinforcement on the projectile impact resistance was studied. It was concluded that the presence of reinforcement may improve the impact resistance of the concrete if a suitable reinforcement detailing is used.

Key words: Concrete, weapon effects, blast wave, fragment impact, numerical simulations, fibre-reinforced concrete, reinforced concrete, SDOF

Stötvågs- och Splitterbelastade Betongkonstruktioner
Numeriska Simuleringar av Armerad och Fiberarmerad Betong
ULRIKA NYSTRÖM
Institutionen för bygg- och miljöteknik
Avdelningen för konstruktionsteknik, betongbyggnad
Chalmers tekniska högskola

SAMMANFATTNING

Betong är, tack vare sin höga energiabsorberande förmåga vid höga tryck, samt vid lämplig utformad armering, sega beteende, ett vida använt material inom byggandet av skyddande konstruktioner. Vid extrem dynamisk belastning skiljer sig dock beteendet hos betongen, på såväl konstruktions- som materialnivå, jämfört med beteendet vid statisk belastning. Vid tillförsel av stålfibrer i betong ökar dess energiabsorberande förmåga, vilket är speciellt tydligt i drag. Brottenergin för stålfiberarmerad betong kan redan vid låga fiberdoser vara flerfaldigt gånger högre för en stålfiberarmerad betong än för motsvarande betong utan fibrer.

Vid dimensionering av skyddskonstruktioner är det viktigt att identifiera möjliga hot för att kunna karaktärisera det avgörande lastfallet. Ofta involverar dessa hot explosioner av höljda laddningar, vilka resulterar i en kombinerad belastning av stötvåg och splitter. Medan beteendet hos betongkonstruktioner utsatta för stötvågsbelastning eller enskilda splitter är relativt välkänt är kunskapen om kombinerad belastning av stötvåg och splittersvärm ännu oklar.

Den teoretiska grunden för betongens materialbeteende, karaktäristiska vapenlaster och deras verkan på konstruktioner behandlas i sammanläggningssdelen i denna licentiatuppsats. Därtill presenteras tre numeriska studier vars syfte är att öka förståelsen för stöt- och impulsintensiva belastningar. Den första numeriska studien var en jämförande studie av vilken relativ inverkan som tillsatts av stålfibrer i betong har på dess motståndsförmåga mot projektilbelastning. Det kunde konstateras att inträngningsdjupet var relativt opåverkat av fibertillsättningen medan kraterstorleken, på både fram och baksidan av den beskjutna kroppen, minskade. I den andra studien undersöktes responsen hos en armerad betongväggsstrimla vid kombinerad belastning av stötvåg och splitter. Det kunde konstateras att den totala skadan i väggelementet var starkt relaterat till skadan orsakad av enbart splitterbelastningen. Vidare framgick att väggstrimlans mittnedböjning var större för det kombinerade lastfallet än för den sammanlagda nedböjningen orsakad av stötvågs- respektive splitterbelastningarna separat. Detta tyder på att det finns en synergieffekt för de kombinerade lasterna. I den tredje studien undersöktes armeringens inverkan på betongens motståndsförmåga vid projektilbeskjutning. Slutsatsen drogs att armeringen kan ha viss betydelse för detta motstånd förutsatt att armeringen är lämpligt inlagd.

Nyckelord: Betong, vapenverkan, stötvåg, splitter, numeriska studier, fiberarmerad betong, armerad betong, SDOF

LIST OF PUBLICATIONS

This thesis is based on the work contained in the following papers, referred to by Roman numerals in the text. In the case of more than one author, the contributions from the authors to the work are given for each paper.

I. Nyström, U. and Gylltoft, K. (2008): Comparative numerical studies of projectile impacts on plain and steel-fibre reinforced concrete. Submitted to *International Journal of Impact Engineering* in April 2008.

   Work done by Nyström, U., supervised by Gylltoft, K.

II. Nyström, U. and Gylltoft, K. (2008): Numerical studies of the combined effects of blast and fragment loading. Submitted to *International Journal of Impact Engineering* in April 2008.

   Work done by Nyström, U., supervised by Gylltoft, K.

One conference paper has also been written within the frame of this work and is referred to as Conference Paper.

Nyström, U. and Leppänen, J. (2006): Numerical Studies of Projectile Impacts on Reinforced Concrete. *Proceedings of the 2nd International Conference on Design and Analysis of Protective Structures 2006*, 13-15 November, 2006, Singapore, pp. 310-319.

Work done by Nyström, U., supervised by Leppänen, J.

Contents

PAPER I – PAPER II

I. Nyström, U. and Gylltoft, K. (2008): Comparative numerical studies of projectile impacts on plain and steel-fibre reinforced concrete. Submitted to *International Journal of Impact Engineering* in April 2008. 15 pp.

II. Nyström, U. and Gylltoft, K. (2008): Numerical studies of the combined effects of blast and fragment loading. Submitted to *International Journal of Impact Engineering* in April 2008. 16 pp.

CONFERENCE PAPER

Nyström, U. and Leppänen, J. (2006): Numerical Studies of Projectile Impacts on Reinforced Concrete. *Proceedings of the 2nd International Conference on Design and Analysis of Protective Structures 2006*, 13-15 November, 2006, Singapore, pp. 310-319.

Preface

The work presented in this licentiate thesis was carried out between March 2006 and April 2008 at Chalmers University of Technology, at the Department of Civil and Environmental Engineering, Division of Structural Engineering, Concrete Structures. The work was performed within the research project “Dynamic behaviour of concrete structures subjected to blast and fragments” and is a continuation of earlier work on concrete structures subjected to severe dynamic loading conducted at Chalmers University of Technology by Morgan Johansson and Joosef Leppänen. The project is financially supported by the Swedish Rescue Services Agency.

I would like to thank my supervisor and examiner, Prof. Kent Gylltoft, for his guidance, for the valuable discussions and for his understanding and kind heart. Further, I would like to thank my assistant supervisors, Dr. Morgan Johansson and Dr. Joosef Leppänen, for sharing their knowledge and giving valuable advice with great willingness to help. I would also like to extend my appreciation to M.Sc. Björn Ekengren from the Swedish Rescue Services Agency, not only for his valuable contribution to the work, but also for his words of wisdom about life and its school.

My colleagues at Structural Engineering, and especially Concrete Structures, are thanked for their support, patience and warming smiles.

Finally, I thank my family for always being there, the princess Aurelie for giving joy and Philip for bringing my hidden strengths to the surface.

Göteborg, April 2008

Ulrika Nyström

Notations

Roman upper case letters

A	Shape factor for failure surface in RHT material model
B	Shape factor for residual strength surface in RHT material model
B_x	Mott explosive constant
B_0, B_1	Material factors describing shape of curve in *P-α EOS*
C	Damping coefficient
C_L	Confidence level
D	Damage factor
D_1, D_2	Material parameters in expression for plastic failure strain
$\sqrt{2E}$	Gurney constant
F_{Rate}	Describing strain-rate dependence in RHT material model
G_F	Fracture energy
K	Stiffness
K_1, K_2, K_3	Material factors describing shape of curve in *P-α EOS*
L	Length of test specimen or structural element
L_f	Fibre length
M	Mass
M_A	Fragment distribution factor
M_{Rd}	Moment capacity
M_1	Shape factor for residual strength surface in RHT material model
N	Shape factor for failure surface in RHT material model
N_f	Total number of fragments with mass larger than m_f
$P(t)$	Pressure/force as a function of time
P^+	Peak overpressure
P^-	Negative pressure
$P_r^+,\ P_s^+$	Reflected and incident peak overpressure, respectively
P_0	Ambient pressure
R	Internal resistance force
R_f	Fragment travel distance
R_m	Maximum internal resistance force
$R_3(\theta)$	Describing third invariant dependence in deviatoric section
T^+	Duration of positive phase in pressure-time relation for blast load
T^-	Duration of negative phase in pressure-time relation for blast load
V_f	Volume fraction of fibres
W	Weight of explosive
W_c	Weight of bomb casing
W_f	Weight of design fragment
Y	Yield strength
Y_{el}	Elastic limit surface in RHT material model
Y_{fail}	Failure surface in RHT material model
Y_{fric}	Residual strength surface in RHT material model
Y_{TXC}	Compressive meridian in *Y-p* relation in RHT material model

Roman lower case letters

a_1	Initial slope of bi-linear crack-softening relation for FRC
a_2	Slope of second branch in bi-linear crack-softening relation for FRC
b_2	Intersection of the second branch with the y-axis in bi-linear crack-softening relation for FRC
d_i	Average inside diameter of casing
e	Internal energy
f_c	Concrete compressive strength
f_s	Concrete shear strength
f_t	Concrete tensile strength
$f_{t.dyn}$	Dynamic concrete tensile strength
$f_{t.static}$	Static concrete tensile strength
i^+	Impulse intensity for positive phase in pressure-time relation for blast load
i^-	Impulse intensity for negative phase in pressure-time relation for blast load
l_{el}	Length over which crack is smeared
m_f	Fragment mass
n	Shape factor in *P-α EOS*
n_{fibres}	Number of fibres per cm^2
p	Hydrostatic pressure
$p_{compaction}$	Hydrostatic pressure for which the compaction of the material starts
p_{HTL}	Hydrostatic tensile limit
p_{solid}	Hydrostatic pressure for which the material is fully compacted
t	Time
t_a	Time of arrival
t_c	Average casing thickness
u	Displacement
$\dot{u}$	Velocity
$\ddot{u}$	Acceleration
u_{el}	Maximum elastic displacement
v_{sf}	Fragment velocity at certain distance
v_0	Initial velocity of fragments
w	Crack opening
w_c	Critical crack opening

Greek letters

α	Adjusting factor for pressure decay of blast load
$\alpha_{current}$	Current porosity of material
α_{porous}	Porosity of undamaged material
δ	Parameter describing strain-rate dependence of tensile strength in RHT material model
ε	Strain
ε_{pl}	Plastic strain
$\varepsilon_{pl.failure}$	Plastic failure strain

ε_u	Ultimate strain
$\dot{\varepsilon}$	Strain rate
ϕ	Diameter
κ_C	Transformation factor for damping coefficient C
κ_M	Transformation factor for mass M
κ_P	Transformation factor for load P
κ_R	Transformation factor for internal resistance force R
μ	Normalised density
ρ	Density
ρ_{solid}	Density of fully compacted material at zero pressure
ρ_0	Initial density
σ	Stress

Abbreviations

DIF	Dynamic increase factor
EOS	Equation of state
FRC	Fibre-reinforced concrete
GFRC	Glass-fibre reinforced concrete
GP	General purpose
NCS	Normal strength concrete
NFRC	Natural-fibre reinforced concrete
SDOF	Single degree of freedom
SFRC	Steel-fibre reinforced concrete
SNFRC	Synthetic-fibre reinforced concrete
SIFCON	Slurry infiltrated fibre concrete

1 Introduction

1.1 Background

The load effect from detonation of a cased charge, such as a General Purpose bomb (GP-bomb), includes blast and fragment impacts on the surrounding structures. Since both the load generation (including formation of blast wave and fracture of the casing into propagating fragments) and the structural response (local or global) when subjected to these loads are complex, extensive work has been conducted around the world to increase the knowledge of the phenomena involved. These studies have led to various design and analysis methods – empirical, analytical and numerical – giving estimations of the load characteristics or the structural response. Due to the complexity of weapon loads and their effects, the generality of these methods is still often limited. However, as more is elucidated and the knowledge within the area increases, the methods are being improved. One aspect not yet well understood is the combination of blast and fragment loading and the response caused by this.

Reinforced concrete is still one of the most common materials used in protective structures, but the use of fibre-reinforced concrete increases. This is motivated by the enhanced energy characteristics of fibre-reinforced concrete, compared to plain concrete, which increase its impact and structural resistance. Since the behaviour of fibre-reinforced concrete and normal reinforced concrete differs, analysis and design methods existing for the latter are generally not directly applicable to fibre-reinforced concrete. Due to the lack of experimental data and general knowledge of how the addition of fibres affects the structural response when exposed to high dynamic loads, there are very few methods that can be used to estimate the subsequent damage.

1.2 Aim of the thesis

The project in which the work presented in this thesis has been conducted is a continuation of a research project within a collaboration of many years' duration between Chalmers University of Technology and the Swedish Rescue Services Agency. The long-term aim of the research project is to increase the knowledge of reinforced concrete structures subjected to explosive loading, i.e. a combination of blast wave and fragment loading. Earlier research within the framework of this collaboration has involved experimental and numerical studies of concrete structures, in particular civil defence shelters, by Plos (1995), Johansson (2000) and Leppänen (2004). However, the blast and fragment loadings have until now been studied separately.

The aim of this thesis is to give a basic knowledge of the field of concrete structures subjected to explosive loading. This includes the basics of blast and fragment loads and the characterisation of these, the material behaviour of concrete under high dynamic loading and the modes of failure and damage mechanisms connected with these events.

1.3 Limitations

The phenomena involved in explosive loading, from the explosions and fracturing of the bomb casing and the subsequent load characteristics to the behaviour of the loaded structure, on both material and structural levels, are very complex. Methods used for estimation and characterisation of loads and structural responses caused by detonation of cased charges involve idealisations and simplifications, often necessary in order to make them generic enough. This implies limitations in the methods and the results attained with these.

For explosions of bare charges, the resulting blast load is relatively well known and therefore methods with high accuracy exist to characterise this load. For cased charges the load characterisation is much more complex, since the mechanics of fracturing the casing also influences the resulting loads. The methods for determining the resulting blast load and fragment characteristics in these instances are therefore less accurate due to the many idealisation and simplifications necessary. Accepted methods of determining the load characteristics for cased charges are presented and used within this work. However, the reader should be aware of their limitations.

The fragments used when simulating fragment cluster impacts are of the same geometrical shape, size, velocity and mass, and are all assumed to have normal impact with the same striking velocity. In reality all these parameters would vary between the fragments, but in order to simplify the numerical model and be able to draw general conclusions from the results these simplifications were necessary.

1.4 Outline of contents

This thesis consists of an introductory part, two papers and one conference paper. The introductory part gives a more comprehensive background to the subjects treated in the papers.

In *Chapter 2* the behaviour of concrete under static loading, and how this changes for high dynamic loading, are presented. A brief description of the improved behaviour when adding steel fibres into the concrete mix is given.

Chapter 3 gives general information about explosions and the characteristics of the blast wave and fragments caused by it.

The effects of cased explosions, i.e. blast and fragments, on concrete elements are described in *Chapter 4*. The results from the numerical study presented in the *Conference Paper*, i.e. of how reinforcement bars affect damage caused by local impact, is also discussed. Further, different methods to estimate the damage caused by loads from cased explosions are presented. One of these methods, the single-degree-of-freedom method, is described in more detail.

In *Chapter 5* the numerical simulation method, also used to estimate the damage, is described. This method is given a separate chapter due to its importance for the work presented in this thesis.

A numerical study of how the addition of steel fibres in concrete may affect the projectile impact resistance is presented in *Chapter 6* and *Paper I*.

The effects of blast and fragment loading, and a combination of these two, are presented in *Chapter 7* and *Paper II*.

Major conclusions and suggestions for further research are presented in *Chapter 8*.

2 Concrete Material Behaviour

Concrete is one of the most widely used building materials in the modern civil infrastructure, due among other things to its low cost and wide field of application. Because of its good energy-absorbing characteristics for high pressures and, when properly reinforced, ductile behaviour it is also suitable for use in protective design. The behaviour of concrete under high-rate loading differs from the static behaviour, a fact that must be taken into account in the design and analysis of protective structures.

In order to improve the energy-absorbing characteristics of concrete, mainly in the tensile range, fibres can be added to the concrete mix, resulting in better post-crack behaviour.

2.1 Static and dynamic behaviour

The behaviour of concrete under uni-axial compression and tension is nonlinear, but can be approximated as linear up to about 30-40% and 70-75% of the ultimate strengths, respectively. Thereafter, gradual softening (sometimes called pre-softening) takes place until the ultimate strength is reached (see Figure 2.1), as shown for instance by Bangash (1989), Riedel (2000) and CEB FIP (1999).

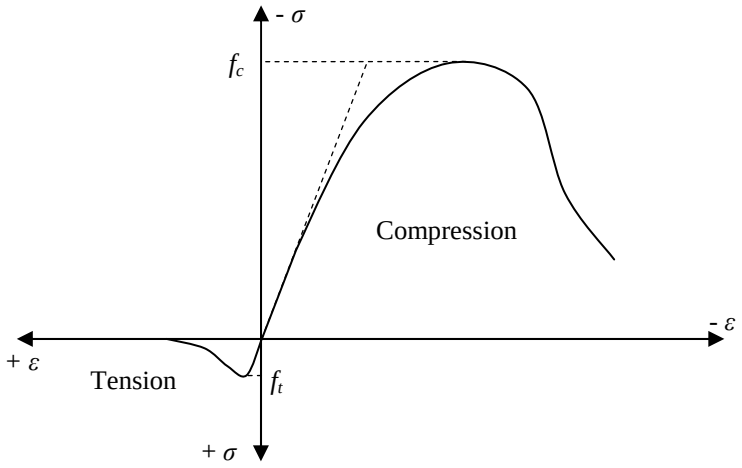

Figure 2.1 Stress-strain relation, based on Bangash (1989).

The low tensile strength and brittle behaviour are two of the most pronounced disadvantages of concrete. The tensile strength, f_t, for normal-strength concrete is less than one tenth of the compressive strength, f_c. In tension it has a brittle behaviour, as the ability to transfer stresses after fracture initiation decreases rapidly; see Figure 2.1. The brittle behaviour can be seen also in compression, for concretes with higher strengths, as the brittleness increases with an increasing ultimate strength. In tension the stress-strain relation is often divided into a stress-strain relation and a stress-crack opening relation, as seen in Figure 2.2. Here w_c is the critical crack opening at which a continuous crack has formed and no more stresses can be transferred. The stress-strain (σ–ε) relation represents the pre-localisation behaviour while the stress-crack opening (σ–w) relation describes the deformations occurring after fracture initiation. The area

under the curve in the stress-crack opening relation represents the fracture energy, G_F. L is the initial length of the tested concrete specimen.

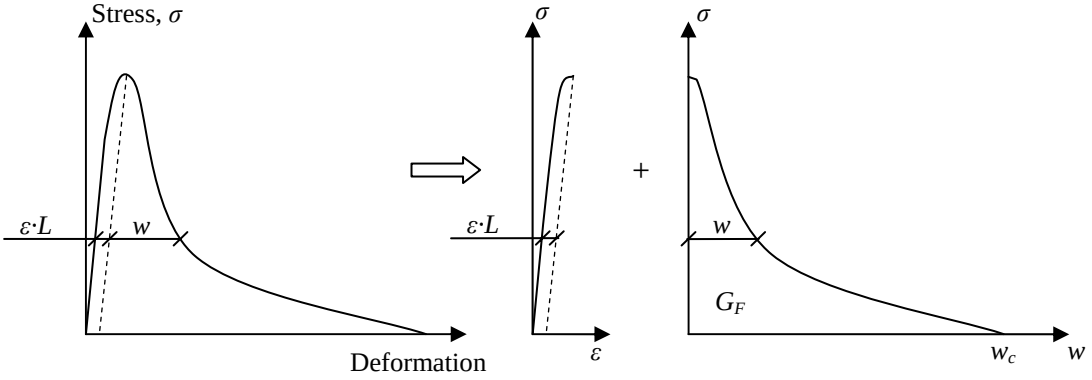

Figure 2.2 Stress-deformation relation for concrete in uni-axial tension, and how it is separated into a stress-strain relation and a stress-crack opening relation.

To facilitate analysis and design procedures, the crack-softening behaviour for concrete in uni-axial tension is often simplified. The degree of simplification is chosen in accordance with the required degree of accuracy of the results and in relation to other simplifications made by the methods used. Several curves have been proposed to describe the crack softening: polynomial or exponential (e.g. Hordijk-Reinhard in Jirásek 2006), multi- or poly-linear, bi-linear (e.g. Gylltoft 1983) and linear (AUTODYN 2005), as seen in Figure 2.3.

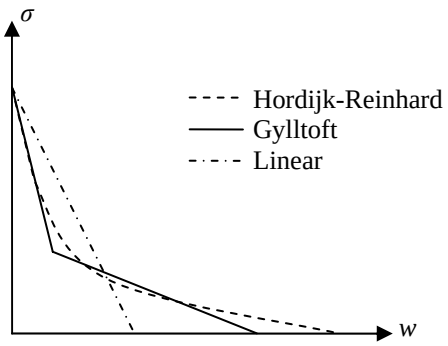

Figure 2.3 Simplified crack opening curves for concrete.

Under multi-axial stress states, often occurring in structural elements, the behaviour differs from the uni-axial behaviour. Confined concrete is stiffer and stronger in compression than unconfined concrete. Under high lateral pressures, occurring during e.g. impact of projectiles or fragments, the compressive strength may be more than 15 times higher than the uni-axial compressive strength, as presented by Leppänen (2004) with reference to Bažant (1996). This means that concrete is a highly pressure-dependent material, which can also be characterised with a relation between the hydrostatic pressure, i.e. the mean value of the principal stresses, and the

density. This relation describes how the density goes from the normal concrete density, with the presence of pores, to a solid concrete density, where all the pores have collapsed and the concrete is fully compacted, as the hydrostatic pressure increases. For more information about the pressure dependence of concrete the reader is referred to Section 5.1 and Leppänen (2004).

As with most materials, the behaviour of concrete changes as the strain rate increases. The increase of the compressive and tensile strength is well known today, and is often characterised by a dynamic increase factor (*DIF*), describing the ratio between the dynamic and static strengths. As seen in Figure 2.4, where Malvar and Ross (1998) have compiled the results of experiments conducted by several researchers, the dynamic tensile strength of concrete may be as much as 5 to 7 times higher than the static ultimate strength. As seen in Figure 2.5, the strain-rate effect is less significant on the compressive strength, but it may still be more than doubled; see Bischoff and Perry (1991).

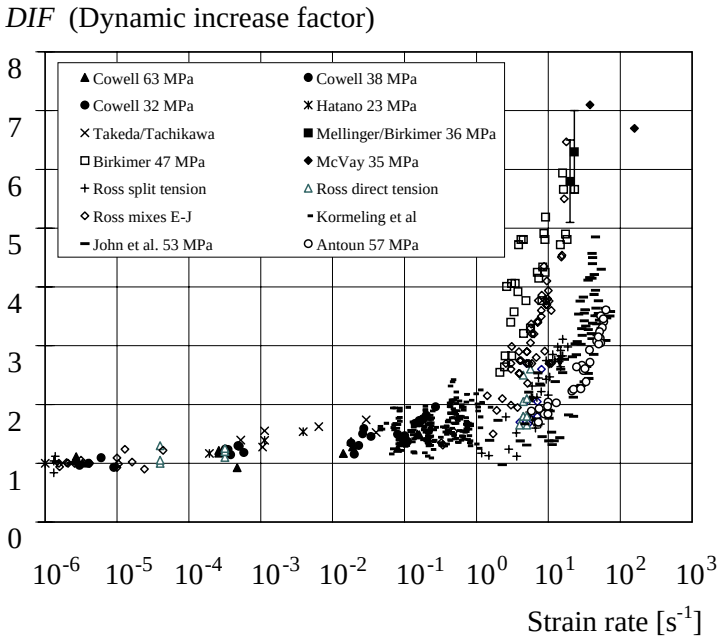

Figure 2.4 Strain-rate dependence for concrete in tension, based on Malvar and Ross (1998).

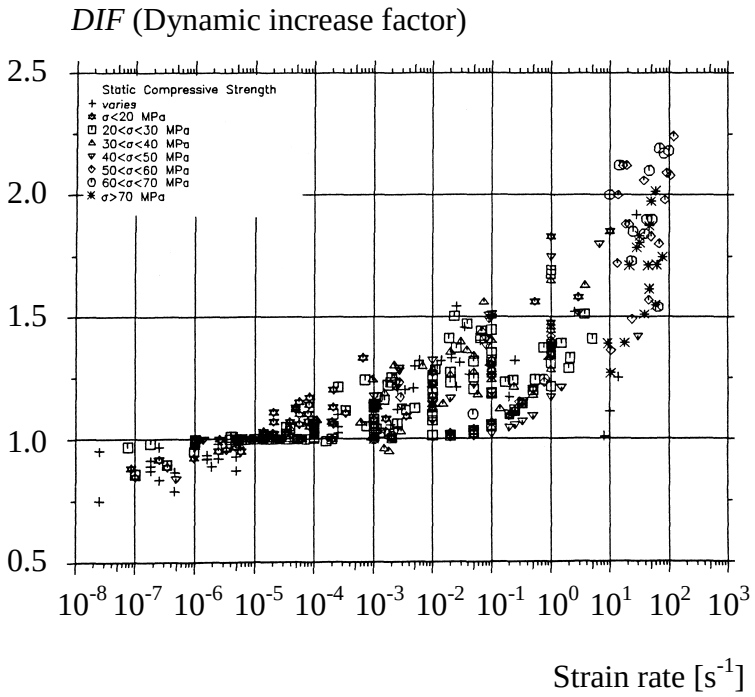

Figure 2.5 Strain-rate dependence for concrete in compression, based on Bischoff and Perry (1991).

Due to the lack of reliable test methods, it was previously unclear whether also the fracture energy is strain-rate-dependent, but more recent studies (e.g. Schuler 2004, Brara and Klepaczko 2007, Weerheijm and van Doormal 2007) indicate that it is. Schuler (2004) has proposed a relation between the dynamic increase factor for the fracture energy and the crack opening velocity; see also Paper I. With a simplified description of the crack softening branch in tension, it can be schematically shown how the strain-rate effect on the tensile strength and the fracture energy influences the crack-softening behaviour, as seen in Figure 2.6.

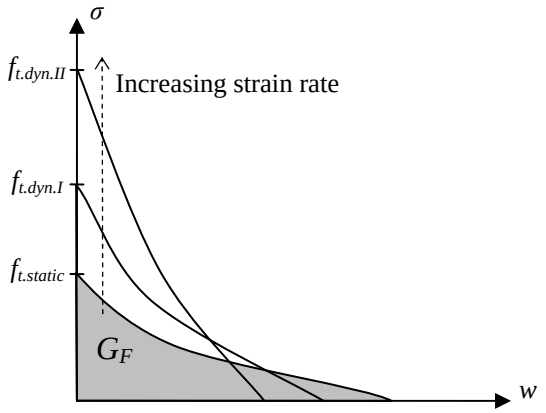

Figure 2.6 Simplified description of crack softening with increasing strain rate, based on Schuler (2004).

2.2 Steel-fibre reinforced concrete

The addition of discrete reinforcing fibres into the concrete mix has been shown to improve the mechanical properties of concrete. However, there are various factors influencing the behaviour of the fibre-reinforced concrete and consequently also the degree of improvement: e.g. concrete matrix quality, fibre type (including material properties and geometry), bond between the fibres and surrounding concrete matrix, and distribution, orientation and concentration of fibres; see Zollo (1997). Fibre-reinforced concretes (FRC) can be subdivided into four classes, based on the fibre material:

- SFRC, steel-fibre reinforced concrete
- GFRC, glass-fibre reinforced concrete
- SNFRC, synthetic-fibre reinforced concrete
- NFRC, natural-fibre reinforced concrete

Since the behaviour differs between these fibre materials, they are generally used in different applications. According to ACI 544 (1996), the most significant properties of steel-fibre reinforced concrete are the improved ability to absorb energy, impact resistance and flexural fatigue endurance; thus it is often used for elements subjected to high loads and impacts. For this reason, the present emphasis will henceforth be given to steel-fibre reinforced concrete and, for further information about the other three classes of fibre-reinforced concretes, the reader is referred to ACI 544 (1996) and Zollo (1997).

Steel fibres improve the ductility of concrete under all modes of loading; but in normal-strength concrete this is more pronounced for tensile than compressive loading, since the plain normal-strength concrete has a more brittle behaviour in tension than in compression; see Section 2.1.

The effects of steel fibres on the ultimate strengths differ between the modes of loading. The compressive ultimate strength of concrete is only slightly increased for volume fractions up to 1.5%. According to Löfgren (2004), also the effect on the ultimate tensile strength is small for low and moderate dosages of steel fibres, which contradicts ACI 544 (1996) where the increase is said to be significant (referring to tests where the increase was 30 to 40% for a volume fraction of 1.5%). Since the increase of shear strength has been shown dependent on the testing technique, it is not clear how much the shear strength is affected by the addition of steel fibres, but it is believed to be increased; see ACI 544 (1996). The effect on the uni-axial tensile behaviour when adding moderate dosages of fibres to concrete is schematically shown in Figure 2.7.

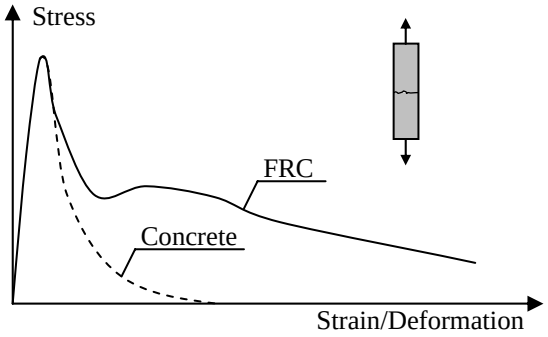

Figure 2.7 Effect of moderate dosages of fibres in concrete on uni-axial tensile behaviour, based on Löfgren (2005).

The increase in impact resistance for steel-fibre reinforced concrete has been studied in several experiments, e.g. by Nataraja *et al.* (2005), Luo *et al.* (2000), Cánovas *et al.* (1994) and Almansa and Cánovas (1999). However, the difference in peak load for normal-strength concrete and steel-fibre reinforced concrete is reported to be smaller in the impact tests than that obtained in static tests, which seems to be true also for the fracture energy; see ACI 544 (1996). This indicates that the relative effect of the fibres in the concrete decreases with an increasing load rate.

Volume fractions of steel fibres of about 0.25 to 2% are generally used in concrete, since higher dosages affect the workability and fibre dispersion; see PCA (2002). However, a special type of steel-fibre reinforced concrete, called slurry infiltrated fibre concrete (SIFCON), may contain volume fractions of fibres ranging from 8 to 12% or even higher; see ACI 544 (1996). This fibre-reinforced concrete can have strength and ductility that far exceed those of conventionally used fibre concrete, but due to its high production costs it is mainly used for impact- and blast-resistant structures; see ACI 544 (1996) and PCA (2002). Nevertheless, only conventionally mixed steel-fibre reinforced concrete, with low or moderate dosages of fibres, was used in the study presented in Chapter 6 and Paper I. Hence, the following reasoning for characterisation of the post-fracture behaviour in tension is applicable to these cases, and may not be valid for other types and higher dosages of fibres.

As in the case of plain concrete, the crack-softening curve can be idealised in different ways and with different degrees of accuracy. For practical applications it has been found that a bi-linear relation, as shown in Figure 2.8, is often a sufficient approximation for fibre-reinforced concrete with low or moderate dosages of steel fibres. Löfgren (2005), through experiments, has made phenomenological interpretations of the parameters, a_1, a_2, b_2, w_1 and w_c describing this relation.

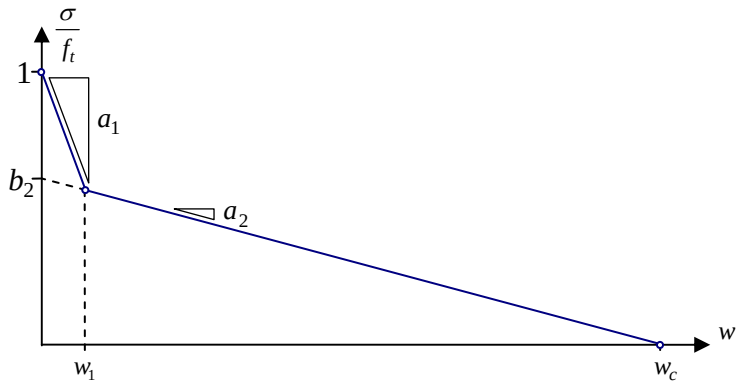

Figure 2.8 Bi-linear stress-crack opening relation for steel-fibre reinforced concrete, based on Löfgren (2005).

The rate of decrease in stress directly after tensile failure initiation is described by the parameter a_1, which is essentially governed by the fracture properties of plain concrete, but may be slightly reduced compared to this. The parameter a_2, describing the rate of stress decrease in the second branch, is principally related to the fibre length. Poor fibre bond or fibre fracture influences the critical crack opening, w_c, which normally is in the range of $L_f/10$ to $L_f/2$, where L_f is the length of the fibres. The value of parameter b_2 is primarily related to the dosage of fibres and increases with increasing volume fraction.

Löfgren (2005) also performed experiments to investigate the hypothesis that there is a linear relationship between fibre content and the tensile stress at different crack openings. The experiments seemed to confirm that it may be acceptable to assume a linear relationship between the number of fibres and the stress-crack opening relation. In the experiments, where end-hooked steel fibres of type Dramix RC-65/35 were used, a relation between the volume fraction, V_f, and the number of fibres per cm^2, n_{fibres}, was determined for the specimens, as:

$$n_{fibres} = 2.5396 \cdot V_f \tag{2.1}$$

By inverse analysis of the experimental results, a relation between the numbers of fibres and the parameter b_2, defined in Figure 2.8, was also determined by Löfgren (2005):

$$b_2 = 0.278 \cdot n_{fibres} + 0.257 \tag{2.2}$$

where 0.257 represents the parameter b_2 for plain concrete in the experiments.

The volume fractions of fibres corresponding to a certain fracture energy, or vice versa, can then be calculated. The relation between the fracture energy and the parameters, a_1, a_2, b_2, w_1 and w_c is known, since the fracture energy equals the area under the curve in Figure 2.8.

3 Weapon Characteristics

The effects of weapons may differ as much as there are types of weapons. For detonation of cased bombs, filled with high explosives, the surroundings will be subjected to blast load and fragment impact. The definitions of these loads are highly dependent on e.g. the bomb geometry, casing thickness and material, type and weight of explosive filling, the surroundings and the stand-off distance, i.e. distance between the point of detonation and the structure studied. Here only the effects of GP-bombs (General Purpose bombs), with a homogeneous casing (not made to fracture in a pre-defined pattern), and bare explosions are discussed. However, the information may also be valid for other bombs.

The initiation of the explosive filling will cause high pressure and temperature inside the casing, which leads to swelling of the casing. During swelling, radial tensile cracks will form at the outside and shear cracks on the inside of the casing. As these cracks meet or propagate to a free border, fragments are formed and start to propagate in the surrounding air away from the point of detonation; see Curran (1997). In order to characterise the loads on structures caused by detonation of a cased bomb, knowledge about blast wave and fragmentation is required.

3.1 Blast load

The formulas and parameters used for characterisation of the blast wave are in most cases empirically determined, in some cases with additional theoretical and computational investigations. Due to a large amount of test data from bare high-explosive detonations the blast load characteristics from such detonation can be estimated with great accuracy. The blast wave resulting from encased explosions, or where the blast wave is reflected on other surfaces before arriving at the target (in the extreme case, confined explosions within a structure), can make the resulting blast load very complex and case-dependent, so that more rough estimations are used in these cases.

3.1.1 Blast wave idealisation

The blast wave, shown as a pressure-versus-time history, at a fixed point with a certain stand-off from the point of detonation, is often idealised as shown in Figure 3.1. This idealisation is valid for detonation in "free air", i.e. distant from any reflecting surface, where the resulting blast wave is not disturbed. Detonation takes place at time $t = 0$ and the blast wave propagates through the air; after a time t_a the blast wave arrives at the point studied. As the wave arrives, the pressure instantaneously increases from the ambient pressure P_0 (in undisturbed air $P_0 \approx 101.3$ kPa) to P_0+P^+, where P^+ is the peak overpressure caused by the detonation, here equal to the incident peak overpressure P_s^+. The overpressure then decays and at a time T^+ after the blast arrival the pressure returns to the ambient pressure P_0 and the positive phase is over. The positive phase is followed by a negative phase, where the negative pressure P^-, relative to the ambient pressure can be

explained as a partial vacuum, meaning that there are fewer air particles than in the surrounding air, since these were moved when the blast front passed; see Johansson and Laine (2007). Thereby, the amplitude of the negative pressure is limited to the absence of the normal ambient air pressure P_0. The duration of the negative phase, T^-, is longer than that of the positive phase.

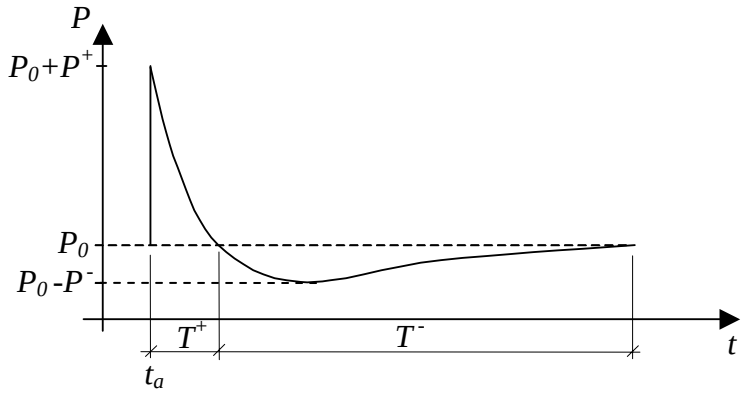

Figure 3.1 Idealised blast wave, based on Leppänen (2004).

In structural design with regard to explosions, not only the amplitude of the pressure is of interest, but also the impulse intensity is an important parameter. The impulse intensity for the positive and negative phases, i^+ and i^-, is calculated as the area under the pressure curve in the positive and negative phases, respectively.

$$i^+ = \int_{t_a}^{t_a+T^+} \left(P(t) - P_0\right) dt \tag{3.1}$$

$$i^- = \int_{t_a+T^+}^{t_a+T^++T^-} \left(P_0 - P(t)\right) dt \tag{3.2}$$

where $P(t)$ is the variation of the pressure as a function of the time, t.

In design with regard to explosions, the negative phase of the blast loading is considered less important than the positive phase; thus often only the latter is taken into consideration. A pressure-time relation often used for the positive phase, e.g. in the computer code ConWep (1992), is:

$$P(t) = P_0 + P^+\left(1 - \frac{t}{T^+}\right)e^{-\alpha t/\ T^+} \tag{3.3}$$

where t is the time after the arrival of the blast wave, i.e. measured from the time of arrival t_a. By means of the factor α, the decay of the pressure is adjusted. If the overpressure P^+, the duration of the positive phase T^+ and the positive impulse intensity i^+ are known, the factor α can be determined by combining Equations 3.1 and 3.3.

Even though not often used in design purposes, expressions for the variation of the pressure as a function of the time can be found also for the negative phase; see Johansson and Laine (2007), in which the relation in Equation 3.4 is presented with reference to Brode (1955).

$$P(t) = P_0 - P^- \frac{t}{T^-}\left(1 - \frac{t}{T^-}\right)e^{-4t/\,T^-} \tag{3.4}$$

Blast parameters from bare spherical high-explosive charges in free air are well known and can be found in most handbooks and design manuals within the area, e.g. Johansson and Laine (2007), Krauthammer (2006) and U.S. Army (1992). However, due to the complexity and great variation of behaviour for conventional weapons, which are cased and have other geometries than spherical or cylindrical, the blast parameters for uncased spherical charges are used also when describing the blast wave caused by these bombs. This means that neither the non-rotationally-symmetric distribution of the pressure in the air, nor the energy consumed to fracture the casing into fragments, resulting in a reduced blast pressure compared to bare-charge explosion, is taken into account. The latter simplification is further discussed in Section 3.3 where the combined loading of blast and fragments is described.

3.1.2 Blast wave reflection

When the blast wave strikes a surface which is not parallel to its direction of propagation, e.g. a wall or the ground, it is reflected and the behaviour of the blast load changes. Reflections can be divided into regular and Mach reflections, depending on the incident angle and the blast peak overpressure. The regular reflection can be divided into normal and oblique reflection, and the Mach reflection can be viewed as a special case of oblique reflection where the angle of incidence is large enough to cause a phenomenon called a Mach wave; see Johansson and Laine (2007). Normal reflection takes place when the blast strikes a perpendicular surface and the effect can lead to a significant enhancement of the pressure, where the reflected overpressure P_r^+ will be between 2 and 8, ASCE (1999), and according to Johansson and Laine (2007) and Baker (1973) as much as 20, times higher than the incident overpressure P_s^+. The pressure enhancement of the reflected wave compared to the incident wave can be explained by arresting flow behind the reflected shock wave; see ASCE (1999). For further information about the normal, oblique and Mach reflections, see e.g. Johansson and Laine (2007), Leppänen (2004) and Krauthammer (2006).

The reflected pressure has the same general shape as the incident pressure, as shown in Figure 3.2. The duration of the positive phase is the same for the incident and reflected pressures, but the peak pressure is higher than that of the incident pressure. This means that Equation 3.3 can be used also to describe the positive, reflected pressure if the peak overpressure P^+ is replaced by the peak overpressure for the reflected wave P_r^+.

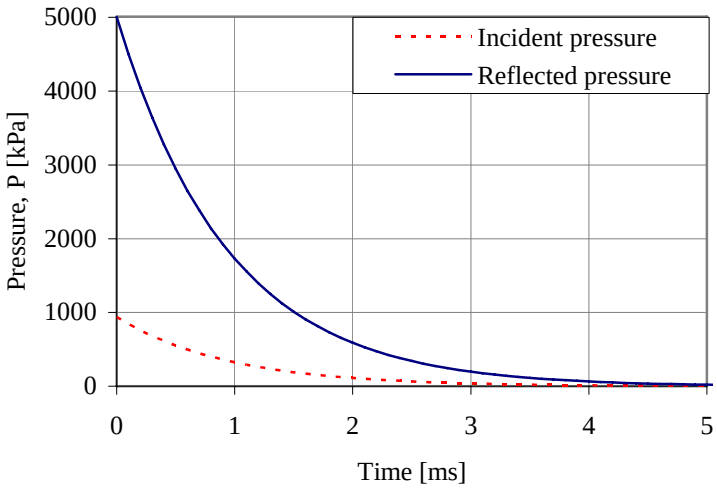

Figure 3.2 *Incident and reflected pressure at stand-off 5 metres, caused by a 125 kg TNT bare spherical explosion, calculated according to ConWep (1992).*

3.2 Fragments

The fragmentation process of a bomb casing is very complex and dependent on the example at hand. Hence, generic empirical expressions for the fragment characteristics cannot be developed in the same way as for bare explosions in free air, unless a very large number of test results are compiled and analysed. Instead analytical methods, where the exploding items are assumed to be cylindrical cased charges, are derived and confirmed with test data. Thereby, the expressions used to characterise the fragments apply especially to cylindrical items and to items that can be reasonably approximated as either cylindrical items or series of cylindrical items. The more the shape of the bomb deviates from this, the less accurate are the fragment characterisation estimations.

The size, velocity and spatial distribution of the fragments resulting from detonation of a cased bomb will mainly depend on the properties, geometry and thickness of the casing and the properties and amount of the explosive filling.

3.2.1 Mass and size distribution

As the weaknesses within a homogeneous casing material are stochastically distributed, so is the mass and size distribution of the fragments. The nose and tail sections of a bomb, which usually are relatively massive, break up into a small number of heavy fragments. The body of the bomb, which normally is somewhat cylindrical in shape with varying diameter and material thickness and less massive than the nose and tail sections, will fracture into many smaller fragments.

The mass distribution for an encased bomb can, under the condition that it can be approximated as either a cylindrical item or a series of cylindrical items, be estimated

by a formula developed by Mott, shown in Equation 3.5, from Krauthammer (2006) but converted to SI units.

$$N_f = \frac{W_c \, e^{-\sqrt{m_f / M_A}}}{2M_A} \tag{3.5}$$

where $M_A = B_x^{\,2} t_c^{\,5/3} d_i^{\,2/3} \left(1 + t_c / d_i\right)^2$

and
- N_f the total number of fragments with mass larger than m_f
- W_c weight of casing [kg]
- m_f fragment weight [kg]
- M_A fragment distribution factor [kg]
- B_x Mott explosive constant [$kg^{1/2}m^{-7/6}$]
- t_c average casing thickness [m]
- d_i average inside diameter of casing [m]

For design purposes a design fragment is often used. The mass, W_f, of the design fragment is, in accordance with design manuals (e.g. U.S. Army (1992)), determined by specifying a confidence level, C_L, giving the probability that this will be the heaviest fragment produced by the detonation. The weight of the design fragment, according to this approach, is calculated as:

$$W_f = M_A \ln^2\left(1 - C_L\right) \tag{3.6}$$

This approach is justified in design against individual fragment impact and the possible subsequent local damage, i.e. spalling, penetration, scabbing and perforation (further discussed in Section 4.1). In design with regard to the fragment cluster, the combined effects of the impulse and impact of the striking fragments are of interest. With this condition, where the damage caused by the cluster of fragments is of interest rather than the local damage caused by individual fragments, it may be necessary to use another approach to find a design-fragment weight than that presented above; see Equation 3.6.

An alternative approach is to use the impulse distribution for the fragments by means of the fragment mass distribution, calculated with Equation 3.5, and the fragment velocity, further discussed in Section 3.2.2. This approach is discussed in Section 7.1.3, where it is used to determine a design-fragment weight that, in turn, is used within a study of the combined effects of blast and fragment loading on a reinforced concrete wall.

3.2.2 Fragment velocities

The average initial velocity v_0, imposed on the fragments during the casing fracture can be estimated from the Gurney equation, as seen in Equation 3.7, from Krauthammer (2006). This is an upper bound estimation of the initial velocity since it is based on energy balance within the explosive and the metal case system, not taking into account the energy loss during rupture of the casing. The Gurney equation presented here is derived for cylindrically shaped bombs.

$$v_0 = \sqrt{2E}\left[\frac{W/W_c}{1+0.5W/W_c}\right]^{1/2} \tag{3.7}$$

where $\sqrt{2E}$ Gurney constant
W weight of explosive [kg]
W_c weight of casing [kg]

The Gurney constant, also called Gurney velocity, is specific to the explosive material and is often listed for the most common high-explosive fillings used for bombs in literature for protective design. However, the constant given may differ between different references. In Krauthammer (2006) the value of the Gurney constant for TNT is given as 7 600 ft/s (2 316 m/s); with reference to U.S. Army (1992) and in U.S. Army (1990) it is given as 8 000 ft/s (2 438 m/s).

The striking velocity of a fragment, v_{sf}, at a certain distance R_f (in metres) from the detonated bomb, will be lower than the initial velocity, v_0, due to air resistance. The velocity of larger, heavier fragments will decrease slower than the velocity of smaller, lighter fragments. The striking velocity of fragments with weight m_f (in kg) can be calculated as, Krauthammer (2006) converted to SI-units:

$$v_{sf} = v_0\, e^{-0.004\left(\frac{R_f}{(m_f)^{1/3}}\right)} \tag{3.8}$$

3.2.3 Fragment distribution in surroundings

For detonating bombs, the fragment distribution in the surroundings will not be uniform, meaning that the placement of the bomb relative to the target structure is of importance. The uneven distribution of fragments depends, among other things, on the bomb geometry (including case thickness and diameter variations), placement of the explosive filling within the bomb and where in the bomb the detonation is initiated.

3.3 Combined loading of blast and fragments

The combined blast and fragment loading involves impulse from the blast wave and the striking fragments, and impact from the fragments. As mentioned in Section 3.1.1, the reduced blast pressure due to the energy consumed during casing break-up is often not taken into account in the design manuals. According to ASCE (1999), it is most often reasonable to neglect the casement effects, including both the fragment impulse and impact. This is justified in ASCE (1999) by the statements that an acceptable estimation of the combined impulse associated with the blast and fragment loading can be derived by using the total charge for the calculation of blast impulse, i.e. the same as not reducing the energy release due to the fracture process of the casing, and that the material degradation due to fragment impact *"...is beyond what can reasonably be expected for the designer of a typical facility."* However, according to Girhammar (1990), the combined impulse of the blast and fragment loading is

considerably higher than the impulse of bare charges, at least in the near field of the detonation. Further, a synergy effect has been observed in many experiments in the case of combined blast and fragment loadings, meaning that the damage from the combined loading is greater than that from the sum of the blast and fragment loadings treated separately; see Girhammar (1990).

The different velocities of the blast wave and the fragments, when propagating in the air, result in different times of arrival for the two loads. In the close range (within a few metres) the blast load travels faster than the fragments. However, due to the faster decay of the blast velocity, the fragments will arrive before the blast wave, see Figure 3.3. For a 250 kg GP-bomb with 50 weight per cent TNT the blast and fragment will arrive at the same time at an approximate distance of 5 metres from the point of detonation.

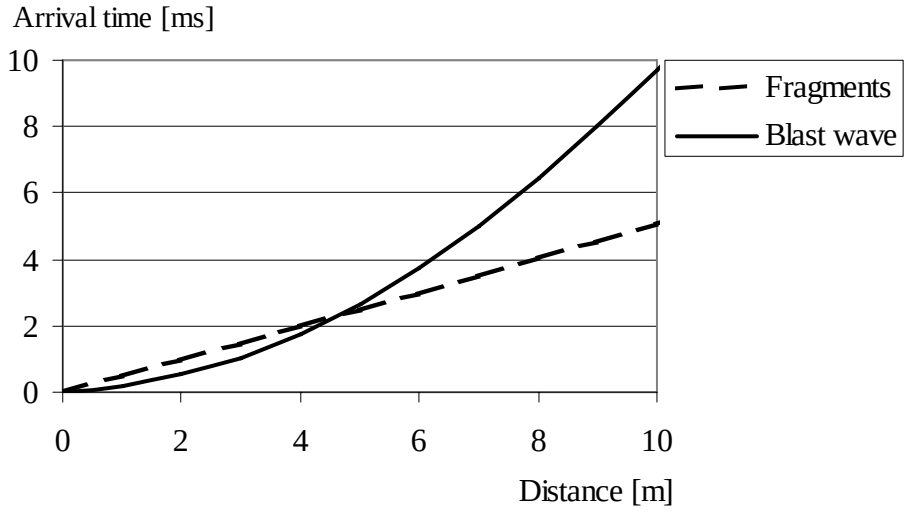

Figure 3.3 Time of arrival for blast wave and fragments as a function of the stand-off for a 250 kg GP-bomb with 50 weight per cent TNT, from Leppänen (2004).

4 Weapon Effects on Reinforced Concrete

The response of a reinforced concrete structure, subjected to severe dynamic loading, may differ considerably from that caused by static loading. This may to some extent be explained by the inertia effects in the structural response, which becomes more pronounced the more the load duration decreases, and the stress waves caused by the dynamic load, travelling in the structure. The enhanced material strengths due to the higher loading rate, discussed in Section 2.1, also affect the response. In this chapter the response of reinforced concrete elements subjected to severe dynamic loads is presented, and different analysis methods used to estimate this response are briefly described.

4.1 Modes of damage

Depending on the load and structure characteristics, the response of the target will differ. In the case of blast loading at relatively large stand-offs, with uniform loading over the element, the response will be global and for close-in blast loading and small stand-offs the resulting damage is localised. Fragment impact has a local effect on the element, but may also cause global response, especially in the case of uniform fragment cluster impact.

4.1.1 Global response

The global behaviour of a reinforced concrete beam or slab can be generalised to membrane, flexural and shear failure; see ASCE (1999). Membrane failure occurs due to tensile, and in some cases compressive, in-plane forces in the element, and can only occur for beams where the supports provide sufficient strength and stiffness to resist in-plane displacement of the edges. However, membrane failure may also occur for two-way slabs without horizontal restraint; see Bailey (2004).

Flexural failure occurs after formation of plastic hinges, resulting in a mechanism or when the in-plane deformations are large enough to make the beam slip of the supports.

Shear failure can, in the same way as for statically loaded reinforced concrete elements, occur due to diagonal tension and compression related to flexural behaviour; hence it must be taken into consideration also in the case of severe loading. However, direct shear (or dynamic shear) response is typical for short-duration dynamic loads and is caused by the high shear inertia forces, which do not exist under static or slow dynamic loading; see ASCE (1999). The direct shear is a local response in that it is localised to zones of geometric or load discontinuity, but is here still considered as global response since it affects the overall behaviour of the structural element. This failure occurs very early in the structural response and before any significant bending deformation takes place, so it is not associated with flexure. The phenomenon of direct shear and how it emerges are well described in Johansson (2000) and Krauthammer (2006).

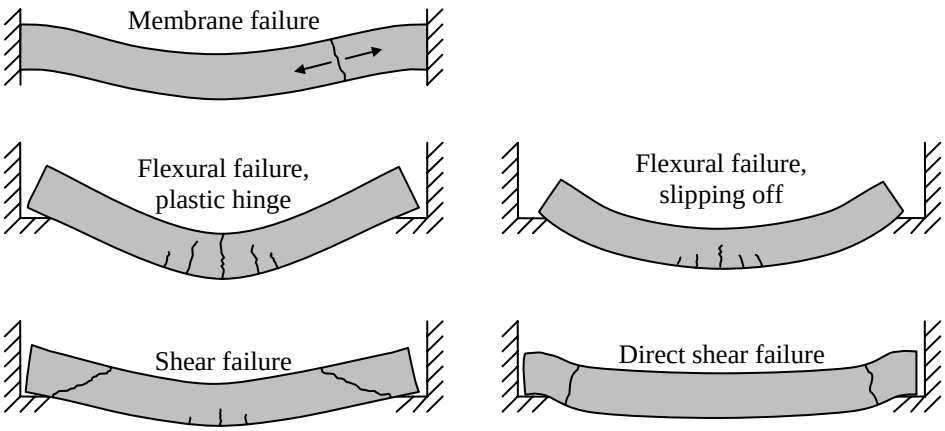

Figure 4.1 Global damage of reinforced concrete beam.

4.1.2 Local response

For contact bursts, blasts with short stand-offs or blast of large charges, a compressive stress wave is generated by the high-pressure pulse applied to the front face and causes localised cratering, so-called spalling. The compressed stress wave travels through the thickness of the structural element and is reflected as a tensile wave when reaching the rear face. This tensile wave may cause failure in the rear face region, resulting in scabbing of the concrete, meaning that a part of the concrete will separate from the structure and travel into the space behind with a certain velocity. If the front face crater and the scabbing zone are merged, the cross-section is breached; see Figure 4.2.

In the case of fragment or projectile impact, the body penetrates into the concrete, resulting in spalling. The compressive stress wave thus created may cause scabbing at the rear face of the structural element in the same way as contact bursts. The depth of penetration for the fragment/projectile depends on its characteristics and the material properties of the target material. With deep penetration, relative to the thickness of the structural element, plugging may occur. Plugging is the formation of a cone-like crack in front of the penetrating body and the possible subsequent punching-shear plug; see Li *et al.* (2005). If the impacting body travels through the structural element, perforation has occurred; see Figure 4.2.

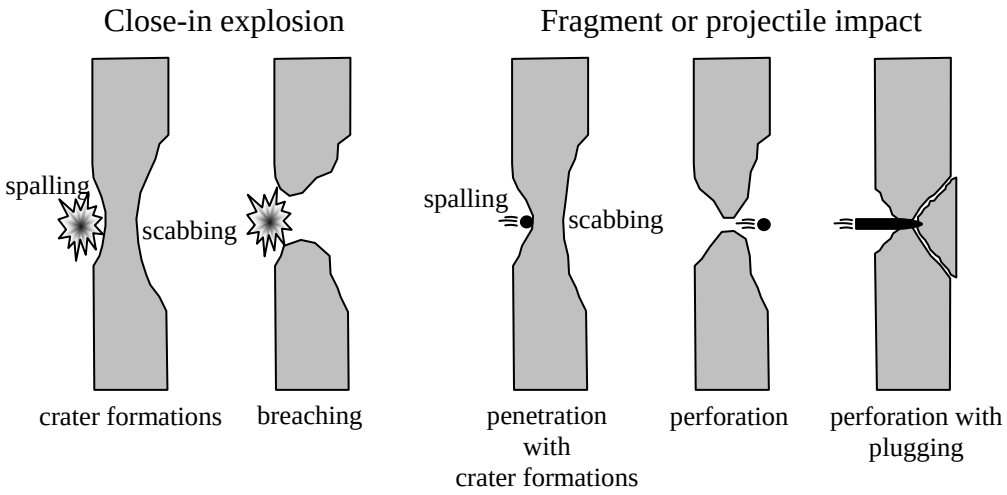

Figure 4.2 Local damage caused by close-in explosion and impact.

A single heavy fragment causes a higher degree of damage than a single less heavy fragment when they have the same striking velocity. This is shown in Table 4.1, where the required thicknesses of a concrete walls, with compressive strength of 30 MPa, just prevents perforation by fragments of different weights, ranging from 5 to 400 grams, and with striking velocities up to 3 000 m/s are shown. The values are based on equations from Krauthammer (2006) and are presented by Leppänen (2004).

Table 4.1 Thickness of concrete wall (compressive strength of 30 MPa) for various fragment weights and striking velocities, based on equations from Krauthammer (2006) and are presented by Leppänen (2004).

Striking velocity [m/s]	Fragment mass [g]					
	5	25	50	100	200	400
300	22	39	50	65	84	108
600	30	54	70	91	118	153
900	39	74	97	127	167	220
1 200	53	101	134	177	235	312
1 500	70	135	180	239	318	424
1 800	90	174	233	312	416	556
2 100	112	220	295	394	528	707
2 400	138	271	363	487	653	877
2 700	166	327	439	590	792	1 064
3 000	196	389	522	702	943	1 268

4.2 Effect of reinforcement on response

As regards global response, the effect of reinforcement is crucial for the energy-absorbing capacity of a concrete structural element, and thereby also its capacity to withstand blast and fragment loading and avoid structural collapse. A properly reinforced concrete structure ought to have a ductile behaviour.

Local damage does not in general lead to structural failure, and a certain level of local damage is often allowed to occur. However, the damage must still be limited. With close-in blast loading and fragment or projectile impact, where spalling occurs on the front face and possible scabbing craters form at the rear face, the presence of reinforcement bars may limit the damage since it holds the concrete in place. This is especially true in the case of scabbing, where the amount of reinforcement is a highly critical parameter; see Leppänen (2004). With projectile and fragment impacts, the penetrating body may strike the reinforcement, leading to a decreased depth of penetration and to damage of the reinforcement bar and the surrounding concrete. Impact on the reinforcement may also lead to local steel rupture, but also to reduced bond between the reinforcement and the concrete further away from the impact point due to vibrations.

A numerical study of how the projectile impact resistance of concrete was affected by the presence of reinforcement and reinforcement detailing was conducted within the work presented; see Conference Paper. It was shown that reinforcement may have an influence on both the depth of penetration and the front-face crater size, and that the effect decreased with a decreasing amount of reinforcement within the damage zone. The increase in impact resistance is plausibly explained by increased confinement effects from the reinforcement. Since the damage caused by a projectile is local, reinforcement bars located further away from the impact area will not influence the impact response. This seems logical since the confinement effects of the reinforcement decrease with increasing distance between the projectile path and the reinforcement bar.

4.3 Analysis tools for estimation of response

Different methods may be used to estimate the response of reinforced concrete structures subjected to blast and/or fragment impact caused by an explosion. The list below shows a rough classification of these methods, presented in order of increasing complexity:

- empirical and analytical equations, charts and simple computer codes
- single-degree-of-freedom analyses, simple or advanced
- numerical simulations with finite-element codes or hydrocodes

Examples of empirical and analytical equations are those used to estimate the depth of penetration and crater sizes caused by fragment or projectile impact. These equations are in some cases also implemented in relatively simple computer codes, which calculate the response for given input data. As an example, the computer code ConWep (1992) is based on the expressions presented in the technical manual

U.S. Army (1992). There are also many charts with which the expected response of blast or impact loading can be estimated. Parts of these charts are only representations of empirical and analytical equations, already mentioned, and others are made by graphical presentations of results from single-degree-of-freedom analyses. Examples of empirical equations for estimating depth of penetration and required concrete thickness to prevent perforation can be found in Appendix A.

The analytical method of simplifying a deformable element to an equivalent single-degree-of-freedom system (SDOF system) is mainly used for estimations of the global response due to blast loading, but may also be used in the case of fragment impacts or combination of these two loads; see Forsén and Nordström (1992). Advanced SDOF models include non-linear behaviour, flexural-shear-membrane interaction and rate effects, but only the simple SDOF method is further discussed in Section 4.4. For further information about the advanced SDOF analyses the reader is referred to Krauthammer (2006) and ASCE (1999).

Numerical simulation by use of finite-element codes or hydrocodes can be performed with different degrees of accuracy, but is the most complex method for estimation of the response due to blast and/or fragment loading discussed here. Many parameters determine the accuracy of the simulations, e.g. the material model used to describe the behaviour of the material, the choice of numerical mesh and element type. The method of numerical simulations by use of the hydrocode AUTODYN (2007) is further discussed in Chapter 5.

4.4 SDOF method

In order to estimate responses of beams and slabs exposed to loads with impulsive character, the single-degree-of-freedom method (SDOF method) may be used. The method allows the deformable body to be transformed into an equivalent SDOF system, by means of transformation factors, κ_M, κ_C, κ_R, and κ_P for the mass, M, the damping coefficient C, the internal resistance force R and the external load $P(t)$, respectively. This transformation is schematically shown in Figure 4.3.

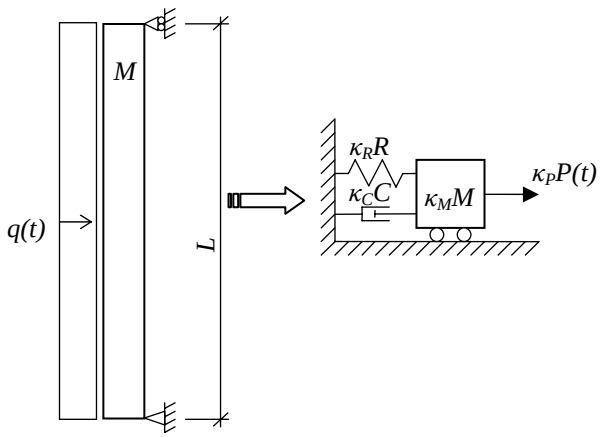

Figure 4.3 Principle of transforming deformable body to an equivalent SDOF system. In case of uniformly loading P(t)=q(t)·L, where q(t) is the uniformly distributed load, and L is the length of the beam.

By solving the equation of motion, Equation 4.1, for the equivalent SDOF system the displacement, u, velocity, $\dot{u}$, and acceleration, $\ddot{u}$, of a predefined point in the analysed body can be estimated. The damping is often neglected since its influence on the peak response is relatively small. Neglecting the damping also gives results on the safe side in design since the capacity of the structural element is underestimated; see Nyström (2006).

$$\kappa_M M \ddot{u} + \kappa_C C \dot{u} + \kappa_R R = \kappa_P P(t) \tag{4.1}$$

The derivation of transformation factors, based on conservation of energy and work within the transformation, requires a defined shape of deflection (mode shape) of the deformable body. Even though the first bending mode is generally dominant as the shape of structural elements subjected to dynamic loads, it will also be influenced by higher modes. For an SDOF system this influence cannot be taken into account and the first bending mode is most often assumed (see e.g. Krauthammer 2006 and ASCE 1999), so also within this work.

The internal force, R, describes the ability of the structural element to resist the external load and is often described with a load-displacement relation. The load-displacement relation can be taken as any relation describing the behaviour of the structural element, but it must be observed that the derivation of the transformation factor, κ_R, for the internal force also depends on this curve, and thus a complex relation makes the derivation complicated

In Figure 4.4 the variation of the internal force, R, as a function of the displacement, u, is shown for three different material response idealisations (linear-elastic, ideal-plastic and bi-linear).

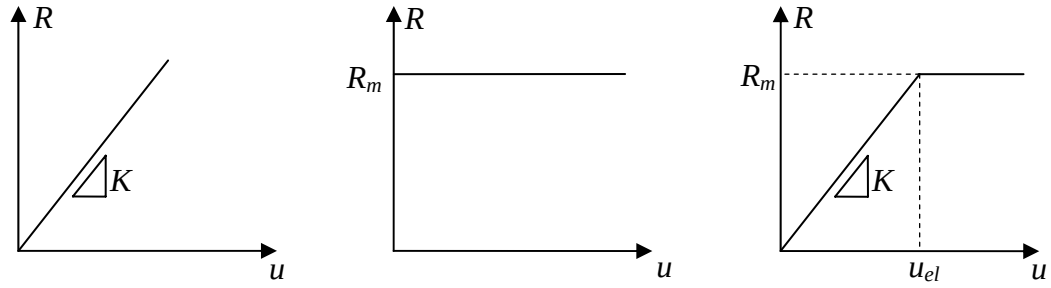

Figure 4.4 Linear-elastic, ideal-plastic and bi-linear material behaviour, shown as internal resistance-deflection relation, and the corresponding functions.

In the SDOF analyses conducted within the work presented in Section 7.2 and Paper II, an ideal-plastic material response was assumed. For the simply supported, reinforced concrete beam subjected to a uniformly distributed load, as in the study, this is considered to be accurate enough.

Values of the transformation factors can be found in literature for linear-elastic and ideal-plastic material response, concentrated and uniformly distributed loads and different support conditions; see for example Nyström (2006). In Table 4.2 the

transformation factors for linear-elastic and ideal-plastic material responses are presented for a simply supported and fixed beam subjected to a uniformly distributed load.

Table 4.2 Transformation factors for a simply supported and fixed beam subjected to a uniformly distributed load for linear elastic and ideal plastic material behaviours, from Nyström (2006).

Support condition	Material behaviour	κ_M	κ_R	κ_P
Simply supported	Elastic	0.504	0.640	0.640
	Plastic	1/3	0.5	0.5
Fixed	Elastic	0.406	0.533	0.533
	Plastic	1/3	0.5	0.5

5 Numerical simulations

For numerical simulations of severe dynamic loading and the resulting deformations and pressures, the non-linear geometrical and material behaviours must be used in order to achieve accurate results. Hydrocodes are used for highly time-dependent dynamic problem-solving, including non-linearity, by use of finite difference, finite volume and finite element techniques. The differential equations expressing the conservation of mass, momentum and energy, together with a material model and a set of initial and boundary conditions, give the solution of the problem. The material model should approximate the observed physical behaviour of a real material under the specific conditions of interest to be able to give accurate results.

The software AUTODYN 2D and 3D can be used to solve non-linear problems in solid, fluid and gas dynamics. The simulations can be conducted by use of different numerical techniques, which are appropriate for the different domains of physical problems. Some of these numerical techniques can also be coupled to solve interaction problems.

5.1 Material models

For static and low-dynamic simulations, a constitutive model, describing the relation between the stress and deformations for the material, is enough to describe the physical behaviour of a solid material. However, in the case of severe loading, including large deformations and very high pressures, the constitutive model must be supplemented by a equation of state (*EOS*), relating the pressure, density and internal energy for the material. Hereby, the material model relates the flow variables in the differential conservation equations for a specific material.

A description of the RHT material model, including the constitutive model and the equation of state, used for concrete in the numerical simulations presented in Chapters 6 and 7, Paper I and II, and the Conference Paper is given here.

5.1.1 RHT – constitutive model for concrete

The RHT model is the constitutive model used to describe the behaviour of concrete. The model, developed by Riedel (2000), includes three pressure-dependent surfaces in the stress space: the elastic limit surface, Y_{el}, the failure surface, Y_{fail}, and the residual strength surface, Y_{fric}, as seen in Figure 5.1.

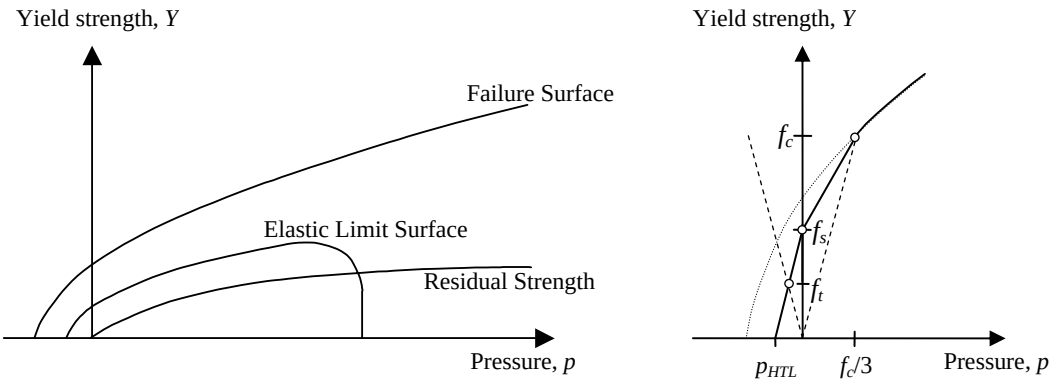

Figure 5.1 Schematically shown surfaces used in the RHT constitutive model (left), from Leppänen (2004), and behaviour of the failure surface for low hydrostatic pressures (right), based on Riedel (2000).

Since the yield strength, Y, increases with increasing hydrostatic pressure, p, the pressure hardening for concrete, discussed in Section 2.1, is taken into account. A function Y_{TXC} is used to describe this hydrostatic pressure dependence of the compression meridian. For lower hydrostatic pressures than $f_c/3$ the compressive meridian is described by straight lines through specified points, as shown in Figure 5.1. For hydrostatic pressures exceeding $f_c/3$, Equation 5.1 is used to calculate Y_{TXC}, where A and N describe the shape of the curve, p_{HTL} is the so-called hydrodynamic tensile limit and is defined in Figure 5.1 (and Section 5.1.2), and F_{Rate} is a factor taking the strain-rate dependence into account.

$$Y_{TXC}(p) = f_c\left(A\cdot\left(\frac{p}{f_c}-\frac{p_{HTL}}{f_c}\cdot F_{Rate}\right)^N\right) \quad \text{for } p \geq f_c/3 \tag{5.1}$$

However, the failure surface not only depends on the hydrostatic pressure and the strain rate, but also takes into account the increased brittleness in shear and tension, compared to compression. This is done by adding a function $R_3(\theta)$, which describes the third-invariant dependence in the deviatoric section, to the failure-surface equation:

$$Y_{fail} = Y_{TXC}(p)\, R_3(\theta)\, F_{Rate}(\dot{\varepsilon}) \tag{5.2}$$

The elastic limit surface limits the elastic stresses, and for increasing stresses linear strain hardening takes place until the failure surface is reached, which initiates failure in the material; see Figure 5.1. After failure initiation a damage model is used for strain softening, taking into account the gradual loss of load-carrying capacity for concrete after reaching the tensile or compressive strength. This is done by linear reduction of the material strength, from the yield strength to the residual strength, by use of a damage factor, D, according to Equation 5.3. The damage factor D is characterised by the plastic strain, ε_{pl}, relative to the plastic failure strain, $\varepsilon_{pl.failure}$, for the material. The plastic failure strain is calculated according to Equation 5.4, where D_1 and D_2 are material parameters. The residual strength is defined by the residual

strength surface, Y_{fric}, expressed in Equation 5.5. Contrary to the failure surface, the residual strength surface does not take the third-invariant, or the strain-rate, dependence into account.

$$D = \sum \frac{\varepsilon_{pl}}{\varepsilon_{pl.failure}} \tag{5.3}$$

$$\varepsilon_{pl.failure}(p) = D_1 \left(\frac{p}{f_c} - \frac{p_{HTL}}{f_c} \right)^{D_2} \tag{5.4}$$

$$Y_{fric} = f_c \cdot B \cdot \left(\frac{p}{f_c} \right)^{M_1} \tag{5.5}$$

It should also be pointed out that there is a minimum limit of the plastic failure strain, expressed in Equation 5.4. This limit is set by default to 1% in the RHT material model.

AUTODYN uses a linear softening curve for brittle materials, e.g. concrete, but according to Jirásek (2006) a linear softening curve can be used only for rough approximations, so it may be justified to use a more accurate shape. Again referring to Jirásek (2006), the Hordijk-Reinhard expression (also described in e.g. van Mier (1984)) gives the best fit to experimental results, but is relatively complicated. This may justify the use of a simpler relation, such as an exponential or bi-linear crack-softening law (see Section 2.1), which usually still gives results with good accuracy.

A hydrodynamic tensile-failure model is used by default in the RHT material model, meaning that if the value of the hydrodynamic pressure in a cell falls below a specified limit, tensile failure is assumed to occur. However, it is not possible to specify a fracture energy, or to use a modified crack-softening description for this tensile-failure model. In AUTODYN it is possible to use a principal-stress tensile-failure model together with the RHT strength model, also providing both these possibilities. The use of a principal-stress tensile-failure model entails that the strain-rate dependence of the tensile strength defined in the RHT strength model is no longer activated. Within the numerical study described in Chapter 6, trials were made to reintroduce this strain-rate dependence by employing a user-subroutine. However, these trials failed due to emergence of stability problems, further discussed in Section 6.2.

Leppänen (2004) developed a modified crack-softening behaviour in the RHT material model and used the bi-linear softening curve proposed by Gylltoft (1983). Leppänen (2004) also modified the tensile strain-rate dependence in the RHT model to better fit experimental data found in literature. The modified strain-rate dependence was introduced in a user-subroutine, which, as mentioned above, was not possible in the study presented in Chapter 6. The routine for sub-routines in AUTODYN have changed in the newest version, i.e. version 11.0, and may explain the difference in success.

Another modification of the RHT material model, contemporaneous with Leppänen's (2004) modification, has been developed by Schuler (2004), which includes a more refined damage model for the description of crack softening. Again a modified strain-rate dependence is used for the tensile strength, but a power function is used to describe the shape of the descending crack-softening curve which also takes into account strain-rate dependence of the fracture energy. However, this modification is yet not implemented in the commercial version of AUTODYN.

5.1.2 Equation of state

By use of thermodynamic equilibrium it can be shown that the local hydrostatic pressure, the specific volume and the specific energy are related through an equation of state (AUTODYN (2005), Gebbeken *et al.* (2006)). The form of the *EOS* differs for different materials and phenomena, and here only the *EOS* used within the RHT material model is described. For further and more generic information about the equation of state the reader is referred to AUTODYN (2005).

The *EOS* characteristics are determined by material testing. However, since the energy distribution is impossible to measure in these tests, only a two-dimensional relation between the density and the pressure can be found, and the energy has to be considered implicitly by the equation of energy conservation; see Gebbeken *et al.* (2006). The *EOS* for concrete, also used for other porous materials, is shown in Figure 5.2. A linear-elastic material behaviour can be assumed from the hydrodynamic tensile limit, p_{HTL}, to the initial compaction pressure, $p_{compaction}$. The hydrostatic tensile limit is the minimum pressure for which the material can sustain continuous expansion; for lower pressures the material will fail. If the compaction pressure is exceeded, the pores start to collapse and the plastic compaction phase is entered. This pore collapse and subsequent compaction of the concrete continues for increasing hydrostatic pressures until the pressure, p_{solid}, is reached where all the pores have collapsed and the material again approximates an elastic behaviour. The initial density of the concrete is denoted ρ_0 and the density of the fully compacted material at zero pressure is ρ_{solid}.

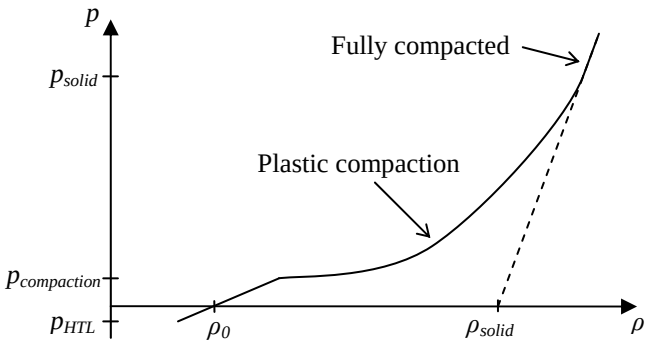

Figure 5.2 EOS for concrete, based on Gebbeken et al. (2006) and Riedel (2000).

In the RHT material model a so-called *P-α EOS*, written in a general form in Equation 5.6, is used to describe the change in state for concrete. The *P-α EOS* combines a polynomial description of the *EOS*, as shown in Equation 5.7, with the current porosity, α, which depends on the porosity of the undamaged concrete, α_{porous}, the hydrostatic pressure, p, and a shape factor n, as defined in Equation 5.8; see also AUTODYN (2005) and Riedel (2000). The factors K_1, K_2, K_3, B_0 and B_1, are material parameters describing the shape of the *EOS* curve and e is the internal energy.

$$p = \frac{1}{\alpha} f(\alpha \cdot \rho, e) \tag{5.6}$$

$$f(\rho, e) = K_1\mu + K_2\mu^2 + K_3\mu^3 + (B_0 + B_1\mu)\rho_0 e$$
$$\text{where} \quad \mu = \left(\frac{\rho}{\rho_0} - 1\right) \tag{5.7}$$

$$\alpha = 1 + (\alpha_{porous} - 1)\left[\frac{p_{solid} - p}{p_{solid} - p_{compaction}}\right]^n \tag{5.8}$$

5.2 Numerical solver technique

Here brief descriptions of the numerical techniques of Lagrange and Euler, used to simulate structural materials in AUTODYN 2D and 3D, are given. The main stress is, however, laid on the Lagrange solver since this is used in the numerical studies presented in Chapters 6 and 7. For information about other numerical techniques, often used in simulations of blast and fragment impacts (e.g. ALE and SPH), the reader is referred to AUTODYN (2005) and Leppänen (2004).

The most obvious difference between the Lagrange and Euler solver techniques is the coupling between the material and the numerical mesh. In a Lagrange solver the numerical mesh moves and distorts with the material, while the numerical mesh in an Euler solver is fixed in space and the material moves in, and between, the mesh elements; see Figure 5.3.

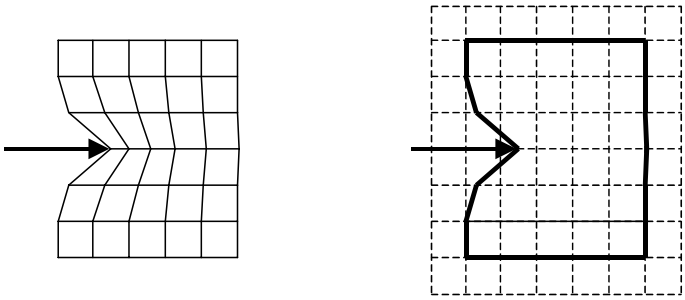

Figure 5.3 The Lagrangian description (left) and the Eulerian description (right) for material movement, from Leppänen (2004).

For a Lagrangian solver, distortion of the mesh can lead to inaccurate and ineffective solutions. Since AUTODYN uses explicit solving, the time-step size must be limited in order to achieve stable solutions. The maximum allowed time-step is often defined as a function of the minimum length of an element, or equivalent to this. For an elongating element, the time-step decreases and may cause extended computational time. In a Lagrangian mesh the positions, velocities, and material accelerations for an element are defined at the element nodes, situated in the element corners. Material quantities such as pressure, density, internal energy, stress and strain deviators and temperature are, on the other hand, defined at element-zone centres by centred differencing. Due to accuracy losses in the centred differencing, an element with high aspect ratio, i.e. large difference in length of its sides, may lead to loss of solution accuracy.

To overcome these numerical problems, rezoning or erosion algorithms may be used. Rezoning means that the distorted mesh is remapped onto a new, more regular mesh. However, an interactive rezoning is only available for Lagrangian elements in AUTODYN 2D, but not in the three-dimensional version. The erosion algorithm is implemented in both AUTODYN 2D and 3D and removes numerical elements if a pre-defined strain exceeds a specified limit. The mass of the eroded element can either be discarded or retained in the solution by distributing it to the corner nodes, which act as free mass points, and can then still interact with other elements, in another or the original body. However, the compressive strength and internal energy of the material within the eroded element cannot be compensated.

The Lagrangian solver can be used to advantage for simulations of solid continua and structures involving relatively small distortions, but may also be extended to highly distorted phenomenon with use of a rezoning or erosion algorithm. According to AUTODYN (2005), it is recommended to use the Euler solver technique for problems involving large deformations. Since the mesh is fixed in the Eulerian solver large deformations does not cause mesh distortion and there is no need for erosion of elements However, the Euler solver technique tends to be computationally more expensive than the Lagrange solver technique due to the transport of material between the mesh elements.

5.3 Mesh dependence

It is well known that the choice of numerical mesh geometries influences the results of numerical simulations. Since the basic equations used in the solver process for hydrocodes, and other similar codes, are based on infinitely small differences, it is obvious that large elements result in less accurate solutions. The mesh dependence can also arise from different assumptions and simplifications within the material model or numerical-solution process.

AUTODYN uses a smeared crack model, where the strain is decomposed into an elastic and an inelastic part, often referred to as the crack strain. The crack strain is calculated by smearing out the deformation, i.e. crack opening w, over a crack extension length, l_{el}, representing the element size. The length l_{el} is calculated in AUTODYN 3D as the diameter of a sphere, which has the same volume as the three-dimensional element.

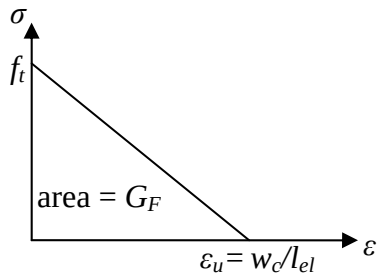

Figure 5.4 Linear crack softening relation used in AUTODYN.

In the principal-stress tensile-failure model, with crack-softening option, the fracture energy is given as an input parameter. As mentioned in Section 5.1.1, a linear crack-softening behaviour, shown in Figure 5.4, is used in AUTODYN, whence the relation between the fracture energy, G_F, and the ultimate crack strain (corresponding to the critical crack opening w_c), ε_u, can be expressed as:

$$\varepsilon_u = \frac{2\,G_F}{f_t\;l_{el}} \tag{5.9}$$

or after rearrangement:

$$G_F = \frac{f_t\;\varepsilon_u\;l_{el}}{2} \tag{5.10}$$

In the standard RHT material model, where the hydrodynamic tensile failure model is used and a limit on the crack strain is set to 1% in the damage model (as described in Section 5.1.1), the post-failure behaviour is the same for all element sizes, meaning that the value of the fracture energy is greatly mesh dependent. In Figure 5.5 the linear post-failure response calculated according to Equation 5.9 (with G_F = 100 Nm/m^2 and f_t = 3.5 MPa), of cubes with different sizes (1.0, 2.5, 5 and 10 mm) are shown, together with the post-failure response for a cubic element simulated with the RHT model.

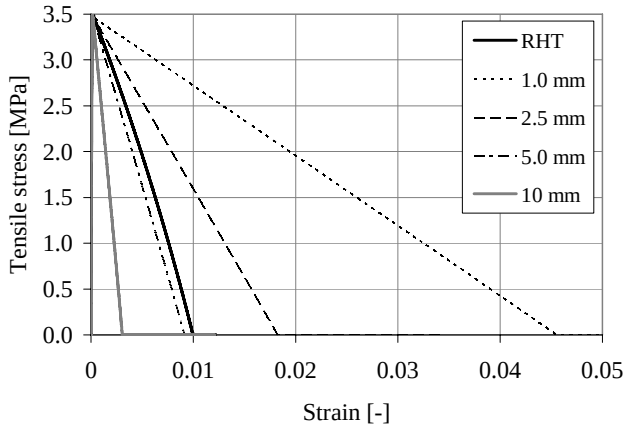

Figure 5.5 *Stress-strain relation for uni-axial tension for RHT (with no strain-rate dependence of the tensile strength) and linear softening relation for different element sizes.*

As seen in Figure 5.5, the relation for the softening behaviour is approximately linear also for the RHT model and the fracture energy corresponding to different element sizes in the RHT model can thus be estimated with Equation 5.10; see Table 5.1. For an element size of 5 mm the fracture energy calculated according to the RHT model agrees with that corresponding to normal-strength concrete, for larger elements the fracture energy is overestimated and for small elements underestimated.

Table 5.1 *Estimations of fracture energy used in RHT material model for different element sizes, calculated by means of Equation 5.10. Tensile strength of 3.5 MPa is assumed.*

Element length [mm]	l_{el} [mm]	G_F [Nm/m^2]
1	1.24	21.7
2.5	3.10	54.3
5	6.20	109
10	12.4	217
15	18.6	326

It is clear that a larger number of small elements are able to make a better description of deformed bodies than a lower number of larger elements. This is important for simulations of, for example, impact and penetration phenomenon. Zukas and Scheffler (2000) concluded, after numerical studies of projectile impact on concrete, that there should be at least three elements in the impacted target per radius of the impacting projectile to achieve accuracy in the simulations. However, in cases where the overall damage caused by the impacting body is of interest instead of the exact

lapse of the penetration process, it may be accurate enough to use larger elements. This is further discussed in Section 7.2.2.

As the failure surface is reached in an element, localisation takes place, meaning that the deformation is localised to this element and the surrounding mesh elements are elastically unloaded. All the plastic deformations occur in the localised element, until the ultimate plastic strain is reached. Since the strain rate is calculated as the change in strain during a time step, where the strain is related to the element size, as discussed earlier, the strain rate will be mesh-dependent after localisation. The smaller the element in which the localisation takes place, the higher the strain rate becomes after localisation. Hence, it becomes difficult to properly use a strain-rate criterion in an element where localisation has occurred. This effect, however, is minimised by use of a cut-off criterion limiting the tensile stress after failure initiation to exceed the tensile failure stress; see Leppänen (2004).

6 Effect of Steel Fibres in Concrete

The increased impact resistance of fibre-reinforced concrete, compared to plain concrete, has been observed in several experiments, e.g. Nataraja *et al.* (2005). Since often only a few variables, e.g. fibre type and its volume fraction, can be studied per experiment, and due to the complexity of the impacting phenomenon itself it is difficult to draw generic conclusions from these tests. By means of a numerical simulation tool the influence of different parameters can be studied in a more cost-effective way.

In order to investigate how the addition of fibres in concrete, and the consequently enhanced energy-absorbing characteristics described in Section 2.2, influence the projectile resistance of a structure, numerical simulations were conducted. These simulations include projectile impacts on plain and fibre-reinforced concrete targets. The simulations, their numerical model and results are mainly described in Paper I, even though a brief presentation is given in this chapter as well. However, due to limitations in the numerical model, which are discussed in this chapter, this study should be seen as a generic study indicating the relative effect of the fibres.

The basic setup of the simulations, i.e. the geometry and characteristics of target and projectile, was the same as used in an experiment of projectile impacts on plain concrete performed at the Swedish Defence Research Agency (FOI) in 1998; see Hansson (1998). This experiment was used to validate the numerical model of plain concrete, which in turn was used to study how different assumptions and simplifications needed in the simulations of fibre-reinforced concrete influenced the results. In order to study also how the addition of fibres influenced the formation of scabbing craters, the length and projectile geometry were varied in the simulations.

6.1 Materials used in study

Modelling of the discrete fibres within the concrete mix would require extensive work with the numerical mesh and complex descriptions of the fibre-concrete interface behaviour, so the fibre-reinforced concrete was modelled as one material. Since only moderate dosages of fibres (<1%) were used in the simulations, their influence was limited to an enhanced post-crack behaviour compared to plain concrete. The post-crack behaviour for the fibre-reinforced concretes (called FRC) was characterised by their fracture energies, for which approximate values of the corresponding volume fractions of end-hooked steel fibres were calculated according to Löfgren (2005); see Section 2.2.

The fracture energy of the plain concrete (called NSC) was estimated to 100 Nm/m^2 and three different fibre-reinforced concretes (called FRC1, FRC2 and FRC3) with fracture energies of 2000, 4000 and 6000 Nm/m^2, corresponding to steel-fibre volume fractions of approximately 0.20, 0.50 and 0.75%, respectively, were used in the simulations. As discussed in Sections 2.1 and 2.2 different relations between the stress and crack opening are proposed for both plain and fibre-reinforced concrete, but it was here assumed that the bi-linear relations are accurate enough in both cases. The bi-linear stress-crack opening relation proposed by Gylltoft (1983) was used for plain

concrete and the one proposed by Löfgren (2005) was used for the fibre-reinforced concretes. These stress-crack opening relations for the plain and fibre-reinforced concretes are shown in Figure 6.1.

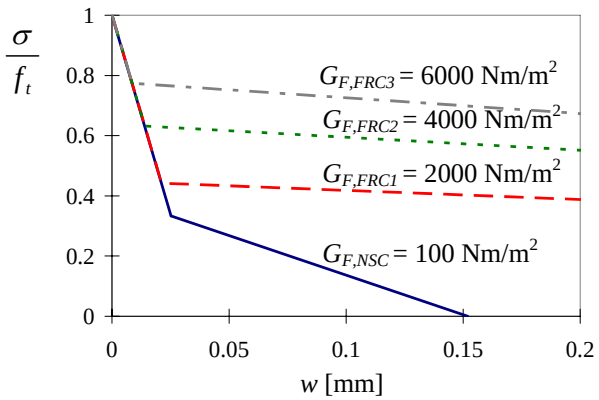

Figure 6.1 Crack softening for concrete NSC, FRC1, FRC2 and FRC3.

6.2 Limitations of numerical model

Since the influence of adding fibres into the concrete mix was limited to improved post-crack behaviour in the simulations and since bi-linear relations were used to describe the crack softening, it was necessary to use a principal-stress tensile-failure model, as discussed in Section 5.1.1. As a consequence the tensile strength was no longer strain-rate-dependent. An attempt to reintroduce the strain-rate dependence in tension was made by adding it in the user-subroutine used for the modified crack-softening behaviour. However, it was found impossible to reintroduce this dependence without getting unwanted effects on the crack-softening behaviour, since the user-defined tensile strength is employed only if it falls inside the RHT failure surface.

In the RHT constitutive model a parameter δ is used to describe the strain-rate effect on the tensile strength. By default this value is set to 0.036 and if δ equals zero the strain-rate dependence is turned off. In order to introduce a stepwise linear simplification of a DIF relation proposed by Malvar and Ross (1998), a high value of the δ-parameter must be used to prevent the tensile strength from falling outside the RHT failure surface. This is seen in Figure 6.2 where the simplified DIF relation used in the user-subroutine (*user-DIF*) is shown together with the DIF relation according to the RHT material model when δ equals 0.1 (*RHT-DIF*) and the results from uni-axial tensile simulations (*Results*). In the figure it can be seen that the desired DIF relation was followed up to a strain rate of approximately 50 s^{-1}.

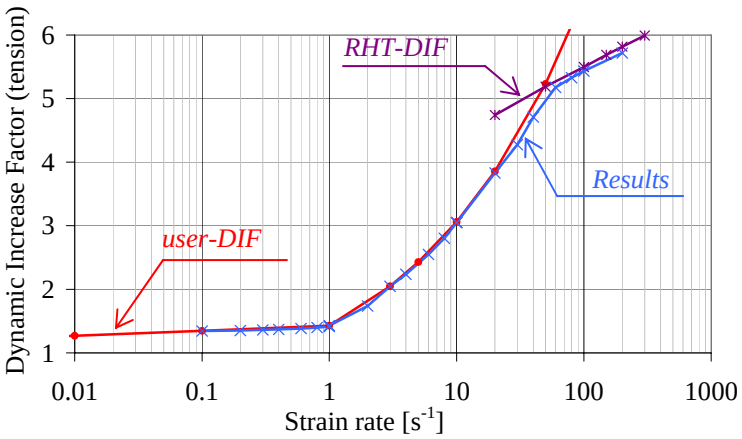

Figure 6.2 *DIF relations as implemented in user-subroutine and RHT constitutive model together with results from uni-axial tensile simulations.*

However, a high value of the δ-parameter leads to unstable solutions with the standard RHT constitutive model, leading to underestimated fracture energies. This can be seen in Figure 6.3, where the result from a uni-axial tensile simulation where $\delta = 0.1$ (*Result*) is shown together with the crack-softening relation defined in the user-subroutine (*Input*). Due to these problems it was chosen to disregard the strain-rate dependence of the tensile strength. For further discussion about the limitations of the study the reader is referred to Paper I.

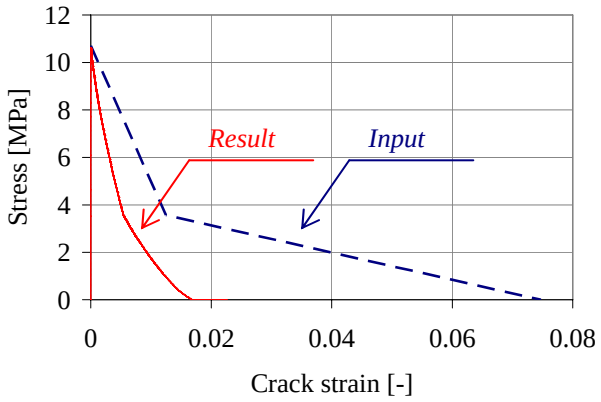

Figure 6.3 *Result from uni-axial tensile simulation and input relation used in sub-routine.*

6.3 Validation and influence of simplifications

As already mentioned, the basic numerical setup corresponded to the experimental setup presented in Hansson (1998), where 6.25 kg projectiles were fired into cylinders of plain concrete. The latter, 2.0 metres long and 1.6 metres wide, had a concrete strength of approximately 40 MPa (tested on 150 mm cubes) and were cast in a steel

culvert. The projectile had a length of 225 mm, a calibre of 75 mm and a striking velocity of 485 m/s. For further information about the experimental setup and the material properties the reader is referred to Paper I and Hansson (1998). The resulting depths of penetration were 655 and 660 mm and the diameters of the front-face craters were approximately 800 mm.

The simulations were conducted in AUTODYN 2D with axial symmetry and Lagrangian solver technique. Based on experience, the element size for the concrete was chosen to be 5 mm, see Figure 6.4, and a finer mesh was not believed to increase the accuracy of the results enough to be worth the increased computational time. The projectile and steel culvert were modelled with the von Mises material model and had a yield strength of 792 MPa, a linear *EOS* with bulk modulus of 159 GPa and a shear modulus of 81.8 GPa.

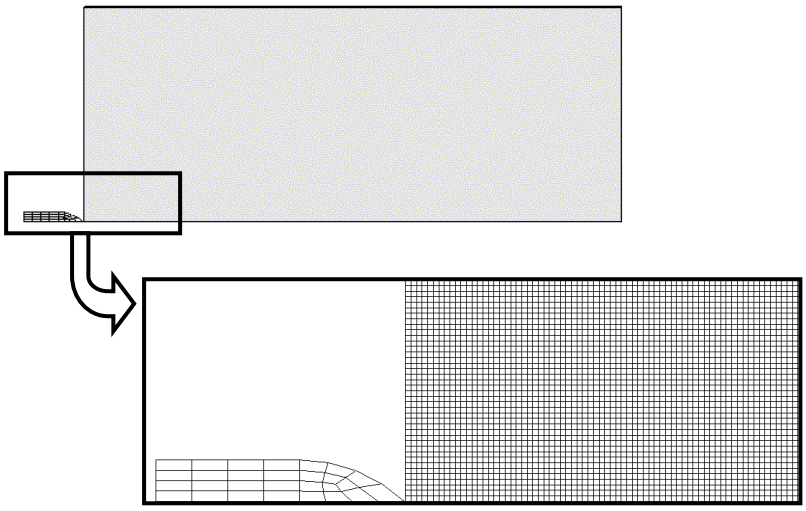

Figure 6.4 Numerical mesh for simulations with ogive-nosed projectile.

The standard RHT model was used for validation of the numerical model; the material parameters used are shown in Appendix A1 of Paper I. As seen in Figure 6.5, where the result of the simulation used for validation is shown together with the results from the experiment, both the depth of penetration, measured as the depth of fully damaged concrete, and the front-face crater size are accurately simulated.

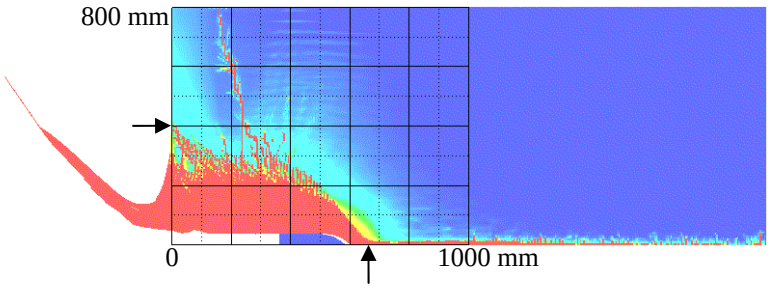

Figure 6.5 Simulation result for plain concrete with standard RHT material model and the experimental measurements indicated as arrows.

The change from the standard RHT material model to the modified RHT material model used in this study included:

- turning off the strain-rate dependence
- using a principal-stress tensile-failure model instead of the hydrodynamic tensile failure
- using a bi-linear crack-softening behaviour instead of a linear crack softening

The result of simulation with the modified RHT material model for plain concrete is shown in Figure 6.6. The depth of penetration is 960 mm and the front-face crater diameter is 1 020 mm, which exceeds the experimental measurements by 28 and 45%, respectively. Hence, this simulation does not show the real situation, but is anyway used to study the relative influence of adding fibres to the concrete.

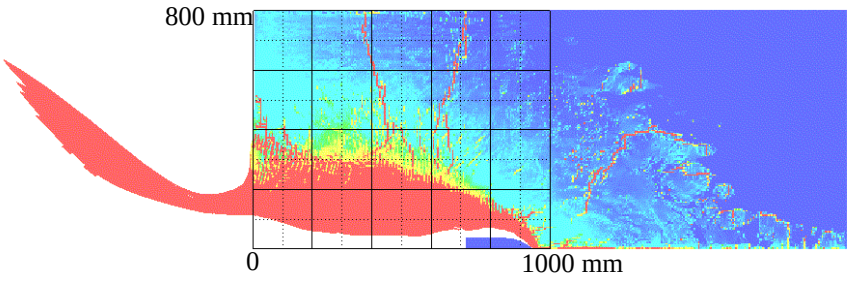

Figure 6.6 Simulation result for plain concrete with modified RHT material model.

6.4 Comparative study of addition of fibres

As mentioned in Section 6.1, three different fibre concretes, representing three different volume fractions of fibres, were used in this study. In order to study also how the addition of fibres in plain concrete influences the formation of a scabbing crater, shorter cylinders of 1.0, 1.1 and 1.3 metres were also used.

In Figure 6.7 the results for the three fibre concretes are shown, for the case of a 2.0 metre long cylinder. When comparing these results with the case of plain concrete (in Figure 6.6) it can be seen that the depth of penetration is negligibly influenced by the addition of fibres, while the influence on the front-face crater size is considerable. However, an increase of the volume fraction of fibres from 0.2% to 0.5 or 0.75% only leads to further small reductions of the front-face crater. The addition of fibres also gives a reduced crack propagation behind the crater region, so that damage becomes confined to a more localised volume; and in contrast to the front-face crater size, this effect is also seen when increasing the amount of fibres within the concrete.

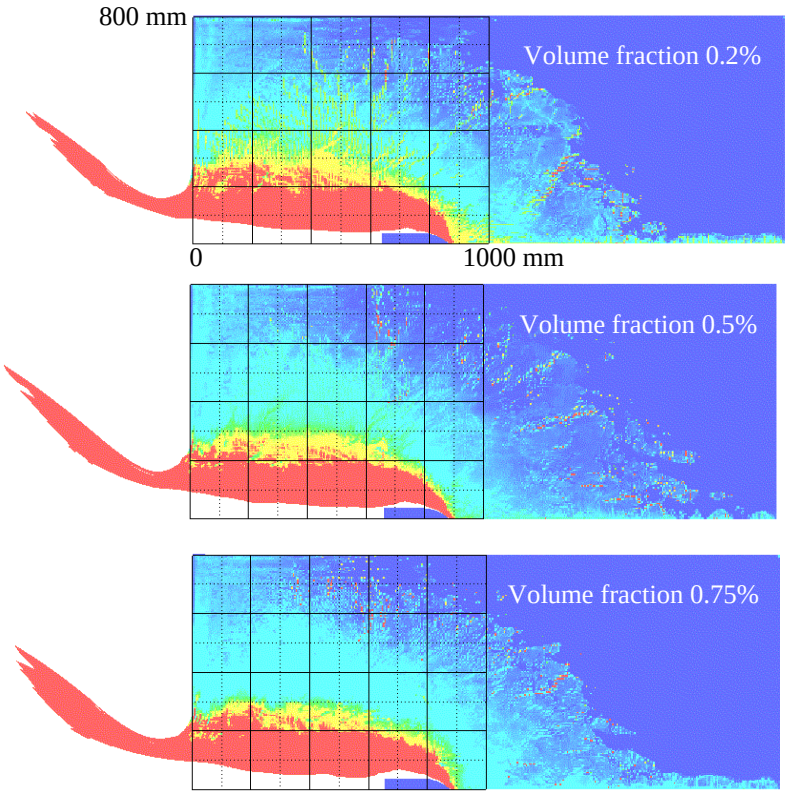

Figure 6.7 *Simulation result for fibre-reinforced concrete with volume fractions of 0.2, 0.5 and 0.75%. Target length of 2.0 m.*

Decreasing the length of the cylinder from 2.0 to 1.3 metres only leads to minor effects on the depth of penetration and the diameter of the front-face crater, as seen in Figure 6.8. Even though almost 75% of the target is penetrated, scabbing does not occur.

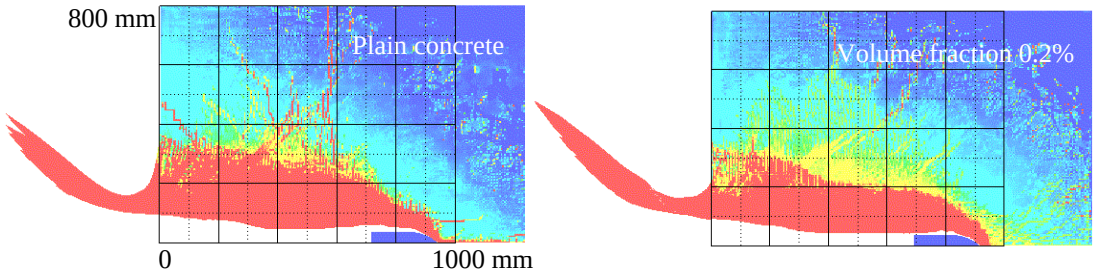

Figure 6.8 *Simulation result for plain concrete and fibre-reinforced concrete with volume fraction of 0.2%. Target length of 1.3 m.*

Further decrease of the target length, to 1.1 metre, does however lead to scabbing for all concretes, i.e. plain and all three fibre-reinforced concretes, as seen in Figure 6.9. But this scabbing effect cannot be differentiated from penetration since it is caused by the formation of a punching-shear plug; see Section 4.1. It can again be concluded

that the addition of fibres leads to a decreased front-face crater diameter. The addition of fibres in plain concrete results in a large reduction of the rear-face crater size and, unlike the size of the front-face crater, the rear-face crater decreases also when increasing the volume fraction of fibres.

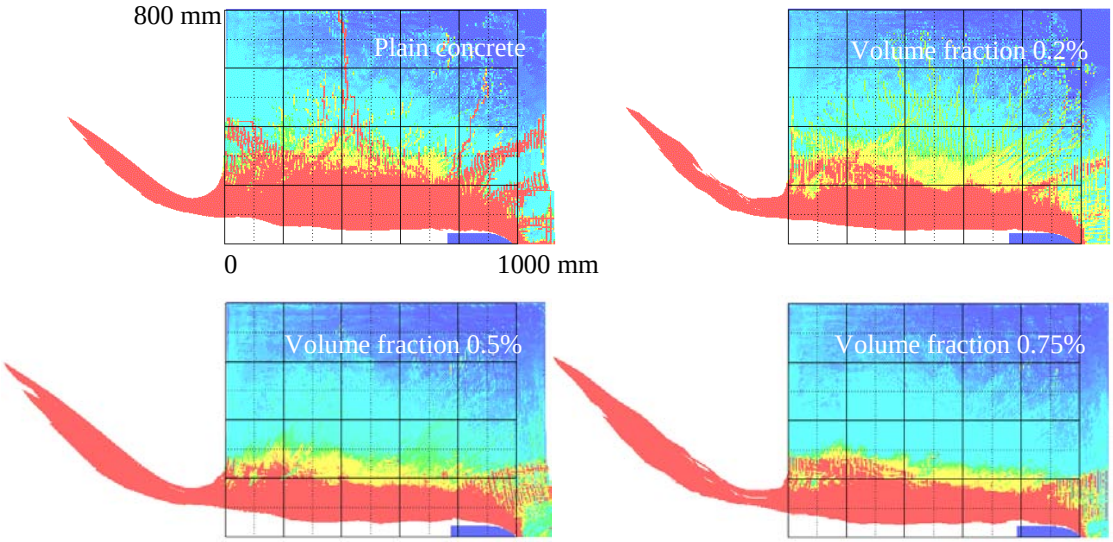

Figure 6.9 *Simulation result for plain concrete and fibre-reinforced concrete with volume fractions of 0.2, 0.5 and 0.75%. Target length of 1.1 m.*

In order to study the effect of fibres for scabbing caused only by the reflected stress wave and not in combination with plugging effects from the projectile, simulations of a 1.0 metre long cylinder subjected to impact by a flat-nosed projectile with striking velocity of 650 m/s were conducted. The results from these simulations are shown in Figure 6.10, where it can be seen that scabbing occurs for the plain-concrete target, but not for the cases with fibre-reinforced concretes. Even though crack initiation takes place at the rear ends due to the reflected stress wave also in the latter cases, the effect of the fibres prevents the initiated crack from developing into a continuous crack, which causes scabbing, as in the case of plain concrete.

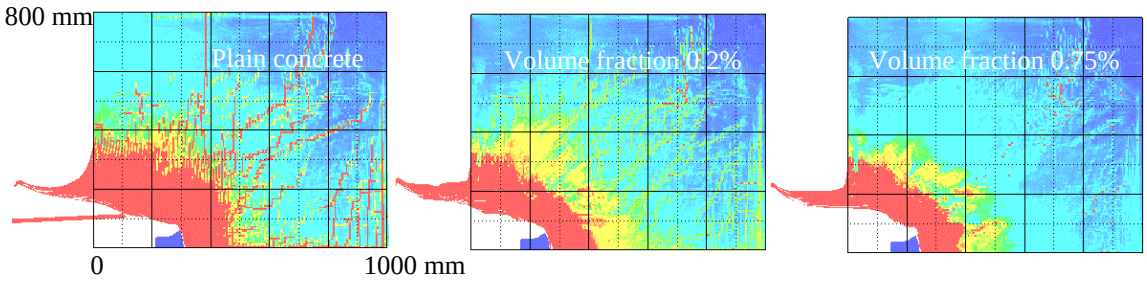

Figure 6.10 *Simulation result for plain concrete and fibre-reinforced concrete with volume fractions of 0.2 and 0.75%. Target length of 1.0 m.*

The scabbing cracks formed at the rear face of the cylinder with plain concrete can be seen in Figure 6.11, where the node velocity vectors are shown. The scabbing crack is seen as the outermost opened crack (indicated with the colour red) along the rear face of the concrete body. Since the velocity is higher on the right side of the crack than on the left side, and the concrete in between is fully damaged, and thus cannot transfer tensile stresses, scabbing occurs. The velocity of the scabbed concrete, relative the velocity on the left side of the crack is approximately 1.5 m/s. This is a low velocity in its connection, but shows the relative behaviour.

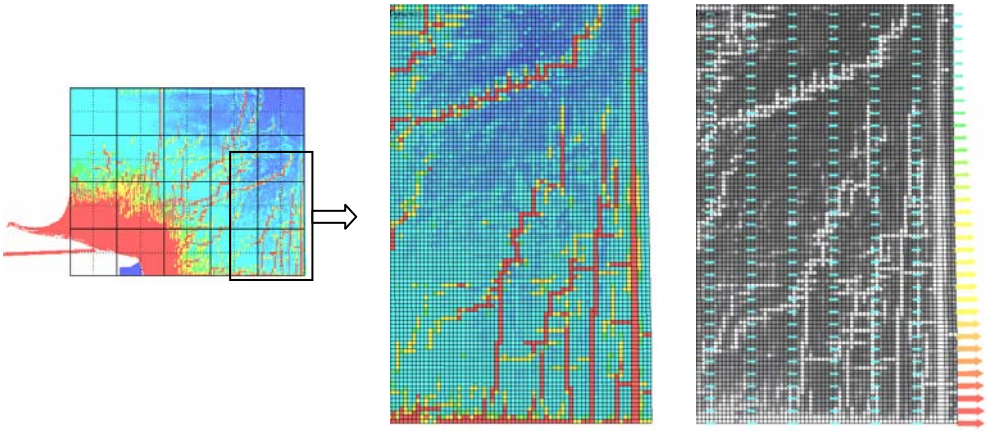

Figure 6.11 Scabbing crack in plain concrete, shown with velocity vectors.

7 Blast and Fragment Loading

A numerical study of the weapon effect on a reinforced concrete wall element was conducted; see also Paper II. The aim of the study was to further increase the knowledge of reinforced concrete structures exposed to explosions, i.e. blast and fragments. The geometry of the wall and the load characteristics were based on the regulations for civil defence shelters in Sweden.

7.1 Wall element and load characteristics

7.1.1 Design criteria for civil defence shelters in Sweden

The Swedish Shelter Regulations, Ekengren (2006), regulate the design of civil defence shelters in Sweden and contain the requirements specified for these protective structures. Civil defence shelters are designed not only to withstand conventional-weapon effects, but also radioactive radiation, chemical and biological warfare and explosive gas, etc. However, in this section only the requirements of protective capacity linked to conventional weapons effects are specified; for further information see Ekengren (2006).

According to Ekengren (1994): *"The shelter shall, with negligible risk to the occupants in need of shelter of being killed or injured, be able to withstand the effect of a pressure wave corresponding to that produced by a 250 kilograms GP-bomb with 50 weight per cent TNT which bursts freely outside at a distance of 5.0 meters from the outside of the shelter during free pressure release"*. Furthermore, *"The shelter shall, with negligible risk to the occupants of the shelter of being killed or seriously injured, also be able to withstand the effect of splinter from a burst bomb as above."*

In the case of fragment loading it is the fragment cluster that should be considered, while larger individual fragments are allowed to damage and penetrate the shelter structure.

In the Swedish Shelter Regulations, the civil defence shelter is assumed to be a reinforced, solid concrete structure. The concrete must be of at least strength class C25/30 according to BBK04, Boverket (2004), and hot-rolled reinforcement bars with a specified requirement of the strain hardening must be used. In order to fulfil the requirements of protective capacity, minimum concrete thicknesses and reinforcement contents are specified. The minimum concrete thicknesses for the shelter roof, floor and walls are 350, 200 and 350 mm, respectively, for a shelter without backfilling. The minimum and maximum values of reinforcement content are 0.14 and 1.10%, respectively. The reinforcement is to be placed in two perpendicular alignments in both edges of the structural element, with a maximum concrete cover of 50 mm. A minimum reinforcement-bar diameter of 10 mm and maximum bar spacing of 200 mm are required.

7.1.2 Wall element

When designing a civil defence shelter according to the Swedish Shelter Regulations, equivalent static loads are used. The equivalent static load representing the weapon effect is given as long-term pressures, both positive and negative, applied to the walls and roof. The positive static equivalent load (50 kN/m^2) was used to calculate the required amount of reinforcement in the wall, giving reinforcement bars ø10 s170 mm (equalling 465 mm^2/m in each face). The geometry of the shelter chosen for this study is shown in Figure 7.1.

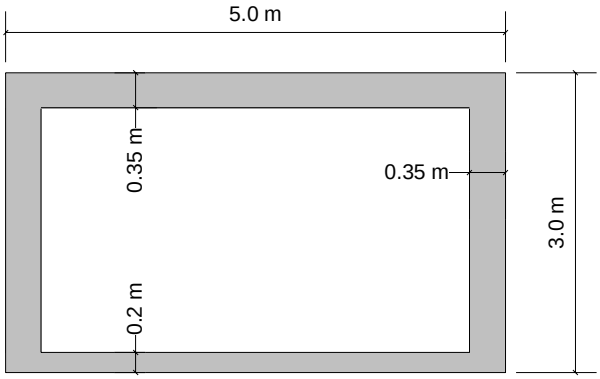

Figure 7.1 Civil defence shelter.

Since the response of one-way slabs, or slabs that reasonably approximate the behaviour of one-way slabs, can be analysed by simulating the response of a beam, representing a unit width of the slab ACSE (1999), it was first chosen to study a metre-wide strip of the wall. However, due to the heavy numerical model corresponding to this choice only a 170 mm wide strip was simulated; this choice is further discussed in Section 7.4.

In order to further simplify the analysis the wall strip was regarded as simply supported, as shown in Figure 7.2. It should, however, be pointed out that this was not done in an attempt to imitate the real support condition, which is more semi-rigid, but only to simplify the numerical model and decrease the complexity of the behaviour.

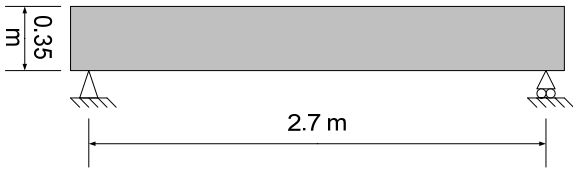

Figure 7.2 Simplified model of wall in civil defence shelter (Figure 7.1), rotated 90 degrees.

7.1.3 Loading definitions

The blast load caused by a detonation of a cased charge differs from that caused by an uncased charge since, in the former instance, energy is required to fracture the casing. As discussed in Section 2.3, it is common to approximate the total impulse from blast and fragment loading as the impulse caused by a bare burst with the same weight of explosive. This means that the difference in impulse for the blast wave caused by a cased charge and a bare charge with the same weight of explosive filling is assumed to correspond to the impulse caused by the fragment impact. Nevertheless, the blast load corresponding to a bare charge of the same weight as the cased charge was used in this study.

The blast load from a 125 kg bare charge of TNT, at a stand-off of 5.0 metres, calculated with the software ConWep (1992) is shown in Figure 7.3 together with the simplified relation used in this study. The blast load is assumed to be uniformly distributed over the wall and possible diffraction effects are disregarded. The blast load has an impulse density of 2 795 Ns/m^2.

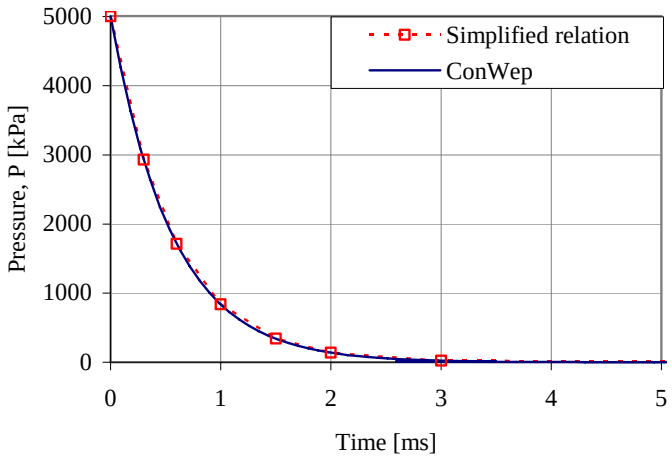

Time [ms]	Pressure [kPa]
0.0	5 006
0.3	2 930
0.6	1 713
1.0	836
1.5	340
2.0	137
3.0	22
8.974	0

Figure 7.3 Pressure load as function of time for 125 kg TNT at a distance of 5.0 metres, according to ConWep (1992), and the simplified relation used in the study.

The fragments caused by the GP-bomb, referred to in the Swedish Shelter Regulations, are more difficult to characterise, since neither the geometry of the bomb nor the thickness of the casing is defined. Hence, the fragment distribution factor, M_A, in Equation 2.5 to determine the mass distribution cannot be calculated. However, the fragment distribution factor of the American GP-bomb Mk82, found in Krauthammer (2006), was used to estimate the fragment distribution factor of the bomb referred to in the Swedish Shelter Regulations, by adjusting for the increased charge volume. The Mk82 has a nominal weight of 500 lb (226.8 kg) and contains 192.0 lb (87.09 kg) of the high-explosive H-6, corresponding to 242.9 lb (110.2 kg) equivalent weight of TNT, and is therefore rather representative for the GP-bomb specified in the Swedish Shelter Regulations.

In order to simplify the simulations and the analyses of their results, it was determined to use the same weight and shape for all the fragments striking the wall. This is obviously a rough idealisation of the real situation, where the range of the fragment mass may be wide and the shape of the fragments may differ considerably, at least for bombs whose casing is not fracturing in a pre-defined pattern. The casing material was assumed to be made of steel and the fragments were assumed to be spherical in shape; thus, after determination of the mass of this design fragment, it was possible to calculate the corresponding diameter of the fragments.

As it is the cluster of fragments that should be considered, it is not the heaviest individual fragment that has the worst effect, but the total impulse caused by the fragments in combination with the local damage of their impact. Hence, the method of using a confidence level to determine the mass of the design fragment (see Section 3.2.1) is not applicable for this case. Instead an impulse distribution for the fragments was determined, by use of the mass distribution and the striking velocity corresponding to each mass (see Equation 3.5 and 3.8), and the mass corresponding to the mean impulse for all fragments was used as the design fragment weight; see Appendix C. The mass of the design fragment for the specified bomb was thereby estimated to be 21.9 grams, and the corresponding diameter and striking velocity were calculated to be 17.5 mm and 1 760 m/s, respectively.

Since the shape of the bomb is not spherical, the distribution of the fragments in the surroundings of the bomb will also differ depending on the position relative to the bomb, as discussed in Section 3.2.3. As the geometry and configuration of the specified bomb are not known, rough estimations of the fragment distribution based on test data were made. In Forsén and Sten (1994), a comparison of the fragment distribution for the two 250 kg GP-bombs Mk 82 and m/50, with test data on the fragment distribution at different angles relative to the axis of the bombs, is presented. In a rough compilation of these data, it was found that fragments with a total mass equalling approximately 60% of the casing mass were found within a sector of ±20 degrees for the two bombs, where the angles are measured relative to the normal to the longitudinal axis of the bomb, as shown in Figure 7.4. This means that the worst fragment-loading situation is, for this idealised bomb, when the bomb is vertically directed with its centre at the same height as the middle of the wall. Assuming this position of the bomb, the numbers of design fragments striking the wall can be calculated by projection. The fragment density is approximately 0.66 kg/m^2 and the corresponding impulse density is 1 125 Ns/m^2.

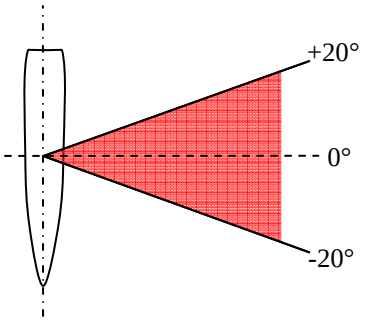

Figure 7.4 *For the two GP-bombs Mk82 and m/50 approximately 60% of the fragment mass was found within ± 20 degrees, relative to the normal to the longitudinal axis of the bombs.*

As further simplifications in the numerical simulations, the fragments are assumed to be uniformly distributed over the wall, and to strike the wall at the same time at perpendicular angle relative to the wall surface.

7.2 Preliminary study

Simulations of blast and fragment loading may place different, and sometimes conflicting, demands on the numerical model, e.g. the numerical solving technique, material model and numerical mesh. In order to calibrate and validate the numerical model, a preliminary study was conducted prior to the main study of blast and fragment loading of the wall strip described in Section 7.1.2. The main objective of the preliminary study was to find a numerical model, i.e. material model and numerical mesh, which was a good compromise for describing the response of the wall strip subjected to both blast and fragment loading, simulated in the main study in Section 7.4.

In this preliminary study the blast and fragment loadings were treated separately to clarify how the responses, local for fragment impact and global for the blast load, are affected by the change of different parameters within the model. An experiment of blast-loaded concrete beams, presented in Magnusson and Hansson (2005), and an experiment of single fragment impacts on concrete blocks, conducted by Leppänen (2003), were used to validate the choices made in the numerical model. The fragment simulations in the preliminary study were made in AUTODYN 2D with axial symmetry, while the simulations of blast loading were made in AUTODYN 3D. However, the blast-loaded beams were modelled with a width of only one element and plane-strain boundary conditions in order to imitate a 2D simulation.

The findings from the preliminary study were then inferred and the numerical model used in the main study is based on these conclusions.

7.2.1 Blast loading

In Magnusson and Hallgren (2000) the test of reinforced concrete beams subjected to blast loading is presented. Magnusson and Hansson (2005) used AUTODYN 3D to simulate the response of these beams and compared different material models and their assumptions.

The configuration of the test beam, including reinforcement detailing, and the pressure-time relation for the blast load are shown in Figure 7.5 and Table 7.1, respectively. The concrete quality for the beam chosen for simulation was 50 MPa and the reinforcement was of type B500BT with a yield strength of 500 MPa. However, the stress-strain relationship for the reinforcing steel used in the numerical simulations was based on uni-axial tensile tests; see Magnusson and Hansson (2005). The stepwise-linear simplification of the stress-plastic strain relation from the test is presented in Table 7.2. Due to the test setup, the blast load did not apply to the outer 60 mm from each end of the beam. In the test, bolts were at the supports to stabilise the beam; but even though these bolts resulted in some degree of fixation, rotation could take place. The maximum mid-point deflection of the beam was measured to be approximately 23 mm and took place after 8 ms.

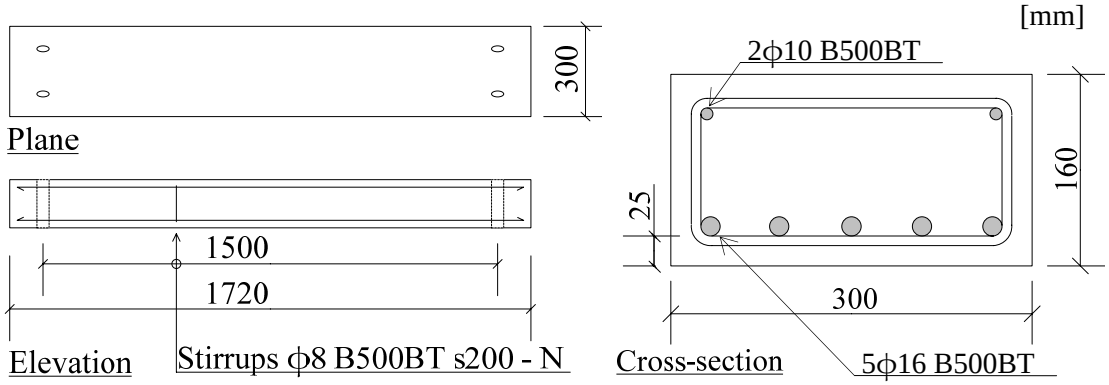

Figure 7.5 Test-beam configuration, based on Magnusson and Hallgren (2000).

Table 7.1 Simplified pressure-time relation for the blast load.

Point No.	1	2	3	4	5	6	7	8	9	10
Pressure [kPa]	0	1 100	810	580	750	390	485	280	100	0
Time [ms]	0	0.16	1.76	2.36	3.04	5.52	5.76	8.10	14.5	24.0

Table 7.2 Stress-plastic strain relation for reinforcement steel B500BT, presented by Magnusson and Hansson (2005).

Point No.	0	1	2	3	4	5	6	7	8
Stress [MPa]	549	562	568	627	678	715	746	776	795
Plastic strain [‰]	0	6.7	16.2	28.6	45.7	64.5	92.1	127.8	179.2

The concrete was modelled with cubic elements and the RHT material model. In order to reduce the size of the numerical model, only a one-element-wide part of the width of the beam was modelled. All the reinforcement bars were modelled with Johnson-Cook material model and, because of the limited width modelled, the dimensions of the tensile, compressive and shear reinforcement bars had to be adjusted so as still to represent the correct amount of reinforcement. The reinforcement bars were modelled with beam elements with the same length as the surrounding concrete elements. The numerical setup of the experiment is shown in Figure 7.6, where also the reinforcement bar diameters after adjustment to the limited width are specified.

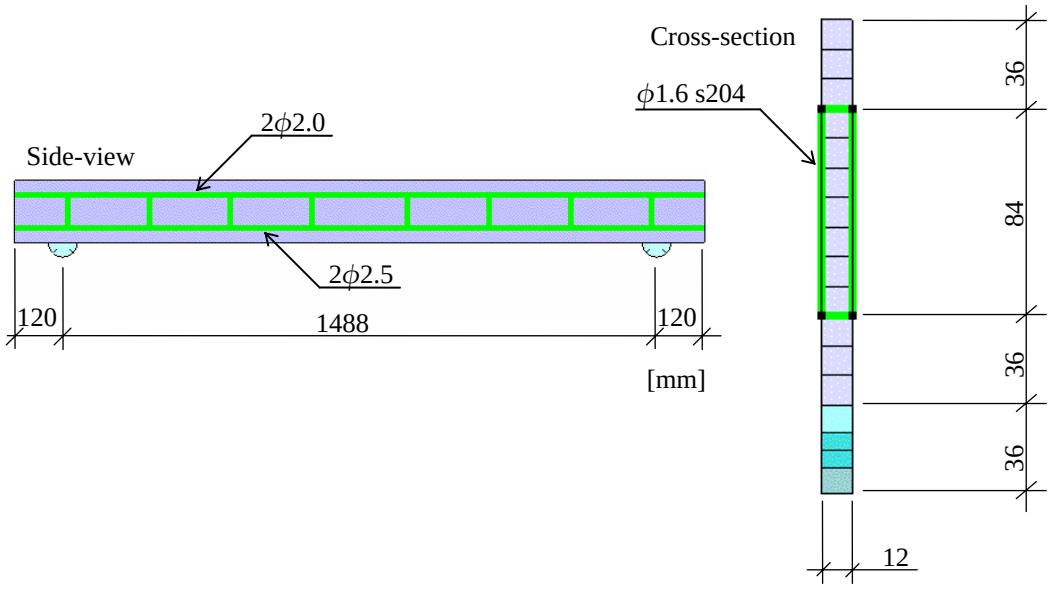

Figure 7.6 Numerical setup and adopted reinforcement bar dimensions.

Even though bolts were used to keep the beam somewhat fixed over the supports in the test, Magnusson and Hansson (2005) modelled the beam as simply supported. They concluded that the bolts had some, but not crucial, influence on the beam response. They also used three different geometries of the supports in their simulations together with different interaction criteria between the supports and the concrete (friction between the surfaces or nodes joined together). All three of these support configurations resulted in accurate beam responses, even though there was

some variation in the measured mid-point deflection and acceleration. Modelling with friction as interaction criterion resulted in somewhat reduced damage around the supports, compared to the results where the support and the concrete were joined together. Based on Magnusson and Hansson's (2005) results it was believed accurate enough to model the support as half-cylinders jointed together with the interfacing concrete.

The blast load was applied to the top surface of the beam by use of a stepwise-linear pressure boundary condition. It should, however, be observed that the load was not applied to the whole front surface due to the test configuration; hence, the load stops 60 mm from the beam end.

In order to calibrate the numerical model for the main study, the influences of tensile-failure model, flow rule, fracture energy and element size were studied, as seen in Table 7.3. The beam responses and the mid-point deflections are shown in Figure 7.7.

Table 7.3 Simulations of blast-loaded reinforced concrete beams, shown in Figure 7.7

Ident	Tensile failure model	Fracture energy [Nm/m^2]	Flow rule	Element size [mm]
BLAST001	Hydrodynamic	-	-	12
BLAST002	Principal stress	120	Non-associated	12
BLAST003	Principal stress	120	Associated	12
BLAST004	Principal stress	180	Associated	12
BLAST005	Principal stress	120	Associated	6*

* In this simulation the elements were no longer cubic since the width of the beam (12 mm) still was modelled with one element.

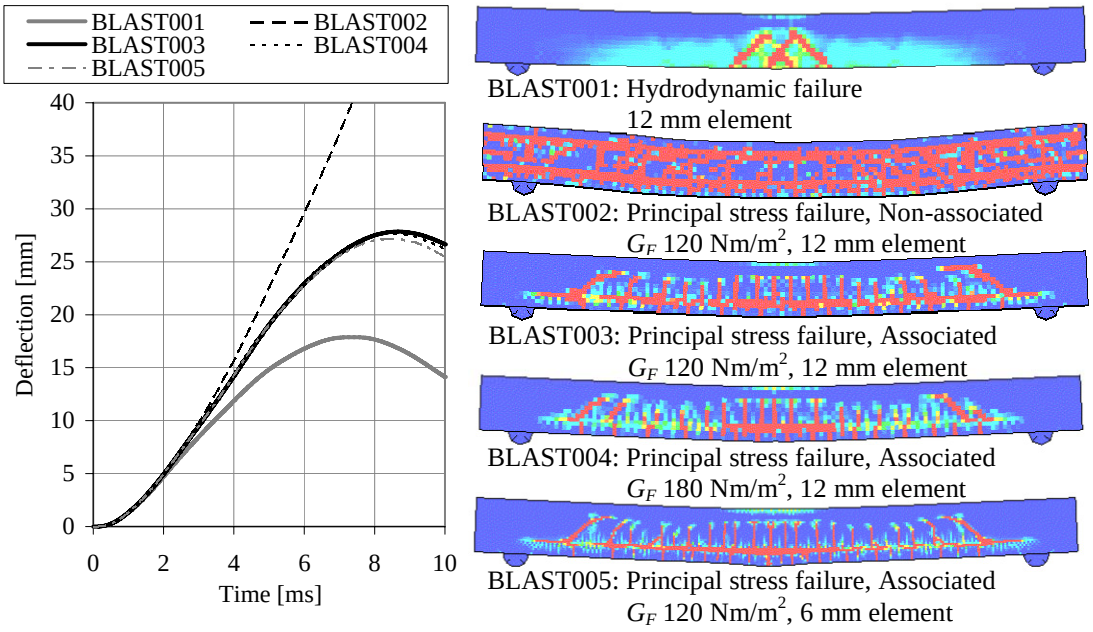

Figure 7.7 Mid-point deflections and beam responses for simulations in Table 7.3.

From the beam response results, shown in Figure 7.7, it was concluded that the use of the principal-stress tensile-failure model and an associated flow rule was necessary to get an accurate crack pattern in the beam. When the standard RHT material model was used, including the hydrodynamic tensile-failure model (simulation BLAST001), only a small number of cracks appear in the beam. This is probably, at least partly, a result of the limitation of the crack strain discussed in Section 5.3, giving an overestimated value of the fracture energy when an element size larger than approximately 5 mm is used. In AUTODYN a non-associated flow rule (in AUTODYN called No-Bulking) is used as default, since the choice of an associated flow rule may lead to excessive bulking of the material, according to AUTODYN (2005). This seems to be valid for simulations of penetration, while in the case of blast loading it leads to incorrect results of the beam response; this is in accordance with conclusions in Magnusson and Hansson (2005). However, acceptable estimations of the mid-point deflection were achieved in all simulations presented in Table 7.3, except for the simulation where a combination of principal-stress tensile-failure model and a non-associated flow law was used (simulation BLAST002), as seen in Figure 7.7. The displacement for simulations with relative good agreement the difference in deflection is limited to approximately ±20%.

7.2.2 Fragment impact

The influences of tensile-failure model, flow rule and element size for the concrete were studied also for single fragment impact on concrete. The experiment presented in Leppänen (2003, 2004) was used to validate the numerical model.

Leppänen (2003) tested concrete blocks subjected to single fragment impacts and fragment cluster impacts. In single fragment impact, which is the only situation presented here, the concrete block had the dimensions 750 x 375 x 500 mm (where

500 mm is the depth of the block). The compressive strength of the concrete was 31.2 MPa, tested on cylinders. Two or three fragment shots were fired against each concrete block, and the fragments, in total eight, had various striking velocities from 1 754 to 2 000 m/s. The fragments were steel point-bearing balls with a diameter of 8 mm. The mass is not specified in the test report, but should be approximately 2.1 grams. The depth of penetration varied between 52.5 and 57 mm and the diameter of the spalling craters was between 74 and 93 mm.

For the validation of the numerical model, which was to be used in the main study, shot number 4 as seen in Figure 7.8 was chosen. The striking velocity of this shot was 1 879 m/s and the resulting depth of penetration and diameter of the crater were 54 and 93 mm, respectively, as shown in the close-up of the damaged area for shot 4 in Figure 7.8.

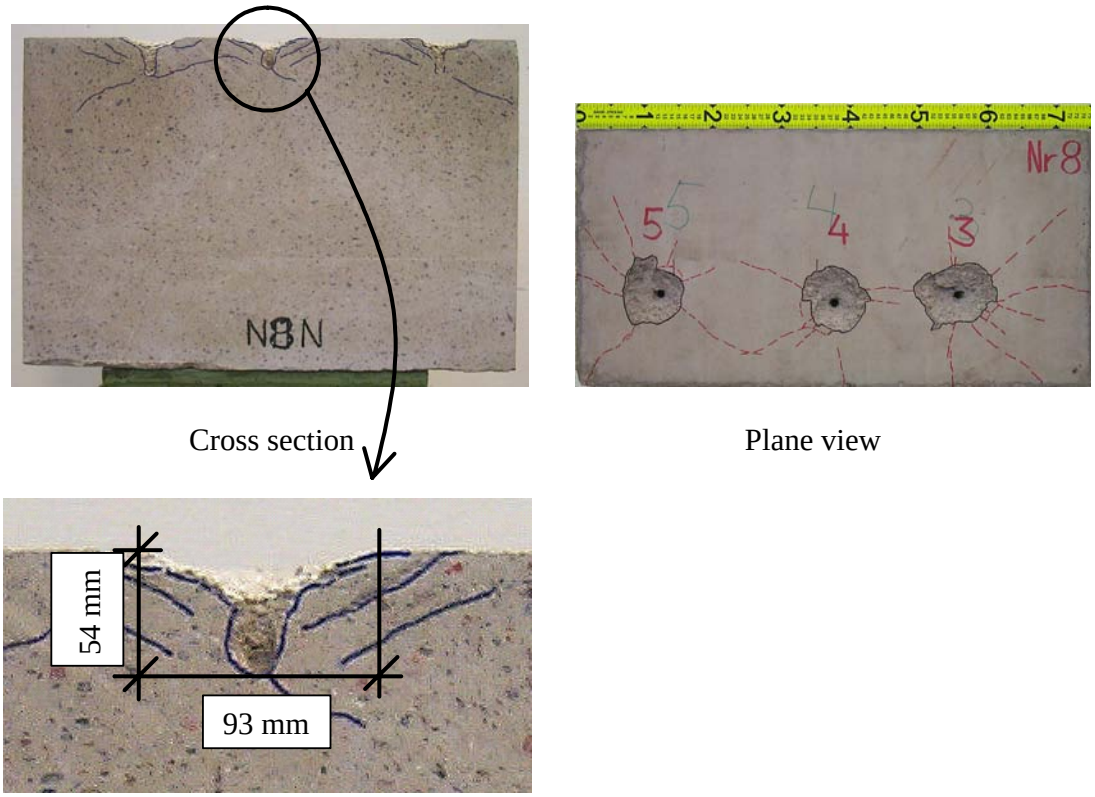

Figure 7.8 Experimental results from single fragment impact (cross-section, plane view and close-up of damage of shot number 4, from Leppänen 2004).

The simulations were made in AUTODYN 2D with axial symmetry. The concrete was modelled with the RHT material model, and the von Mises material model, with yield strength of 800 MPa, was used for the fragment. The simulations of single fragment impact conducted within the preliminary study are summarised in Table 7.4. The results from these simulations are shown in Figure 7.9.

Table 7.4 *Simulations of single fragment impact on concrete block, shown in Figure 7.9.*

Ident	Tensile failure model	Fracture energy [Nm/m^2]	Flow rule	Element size [mm]
FRAGM001	Hydrodynamic	-	-	1
FRAGM002	Principal stress	120	Non-associated	1
FRAGM003	Principal stress	120	Associated	1
FRAGM004	Principal stress	120	Associated	2

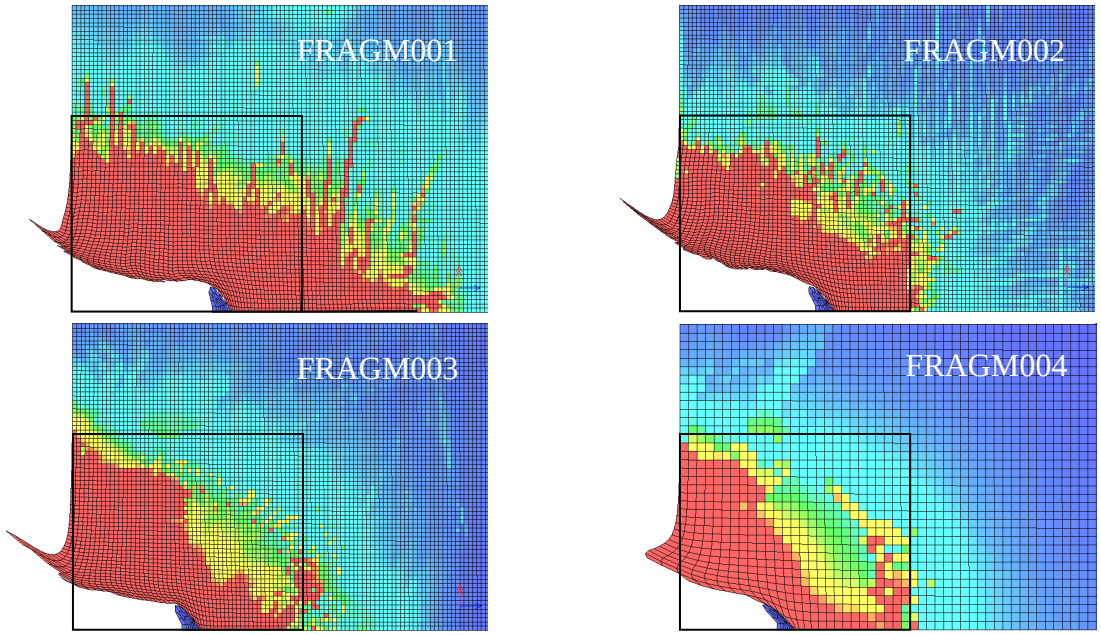

Figure 7.9 *Results from simulations of single fragment impacts, shown in Table 7.4. The squares indicate the damage measured in experiments (height 46.5 mm and length 54 mm). (Only a part of the numerical mesh is shown.)*

As the 1.0-mm elements and the standard RHT material model, with hydrodynamic tensile failure (FRAGM001), were used for the concrete, the simulated depth of penetration – measured as the depth of fully damaged concrete – was overestimated (90 mm compared with 54 mm in the test). Changing the tensile-failure model from hydrodynamic to principal stress with non-associated flow rule (FRAGM002), the depth of penetration decreased to 58 mm, and became more similar to that of the test. Since the simulation of blast loading requires an associated flow rule, also this alternative had to be tested (FRAGM003), and the depth of penetration again decreased somewhat (to 50 mm). Doubling the element size from 1 to 2 mm gave a small increase of the penetration depth to 52 mm, and was assumed to simulate reasonably well the damage caused by the fragment. The front-face crater diameter

differed between the simulations (ranging from 72 to 94 mm, compared with 93 mm in the test), but was accurately simulated in at least simulations FRAGM003 and FRAGM004.

Since the fragments used in the experiments conducted by Leppänen (2003) were small (8 mm diameter) compared to the fragments used in the main study (17.5 mm diameter) and a thick concrete block was simulated instead of a wall, additional simulations more similar to the conditions used in the main study were performed. In these additional simulations the influence of the element size was studied. The principal-stress tensile-failure model was used together with an associated flow rule and fracture energy of 120 Nm/m^2 for all these additional simulations.

The wall strip used in the main study had a thickness of 350 mm and a height of 3 metres, as shown in Figure 7.1. For the additional simulations these measurements were used. As mentioned in Section 5.3, Zukas and Scheffler (2000) concluded that at least three elements in the impacted target per radius of the impacting body should be used in the numerical mesh. In the simulations of single fragment impact discussed above, however, it was concluded that the damage could be reasonably simulated also with larger elements. In this additional study of single fragment impact, three element sizes were used, 2, 3 and 6 mm, named simulations FRAGM004, FRAGM005 and FRAGM006, respectively. The results from the additional simulations are summarised in Figure 7.10.

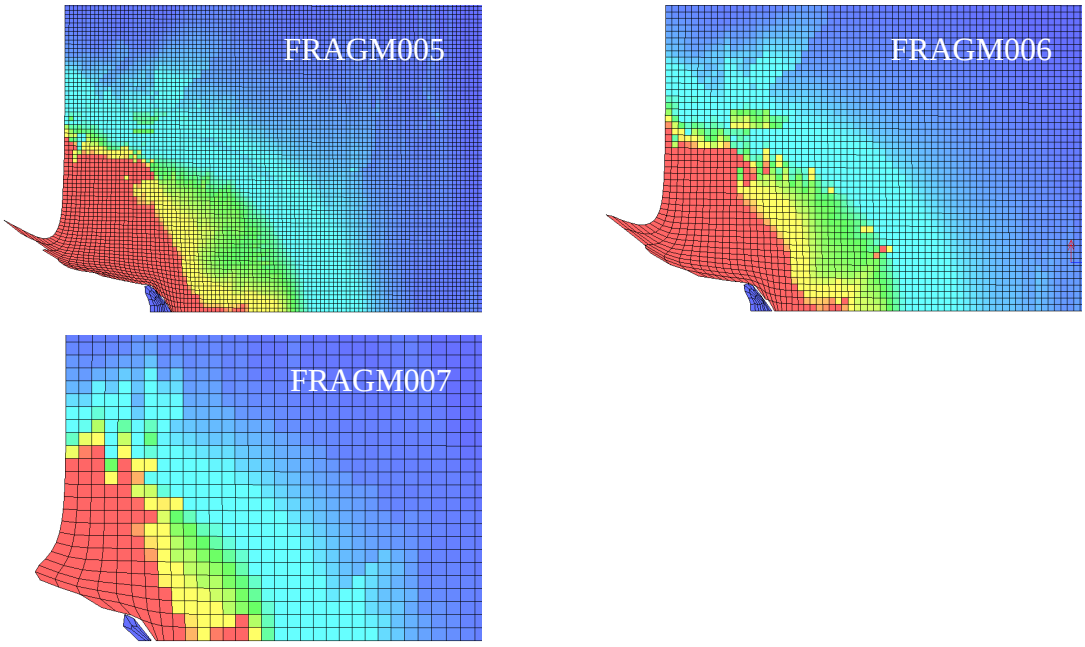

Figure 7.10 Results from additional simulations of fragment impacts.

Since the depth of penetration and front-face crater size do not differ much for the three simulations (FRAGM004 to FRAGM006), it was assumed that an element size of 6 mm could be used to estimate reasonably well the local damage caused by the fragment impact; see Figure 7.10.

7.2.3 Conclusions

In order to accurately simulate the beam response when loaded with a blast wave, an associated flow rule must be used; see Figure 7.7. The beam response, for blast loading, was accurately described when 12-mm elements were used, and halving the element size to 6 mm led to only small changes in the beam response.

The damage caused by an impacting fragment was most accurately simulated with the use of the principal-stress tensile-failure model and a non-associated flow rule. Since an associated flow rule is necessary to get accurate response in the case of blast loading, it must be used in the simulations of combined loading. As an associated flow rule was used in the simulations of fragment impact, the damage was somewhat underestimated, but still relatively well described. The local damage caused by the fragment impact is better described the smaller the elements are. However, for the fragment used in the main study an element size of 6 mm may still be used even though it is large compared to the radius of the impacting fragment. It must be pointed out that this is not believed to give an accurate description of the penetration process itself, but only to result in damage which approximates the damage caused by this impact in reality.

7.3 SDOF analyses

The SDOF method, described in Section 4.4, was used to estimate the mid-point deflection and velocity of the wall strip when subjected to blast and impact loading. With combined loading it was also of interest to find for which case the maximum deflection was attained: for simultaneous arrival of the two loads, for blast load arriving first or for fragments arriving first.

An ideal-plastic material behaviour was assumed and the maximum internal resistance R_m was calculated as the maximum static internal resistance times a factor 1.3, for taking into account dynamic effects in accordance with Forsén and Nordström (1992). This increase in load-bearing capacity for high dynamic loads, compared to static loads, is reported also by Magnusson and Hallgren (2000). Johansson (1999) also observed an increased load-bearing capacity in numerical simulations of shelter walls subjected to blast loading, and explained it by a normal force appearing in the loaded structural element. This normal force is probably related to internal momentum effects, and then appears even if the structural element studied is simply supported, as in this case. The maximum internal resistance was therefore calculated as:

$$R_m = 1.3\frac{8\,M_{Rd}}{L} \tag{7.1}$$

where M_{Rd} is the moment capacity of the wall strip for static loading and L is the length of the wall strip. The moment capacity calculated for the wall strip was 71 kNm.

In Figure 7.11 the mid-point deflection of the wall strip is seen for different configurations of arrival times in for combined loading. Five cases are presented:

1. Simultaneous loading
2. Blast arrives first, fragments arrive at time of maximum wall deflection
3. Blast arrives first, fragments arrive at time of maximum wall velocity
4. Fragments arrive first, blast arrives at time of maximum wall deflection
5. Fragments arrive first, blast arrives at time of maximum wall velocity

As seen in the figure, the case of simultaneous loading results in the maximum deflection.

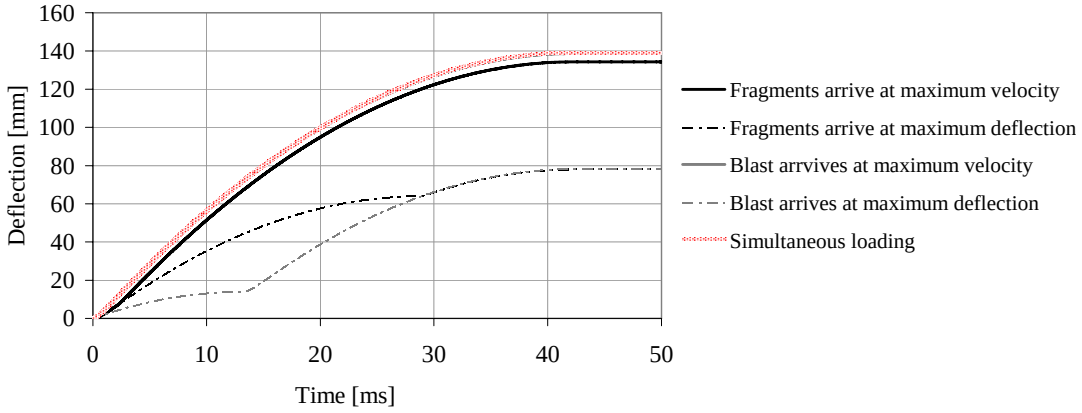

Figure 7.11 Mid-point deflection of wall strip subjected to combined loading with different times of arrivals of the loads. Estimated with the SDOF method. Since the responses in the case of simultaneous loading and the case of fragments arriving first and the blast arriving at time of maximum velocity are almost identical, these lines are seen as one in the figure.

The mid-point deflection of the wall strip, estimated with the SDOF method in the case of blast loading, fragment impact and the combination of these loads, is shown in Figure 7.12. Maximum deflection reached for blast loading is 64 mm and appears 29.0 ms after the arrival. For fragment impact the corresponding values are 13.9 mm at time 13.2 ms. In the case of combined, simultaneous loading the maximum deflection is reached after 42.2 ms and is 139.2 mm, which is very high compared to the other two cases.

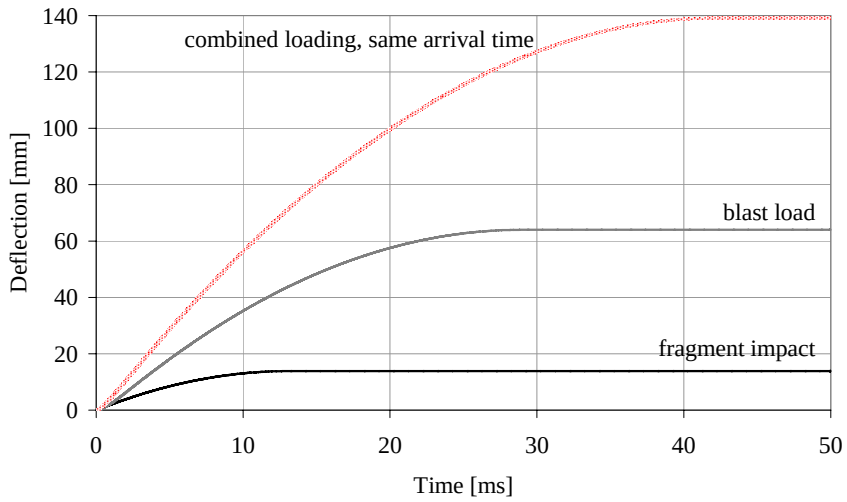

Figure 7.12 Mid-point deflection of wall strip subjected to blast load, fragment impact or combined, simultaneous loading of these. Estimated with the SDOF method.

As seen in Figure 7.13, the maximum mid-point velocity of the wall strip for combined loading (6.2 m/s) equals the sum of the maximum velocities in the cases of blast and fragment loading subjected separately to the beam, 2.1 and 4.1 m/s, respectively.

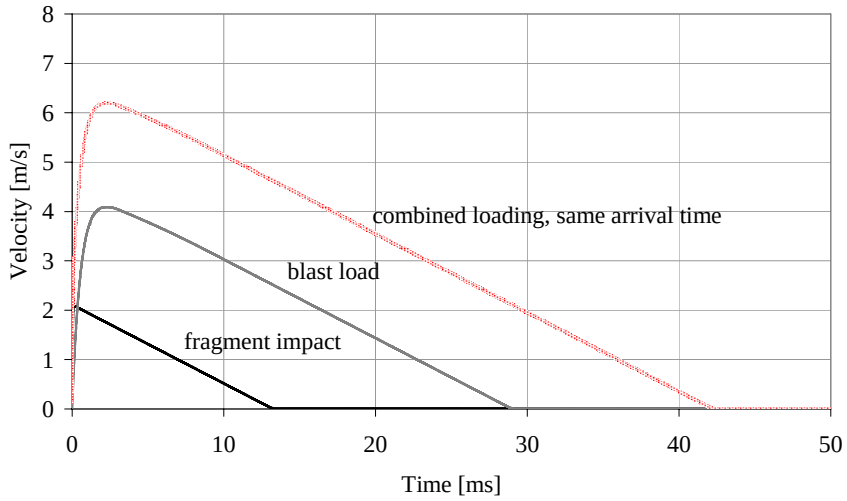

Figure 7.13 Mid-point velocity of wall strip subjected to blast load, fragment impact or combined, simultaneous loading of these. Estimated with the SDOF method.

7.4 Numerical analyses – main study

As shown in the preliminary study, Sections 7.2.1 and 7.2.2, the blast and fragment loading place different requirements on the numerical-mesh geometry and the flow rule used within the constitutive model. In order to conduct a numerical simulation of blast and fragment loading, it was therefore necessary to find a compromise for the numerical model, suitable to approximately describe the, local and global responses of the reinforced concrete wall described in Section 7.1.2.

A relatively fine numerical mesh is necessary to simulate fragment impact and the subsequent damage. In the preliminary study it was shown that an element size of 6 mm was fine enough to estimate the resulting damage, even though a finer mesh must be used to reproduce the real behaviour; see Section 7.2.2. The response of blast loading is, however, accurately simulated also for a coarser numerical mesh. The preliminary study showed that an element size of 12 mm gave accurate results. Since the direct damage (not including possible effects of the reflected stress wave) caused by the fragment impacts is limited to the front of the target, the fine mesh was used only here; see Figure 7.14. This was done to reduce the size of the numerical model, and thereby the computational time required for the simulations.

However, modelling the wall, or even a metre-wide strip of the wall, results in an excessively large numerical model. By use of symmetries and planar-strain boundary conditions the model was limited to a 84 x 1 512 x 350 mm part, representing 4.25% of a metre-wide wall strip. The mesh geometry for the numerical model of the reinforced concrete target used in the simulations described in subsequent sections is shown in Figure 7.14. The support was modelled in the same way as in the preliminary study of blast loading (see Section 7.2.1), i.e. as half-cylinders restricted from vertical movement, with linear-elastic material behaviour and full interaction with the adjacent concrete.

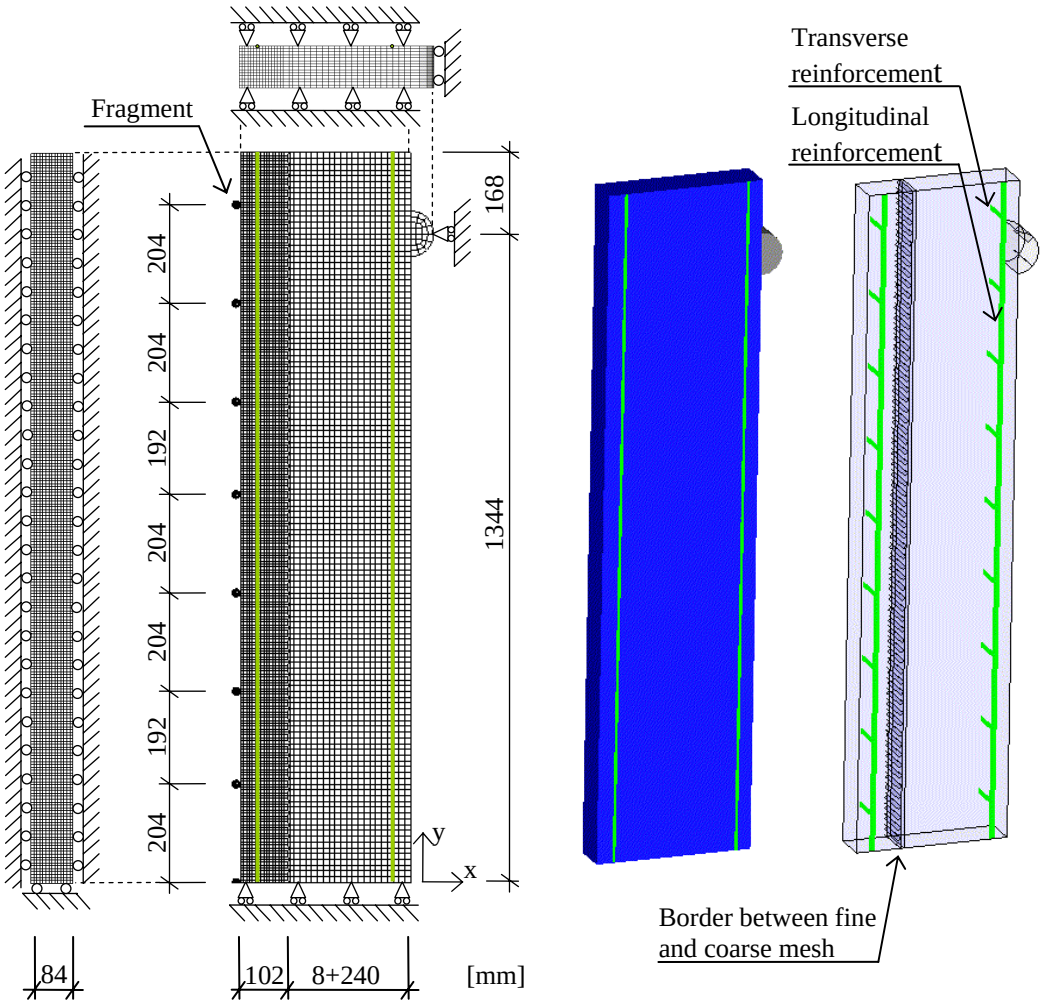

Figure 7.14 Numerical mesh of wall strip used in simulations, also showing reinforcement in the modelled wall strip.

The RHT material model for concrete, included in the standard material library in AUTODYN, was used with some modifications. The preliminary study made it necessary to use the principal-stress tensile-failure model (with crack softening) instead of the hydrodynamic tensile-failure model; see Section 7.2.3. As also discussed in Section 7.2.3, the simulations of blast and fragment loading also placed different demands on the flow rule used in the material model, but an associated flow rule was assumed to be the best choice for simulations of combined loading.

Since the longitudinal reinforcement bars lie in the plane of symmetry (see Figure 7.14), the diameter had to be adapted to this by halving their area. The bars are modelled with a piecewise linear Johnson-Cook material model, beam elements and full interaction with the surrounding concrete; see Section 7.2.1.

The blast load was applied to the concrete front face by use of a time-dependent pressure boundary condition equal to the simplified relation shown in Figure 7.3. The size, mass and distribution of the fragments are also defined in Section 7.1.3. The fragments were modelled in the same way as in the preliminary study, with two elements across the radius and the von Mises (linear-elastic – ideal-plastic) material

model. In the case of combined loading the blast-wave front and the fragments were assumed to arrive at the same time.

7.4.1 Results

Only a brief description of the results from the numerical simulations is presented here; for more detailed information and further reasoning of the results the reader is referred to Paper II.

In Figure 7.15 the response of the wall strip when subjected to the blast load at the time of maximum mid-point deflection is shown. The cracks closest to the supports appear within less than 1 ms after the arrival at the wall and are probably direct shear cracks. After another millisecond, flexural cracks have formed in the middle of the beam, and the damage is localised to a relatively low number of cracks. The maximum mid-point deflection is 65.2 mm and takes place at 29.3 ms after arrival of the blast load.

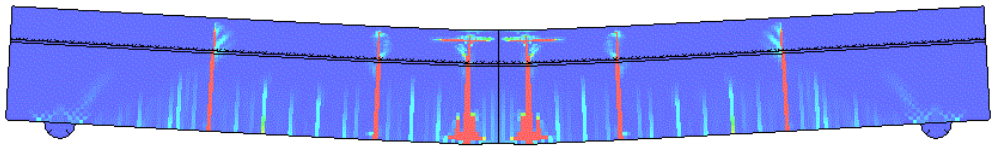

Middle of wall strip

Figure 7.15 Response of wall strip subjected to blast load at time of maximum mid-point deflection.

The damage caused by the fragment impacts in the simulations is more complex than in the case of blast loading, as seen in Figure 7.16, where the wall strip is shown when maximum mid-point deflection is reached. The total damage consists of local damage on the front face, scabbing cracks at the rear of the wall strip, direct shear cracks close to the supports, and bending cracks propagating from the rear of the target towards the front. Since the scabbing cracks did not occur in the simulations of fragment impact made within the preliminary study (see Section 8.2.2.), they were not expected. However, these 2D simulations did not take the effect of multiple, simultaneous impact of fragments into account, and a 2D simulation, taking this effect into consideration by use of boundary conditions, was conducted; this is further discussed in Section 7.4.3. As seen in Figure 7.16 and Figure 7.15 more flexural cracks form in the case of fragment loading than in blast loading (Figure 7.15), which may lead to a more ductile behaviour as the reinforcement bars can strain at more locations. The maximum mid-point deflection, in the case of fragment loading, is 11.0 mm and occurs after 13.3 ms.

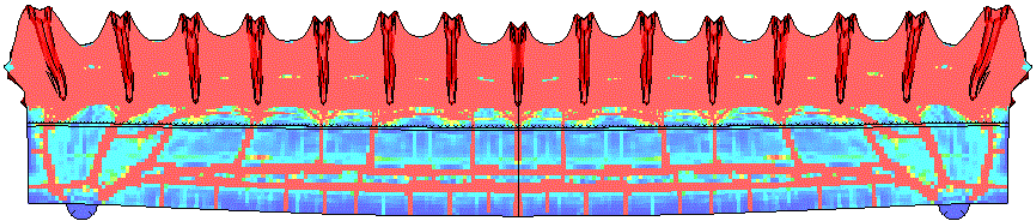

Middle of wall strip

Figure 7.16 Response of wall strip subjected to fragment impacts at time of maximum mid-point deflection.

For combined loading, where the blast wave and the fragments arrive at the wall at the same time, the crack pattern is very similar to that resulting from fragment loading alone, seen when comparing Figure 7.17, where the response in the case of combined loading is shown at time of maximum mid-point deflection, and Figure 7.16. This is due to the early formation of craters at the front face and the appearance of scabbing cracks caused by the fragment impacts. It can also be seen that the diameters of the craters on the front face are smaller for combined loading than for fragment loading alone. The reduced damage on the front side may lead to increased load-bearing capability, compared to the case of fragment loading alone. The maximum mid-point deflection is 85.7 mm and occurs after 33.4 ms.

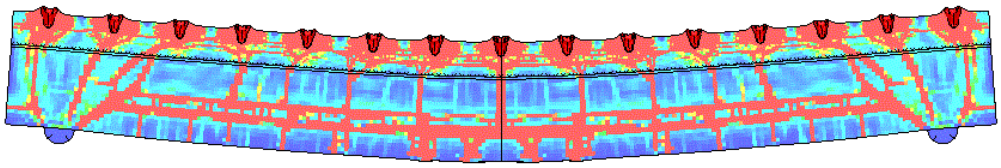

Middle of wall strip

Figure 7.17 Response of wall strip subjected to combined blast and fragment loading at time of maximum mid-point deflection.

7.4.2 Comparison with SDOF results

In Figure 7.18 the mid-point deflection, as a function of the time, is shown for the blast load simulation together with the estimation made with the SDOF method; see Section 7.3. As seen in the results from the numerical simulation and SDOF analysis, the agreement between these two is good.

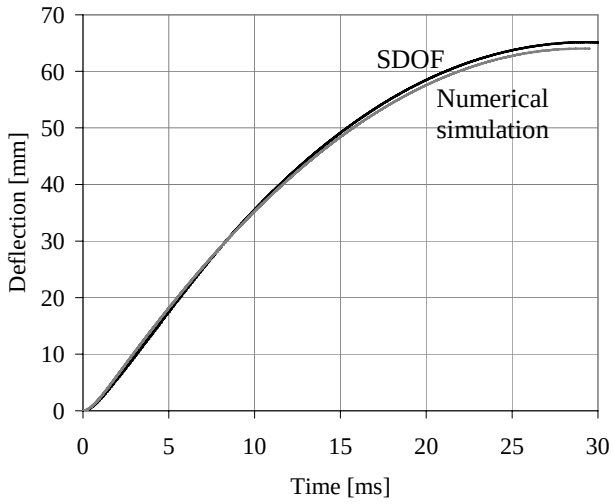

Figure 7.18 Response of wall strip subjected to blast load, estimated with SDOF method and numerical simulation.

In Figure 7.19a the mid-point deflection, as a function of the time, is shown for the fragment impact simulation together with the estimation made with the SDOF method for this case. The maximum mid-point deflection estimated with the SDOF method in the case of fragment loading was 13.9 mm, which is approximately 3 mm more than the maximum mid-point deflection estimated in the numerical simulation. This can be considered a relatively large difference, since it constitutes more than one fourth of the deflection in the numerical simulation. There may be several explanations for this difference. One of them may be that the simplifications in the SDOF analysis are too rough to give accurate results. For example, the energy consumed during penetration of the fragments and the subsequent crushing of the concrete, the probably reduced bearing capacity of the wall strip due to this front-face damage, and the formation of many flexural cracks, allowing an increase of energy-absorbing capacity compared to the case of few flexural cracks, are not represented in the SDOF analysis. However, when comparing the mid-point velocities estimated in the SDOF and numerical analyses, see Figure 7.19b, it can be seen that these correspond well after approximately 6.5 ms, but also that the difference is considerable for shorter times. This is also a probable reason for the differing mid-point deflections shown in Figure 7.19a.

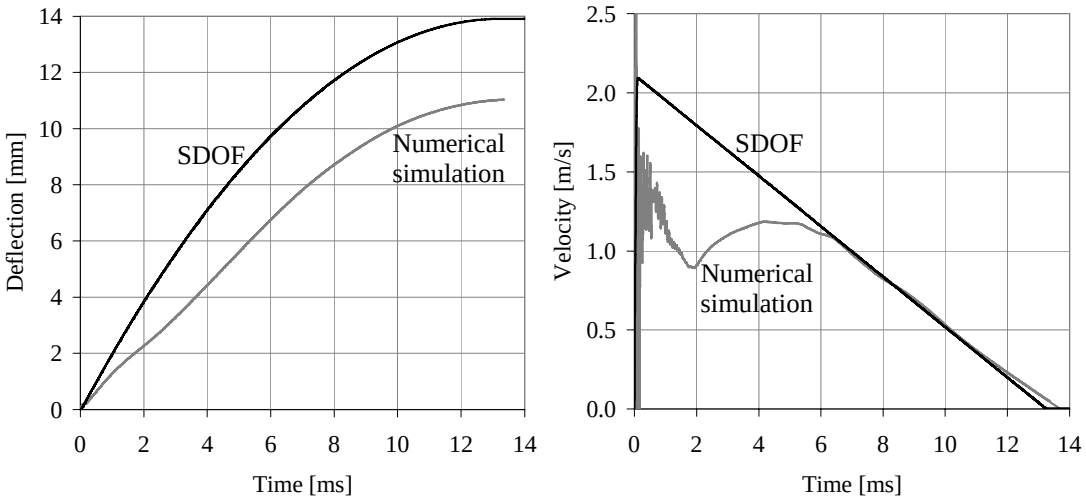

a) *b)*

Figure 7.19 Response of wall strip subjected to fragment impacts, estimated with SDOF method and numerical simulation: (a) mid-point deflection and (b) velocity of mid-point.

In the case of combined, simultaneous loading the results from the numerical simulation and the SDOF analysis differ considerably; the maximum mid-point deflections were estimated to be 85.7 and 139 mm, respectively. Figure 7.20 shows the wall strip's mid-point velocity, estimated with numerical simulation and the SDOF method. In contradiction to the case of fragment loading alone, the velocity differs for all times and not only in the beginning of the simulation.

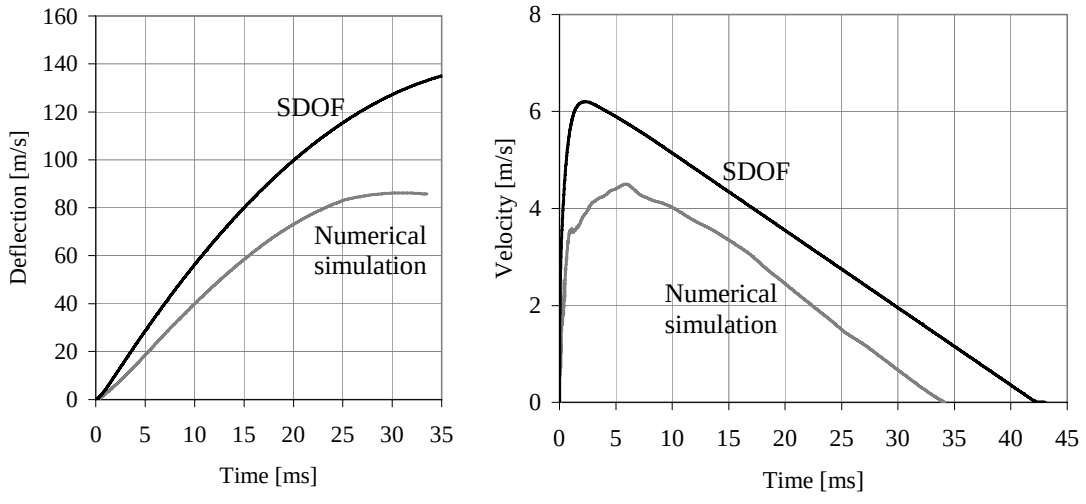

a) *b)*

Figure 7.20 Response of wall strip subjected to combined loading, estimated with SDOF method and numerical simulation: (a) mid-point deflection and (b) velocity of mid-point.

7.4.3 Study of scabbing crack

Since the scabbing cracks appearing in the wall strip when subjected to fragment impacts were not expected, additional 2D simulations were conducted to further study this behaviour. In the additional simulations presented in this section, the effect of multiple, simultaneous impact of fragments was taken into account by use of boundary conditions, as shown in Figure 7.21a.

The result of this simulation is shown in Figure 7.21b, where it can be seen that the scabbing crack occurs. Another possible explanation that had to be studied was the influence of the strain-rate dependence of the tensile strength, which was not taken into account in this study. A similar simulation as just described, but with the standard RHT material model (including the strain-rate effect), was conducted. In the results, shown in Figure 7.21c, it can be seen that scabbing still occurs, and therefore the scabbing could not be explained by the lack of strain-rate dependence of the tensile strength.

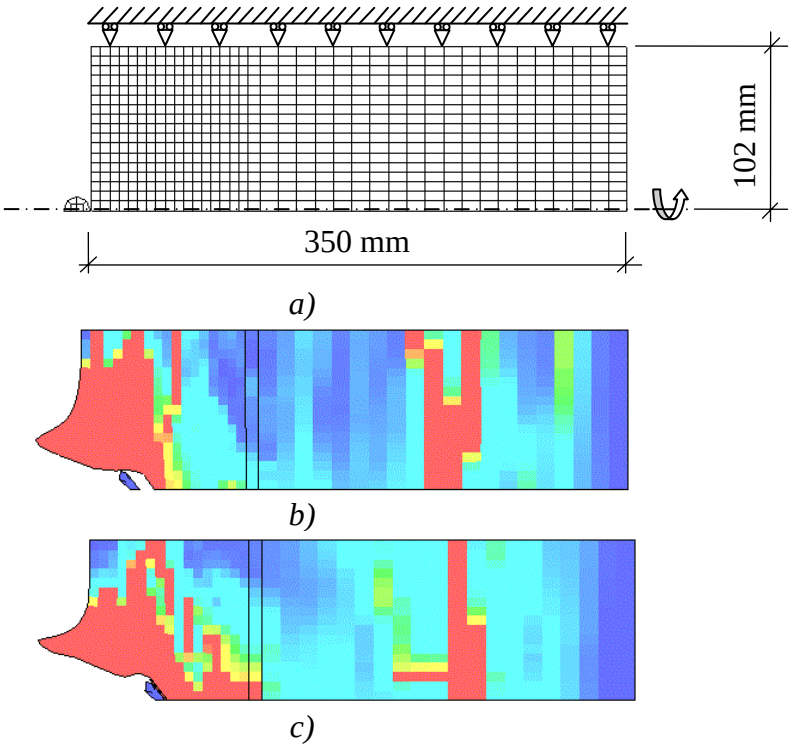

Figure 7.21 *(a) The numerical mesh of AUTODYN 2D simulations of effect of multiple fragment impacts. Numerical results with (b) the same material model as in main study and (c) the standard RHT material model. The black lines crossing the bodies indicate the border between the fine and coarse mesh.*

The average distance to the scabbing cracks in the wall strip, measured from the front face of the wall strip, is 265 mm, below the distance to the tensile-reinforcement layer, meaning that the scabbing cracks appear in between the two reinforcement layers. In experiments the scabbing often occurs at the level of rear face reinforcement. A possible explanation for the discrepancy in scabbing crack location

between experiments and the simulations is that the reinforcement bars are modelled as beam elements, thereby not taking into account the reduced area of concrete over which the stresses can be transferred. If the reduction of concrete area is taken into account, the stresses will become approximately 13% higher than without reduction. This effect could be taken into account by modelling the concrete elements at the reinforcement level with reduced strength. However, as seen in Figure 7.22, weakening of the concrete elements at the level of reinforcement by reducing the strength by 10% does not mean that the scabbing crack appears in these elements. In reality the reinforcement is a natural place for notches, which is also not represented in the simulations since the interface between the reinforcement and the concrete is not modelled to take these effects into account. The location of the scabbing cracks, appearing in the wall strip simulations, may therefore rather represent the case where no tensile reinforcement is used. It should also be pointed out that the two scabbing cracks probably represent one crack in reality, and that scabbing is prevented from occurring by the tensile reinforcement that crosses the scabbing cracks and continues over the support.

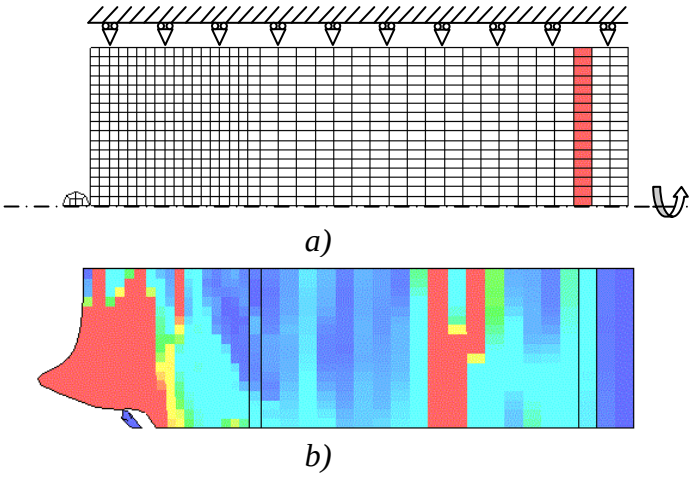

Figure 7.22 *(a) The numerical mesh of AUTODYN 2D simulations of effect of weakened elements (indicated in red) at level of tensile-reinforcement layer and (b) the numerical result.*

8 Conclusions

8.1 General conclusions

The area of blast and fragment loading on reinforced concrete structures involves phenomena not yet well understood. In order to increase the knowledge in this area, three numerical studies were conducted. The studies involved investigations of the effect of reinforcement on the projectile impact, the relative effect of the impact resistance when adding steel fibres to concrete, and the combined effects of blast and fragment loading. The general conclusions from these studies and the theory behind them are presented here.

Numerical simulation with a hydrocode is a useful tool for estimation of damage caused by blast and fragment impacts. This is mainly due to the low costs, ease of carrying out parameter studies, and the possibility to better follow and understand the principal phenomenon involved, compared to experimental testing. However, since the material models used in the simulation, and their ability to describe the real behaviour, are crucial for the simulation results, their limitations must be known by the user and taken into account when analysing and drawing conclusions.

The reinforcement in a concrete structure is necessary in order to ensure ductile behaviour and thereby an energy-absorbing capacity, but may also increase the resistance against local damage. However, an increased projectile resistance, i.e. decreased depth of penetration, can only be achieved with, for this case, suitable reinforcement detailing, since the reinforcement must be located in the damage zone in order to have an effect. Furthermore, the distance between the projectile path and the reinforcement bars is a crucial factor since the confinement effect of the reinforcement, pointed out as a plausible explanation for the increased projectile resistance, decreases with increasing distance. Reinforcement bars do, though, almost always reduce the scabbing and spalling effects.

Addition of moderate dosages of steel fibres in the concrete does not significantly influence the depth of penetration of a striking projectile, while the size of both the spalling and possible scabbing crater decreases. An increased amount of fibres only lead to a small reduction of the spalling crater, whereas the effect on the scabbing crater is more significant – it decreases and may even be prevented.

Due to the complex nature of the effects of combined blast and fragment loading on a reinforced concrete structure, the phenomenon involved is not well understood. Thus, design manuals, used for protective design, often disregard the well-known synergy effect observed for combined loading, or treat it in a very simplified manner. Most damage caused by the multi-fragment impact on a wall element occurs within fractions of a millisecond and consists of local damage on the front face, i.e. craters, scabbing cracks at the rear and direct shear cracks close to the supports. In the case of blast loading the number of flexural cracks, to which elongation of the reinforcement is localised, is relatively low, while for fragment loading the flexural cracks are more numerous. The early appearance of damage caused by the fragments and the larger number of flexural cracks indicate that the load-bearing capacity and mid-point deflection of the element in the case of combined, simultaneous loading are highly influenced by the fragment impact. The impulse intensity of the fragments constituted

approximately 40% of the impulse density of the blast load and the mid-point deflection of the blast load was almost 6 times larger than that caused by the fragment impacts. For combined loading, a synergy effect was observed; the sum of the mid-point deflections for blast and fragment loading treated separately is smaller than the mid-point deflection for combined loading.

8.2 Further research

The response of a reinforced concrete structure subjected to combined blast and fragment loading is highly influenced by different parameters, e.g. blast and fragment load characteristics. Further research within this area must therefore be conducted before the phenomena involved and their parameter dependence can be considered as well understood and generic methods for estimating the structural response can be derived.

As mentioned earlier, numerical simulations are an effective tool to study the response of reinforced concrete structures subjected to blast and fragment impact. However, the material models for concrete, used to describe the concrete behaviour in the hydrocodes, involve various simplifications and limitations. It is of interest to further study how these idealisations and limitations affect the numerical results. It may also be of interest to develop improved material models and simulation procedures in order to increase the accuracy of the numerical results and thereby be able to better understand and predict the complex phenomena involved in severe dynamic loading of reinforced concrete structures.

9 References

ACI 544 (1996): *State-of-the-Art Report on fibre Reinforced Concrete*. ACI Committee 544 Report 544.1R-96, American Concrete Institute, Detroit, 66 pp.

ACI MCP (2002): *Manual of Concrete Practice*. ACI Concrete Institute, Farmington Hills, MI, USA.

Almansa, E.M. and Cánovas, M.F. (1999): Behaviour of normal concrete and steel fibre-reinforced concrete under impact of small projectiles. *Cement and Concrete Composites*, Vol. 29, pp. 1807-1814.

ASCE (1999): *Structural Design for Physical Security – State of the Practice*. Task committee: Conrath, E.J. *et al*., American Society of Civil Engineers, 264 pp.

AUTODYN (2005). *AUTODYN Theory Manual, Revision 4.3*. Century Dynamics Inc.Concord, CA, USA, 227 pp.

AUTODYN (2007). *ANSYS AUTODYN User Manual, Version 11.0*. Century Dynamics Inc., Concord, CA, USA, 528 pp.

Bailey, C.G. (2004): Membrane action of slab/beam composite floor systems in fire. *Engineering Structures*, Vol. 26, No. 12, pp. 1691-1703.

Baker W.E. (1973): *Explosions in Air*. University of Texas Press, Austin, TX, USA, 285 pp.

Bangash, M.Y.H. (1989): *Concrete and Concrete Structures: Numerical Modelling and Applications*. Elsevier applied science, London, 652 pp.

Bažant, Z.P., Xiang, Y.Y., Adely, M.D., Prat, P.C. and Akers, S.A. (1996): Microplane Model for Concrete: II: Data Localization and Verification. *Journal of Engineering Mechanics*, Vol. 122, No. 3, pp. 255-262.

Brara, A. and Klepaczko, J.R. (2007): Fracture energy of concrete at high loading rates in tension. *International Journal of Impact Engineering*, Vol. 34, No. 3, pp. 424-435.

Bischoff P.H. and Perry, S.H. (1991): Compressive behaviour of concrete at high strain rates. *Materials and Structures*, Vol. 24, pp. 425-450.

Boverket (2004): *Boverkets Handbook för Betongkonstruktioner BBK 04*, (Boverkets Handbook for Concrete Structures, BBK 04, in Swedish), Boverket, Karlskrona, Sweden, 271 pp.

Brode, H.L. (1955): Numerical Solutions of Spherical Blast Waves. *Journal of Applied Physics*, Vol. 26, No. 6, pp. 766-775.

Cánovas, M.F., Pamies, R.G., Simón del Porto, J.R. and Almansa, E.M. (1994): Impacts effects on the primary fragmentation generated by the HE81 mortar grenade on conventional concrete and steel fibres reinforced concrete. *Proceedings*

of the Third International Conference on Structures Under Shock and Impact, Madrid, Spain, Computational Mechanics Publications, 1994. pp. 37-44.

CEB FIP (1999): *Structural Concrete – Textbook on Behaviour, Design and Performance, Updated knowledge of the CEB/FIP Model Code 1990, Volume 1*. International Federation for Structural Concrete, Lausanne, Switzerland, 224 pp.

ConWep (1992): *ConWep*. Collection of conventional weapon effects calculations based on TM 5-855-1, Fundamentals of Protective Design for Conventional Weapons, U. S. Army Engineer Waterboys Experiment Station, Vicksburg, VA, USA.

Curran, D.R. (1997): Simple fragment size and shape distribution formulae for explosively fragmenting munitions. *International Journal of Impact Engineering*, Vol. 20, 1997, pp. 197-208.

Ekengren, B. (2006): *Skyddsrum SR0*6 (Shelter Regulations SR06, in Swedish). Swedish Rescue Services Board, Karlstad, Sweden, 113 pp.

Ekengren, B. (1994): *Shelter Regulations SR-English Edition*. Swedish Rescue Services Agency, Karlstad, Sweden, 94 pp.

Erkander, Å. and Pettersson, L. (1985): *Betong som splitterskydd: Skjutförsök på plattor av olika betongmaterial* (Concrete as protective material against fragment impacts: Fragment impacts on plates of different types of concrete, in Swedish). Försvarets Forskningsanstalt, C 20574-D6(D4), Stockholm, Sweden, 66 pp.

Forsén, R. and Nordström, M. (1992): *Damage to Reinforced Concrete Slabs Due to the Combination of Blast and Fragment Loading* (In Swedish). National Defence Research Establishment (FOA), FOA Report B 20101-2.6, Tumba, Sweden, 12 pp.

Forsén, R. and Sten, G. (1994): *Utredning om splitterverkan/splitterskydd, Jämförelse mellan två 250 kg minbomber* (In Swedish). National Defence Research Establishment (FOA), Tumba, Sweden, 25 pp.

Girhammar, U.A, (1990): *Brief Review of Combined Blast and Fragment Loading Effects*. Report C7:90. National Fortifications Administration, Eskilstuna, Sweden, 15 pp.

Gebbeken, N., Greulich, S. and Pietzsch, A. (2006): Hugoniot properties for concrete determined by full-scale detonation experiments and flyer-plate-impact tests. *International Journal of Impact Engineering*, Vol. 32, pp. 2017-2031.

Gylltoft, K. (1983): *Fracture Mechanics Models for Fatigue in Concrete Structures*. Doctoral Thesis. Division of Structural Engineering, Luleå University of Technology, Luleå, Sweden, No. 1983:25:D, 210 pp.

Hansson, H. (1998): *Numerical Simulations of Concrete Penetration*. FOA Report 98-00816--311--SE. National Defence Research Establishment, Tumba Sweden, 17 pp.

Jirásek, M. (2006); *Modelling of Localized Inelastic Deformation*. Lecture notes. Czech Technical University, Prague, 239 pp.

Johansson, M. (1995): S*tructural Behaviour in Concrete Frame Corners of Civil Defence Shelters, Non-linear Finite Element Analyses and Experiments.* Doctoral Thesis. Department of Structural Engineering, Division of Concrete Structures, Chalmers University of Technology, Publication no. 00:2, Göteborg, Sweden, 204 pp.

Johansson, M. and Laine, L. (2007): *Bebyggelsens motståndsförmåga mot extreme dynamisk belastning, Delrapport1: Last av luftstötvåg* (The capacity of buildings to resist severe dynamic loading, Part 1: Blast wave loading, in Swedish). Swedish Rescue Services Agency, Karlstad, Sweden, 114 pp.

Krauthammer, T. (2000): *Modern Protective Structures, Design, analysis and evaluation*. Course notes. The Pennsylvania State University, 358 pp.

Krauthammer, T. (2006): *Modern Protective Structures, Design, analysis and evaluation*. Course notes. The Pennsylvania State University, 412 pp.

Leppänen, J. (2004): *Concrete Structures Subjected to Fragment Impacts – Dynamic Behaviour and Material Modelling.* Doctoral Thesis. Department of Structural Engineering and Mechanics, Division of Concrete Structures, Chalmers University of Technology, Publication no. 04:4, Göteborg, Sweden, 127 pp.

Leppänen, J. (2002): *Dynamic Behaviour of Concrete Structures Subjected to Blast and Fragment Impacts.* Licentiate Thesis. Department of Structural Engineering, Division of Concrete Structures, Chalmers University of Technology, Publication no. 02:4, Göteborg, Sweden, 78 pp.

Leppänen, J. (2003): *Splitterbelastad betong – Experiment och numeriska analyser* (Fragment Impacts into Concrete – Experiments and Numerical Analyses, in Swedish). Department of Structural Engineering and Mechanics, Division of Concrete Structures, Chalmers University of Technology, Report no. 03:6, Göteborg, Sweden, 80 pp.

Li, Q.M., Reid, S.R, Wen, H.M. and Telford, A.R. (2005): Local impact effects of hard missiles on concrete targets. *International Journal of Impact Engineering*, Vol. 32, 2005, pp. 224-284.

Luo, X., Sun, W. and Chan, S.Y.N. (2000): Characteristics of high-performance steel fibre-reinforced concrete subjected to high velocity impact. *Cement and Concrete Research*, Vol. 30, pp. 907-914.

Löfgren, I. (2005): *Fibre-reinforced Concrete for Industrial Construction – a fracture mechanics approach to material testing and structural analysis.* Doctoral Thesis. Department of Civil and Environmental Engineering, Division of Structural Engineering, Chalmers University of Technology, Göteborg, Sweden, 243 pp.

Magnusson, J. and Hallgren, M. (2000): *High Performance Concrete Beams Subjected to Shock Waves from Air Blast*. National Defence Research Establishment (FOA), FOA Report 00-01586-311--SE, Tumba, Sweden. 86 pp.

Magnusson, J. and Hansson, H. (2005): *Simuleringar av explosionsbelastade betongbalkar – en principstudie*, (Numerical simulations of concrete beams- a principal study, in Swedish). National Defence Research Establishment (FOI), FOI Report 1686--SE, Tumba, Sweden. 55 pp.

Malvar, L.J. and Ross, C.A. (1998): Review of Strain Rate Effects for Concrete in Tension. *ACI Materials Journal*, Vol. 95, No. 6, pp. 735-739.

Nataraja, M.C., Nagaraj, T.S. and Basavaraja, S.B. (2005): Reproportioning of steel fibre reinforced concrete mixes and their impact resistance. *Cement and Concrete Research*, Vol. 35, No. 12, pp. 2350-2359.

Nyström, U. (2006): *Design with regard to explosions*. Master's Thesis. Department of Civil and Environmental Engineering, Division of Structural engineering, Chalmers University of Technology, Göteborg, Sweden, 205 pp.

PCA (2002): *Design and Control of concrete Mixtures*. Portland Cement Association. 372 pp.

Plos, M. (1995): *Application of Fracture Mechanics to Concrete Bridges. Finite Element Analysis and Experiments*. Doctoral Thesis. Department of Structural Engineering, Division of Concrete Structures, Chalmers University of Technology, Publication no. 95:3, Göteborg, Sweden, 127 pp.

Riedel, W. (2000): *Beton unter dynamischen Lasten, Meso- und makromechanishe Modelle und ihre Parameter* (Concrete under dynamic loads, Meso- and macromechanical models and their parameters, in German). Doctoral Thesis. Fakultät für Bauingenieur- und Vermessungswesen, der Universität der Bundeswehr, Munich, Germany, 210 pp.

Schuler, H. (2004): *Experimentelle und numerische Untersuchungen zur Schädigung von stroßbeanspruchtem Beton* (Experimental and numerical investigations of damage in impact stressed concrete, in German). Doctoral Thesis. Fakultät für Bauingenieur- und Vermessungswesen, der Universität der Bundeswehr, Munich, Germany, 184 pp.

U.S. Army (1990): *Design of Structures to Resist the Accidental Effects of Explosions*. Department of the Army Technical Manual TM 5-1300, Navy Publication NAVFAC P-397, Air Force Report 88-22, Washington D.C., USA. 1784 pp.

U.S. Army (1992): *Fundamentals of Protective Design for Conventional Weapons*. Technical Manual TM 5-855-1. 271 pp.

van Mier, J.G.M. (1984): *Strain-softening of concrete under multiaxial loading conditions*. Doctoral Thesis. Technische hogeschool Eindhoven, The Netherlands, 348 pp.

von Essen, W. (1973): *Provisoriska anvisningar för dimensionering av armerade betongkonstruktioner som skydd mot verkan av konventionella vapen inom närmissområde, Kommentarer* (In Swedish). Fortifikationsförvaltningen Publ. 25:2, 34 pp.

Weerheijm, J. and van Doormal, J.C.A.M. (2007): Tensile failure of concrete at high loading rates: New test data on strength and fracture energy from instrumented spalling tests. *International Journal of Impact Engineering*, Vol. 34, No. 3, pp. 609-626.

Zollo, R.F. (1997): Fibre-reinforced concrete: an Overview after 30 Years of Development. *Cement and Concrete Composites*, Vol. 19, No. 2, pp. 107-122.

Zukas, J.A. and Scheffler, D.R. (2000): Practical aspects of numerical simulations of dynamic events: Effects of meshing. *International Journal of Impact Engineering*, Vol. 24, No. 9, pp. 925-945.

Appendix A Empirical Equations

This appendix is directly taken from Leppänen (2004). The references are found in the reference list (Chapter 9), but are also according to Leppänen (2004).

Depth of penetration

By using a direct formula, from ConWep (1992), the depth of penetration, x (in inches), can be estimated for fragments penetrating massive concrete:

$$x = \frac{0.95 m_f^{0.37} V_s^{0.9}}{f_c^{0.25}} \qquad \text{for } x \le 1.4 m_f^{1/3}$$

or

$$x = \frac{0.464 m_f^{0.4} V_s^{1.8}}{f_c^{0.5}} + 0.487 m_f^{1/3} \qquad \text{for } x > 1.4 m_f^{1/3}$$

where m_f is fragment weight [oz.], V_s is the fragment striking velocity [kfps] and f_c is the concrete compressive strength [ksi]. By using conversion factors, as shown in Table A.1, the penetration depth of fragments can be calculated in SI units.

The depth of penetration, x, according to von Essen (1973) can be estimated with following equation:

$$x = 180 \cdot 10^{-6} \cdot v_r \cdot \sqrt[3]{m_f} \qquad \text{[m]} \qquad \text{(A.1)}$$

where v_r is the fragment velocity and m_f is the fragment mass [kg].

The depth of penetration, x, for a spherical fragment of 35.9 g (i.e. 20.6 mm in diameter), according to Erkander and Pettersson (1985) can be estimated as:

$$x = 288 \cdot 10^{-6} \cdot \sqrt[3]{m_f} \cdot (v_r - 170) \qquad \text{[m]} \qquad \text{(A.2)}$$

where v_r is the fragment velocity and m_f is the fragment mass [kg].

Thickness to prevent perforation

The thickness of a concrete wall that just prevents perforation, d_{pf}, can be estimated with the following equation, from Krauthammer (2000):

$$d_{pf} = 1.09 x m_f^{0.033} + 0.91 m_f^{0.33} \qquad \text{[in]} \qquad \text{(A.3)}$$

where x is the depth of penetration from Eqs.(A.1) and (A.2), and m_f is the fragment weight in ounce [oz]. To convert to SI units, see Table A.1.

Table A.1 Conversion factors: Inches-pounds to SI units (metric), according to the ACI MCP (2002).

To convert from	to	multiply by
inches	millimetres [mm]	25.4
feet	metres [m]	0.3048
kip-force/square inch [ksi]	megapascal [MPa]	6.895
ounces [oz]	grams [g]	28.34

Appendix B Steel-fibre Volume Fraction

This appendix shows how the steel-fibre volume fraction corresponding to a fibre-reinforced concrete, with specified fracture energy, was estimated in the study presented in Chapter 6 and Paper I. The material properties of three fibre-reinforced concretes were used in the numerical study of how the addition of steel fibres in concrete affects the projectile resistance.

A bi-linear crack softening behaviour, according to Figure 2.8, was assumed for the fibre-reinforced concretes. Equation 2.1 and 2.2, describing the relation between the number of fibres per m^2, n_{fibres}, the volume fraction of fibres, V_f, and the b_2-parameter, were used as follows.

The parameter a_1 was assumed to be equal to the slope of the first branch in the bi-linear relation used to describe the softening behaviour of the normal concrete used in the study. The bi-linear relation proposed by Gylltoft (1983), see Figure 2.3, was used for the normal concrete, where the slope of the first branch can be calculated as the tensile strength, f_t, divided by the fracture energy for the normal concrete, $G_{F.NSC}$.

$$a_1 = \frac{f_t}{G_{F.NSC}} \tag{B.1}$$

According to Löfgren (2005) the parameter a_2 is mainly related to the fibre length, and the bond between the fibre and the concrete also influences its value. Since these factors are not known in the study, the typical values presented in Löfgren (2005) for the a_2-parameter were used to estimate a realistic value. The typical values are given as $0.025\ mm^{-1} \leq a_2 \leq 0.25\ mm^{-1}$ and a value close to the average value of these was desired. It turned out that the a_2-parameter could be estimated as:

$$a_2 = \frac{a_1}{200} \tag{B.2}$$

By means of the a_1- and a_2-parameters, the fracture energy and the tensile strength, the parameter b_2 can be calculated, and Equation 2.2 can be used to determine the corresponding number of fibres per m^2. However, in the experiments where this expression was derived, the b_2-parameter for the plain concrete was determined as 0.257, as seen in Figure B.1.

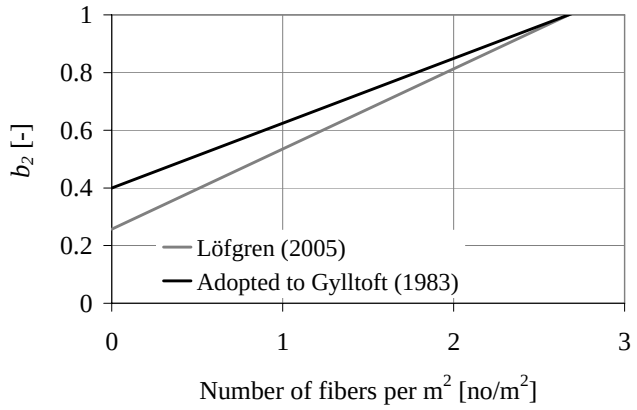

Figure B.1 Response of wall strip subjected to combined blast and fragment

This value differs from the value 0.4 used in Gylltoft (1983), implying that the equation had to be adjusted. It was assumed that the volume fraction giving a b_2-parameter equal to 1.0 was the same in the two cases, and the relation between the b_2-parameter and the number of fibres per m^2, n_{fibres}, was scaled according to this.

$$b_2 = \frac{1-0.4}{2.6727} n_{fibres} + 0.4 \tag{B.3}$$

Equation (2.2) was then used to calculate the corresponding volume fraction of fibres, V_f.

$$V_f = \frac{n_{fibres}}{2.5396} \tag{B.4}$$

Appendix C Design Fragment Weight

In this appendix it is shown how the design fragment weight was determined in the study of combined blast and fragment loading, presented in Chapter 7 and Paper II. Since the impulse was used to determine the characteristics of the design fragment, the mass distribution and velocity of the fragments had to be determined.

The mass distribution of fragments can be estimated with Equation 3.5, given that the fragment distribution factor, M_A, is known. As mentioned before, the geometry of the bomb referred to in the Swedish Shelter Regulations, Ekengren (2006), is not specified and the fragment distribution factor could not be calculated. Instead the American GP-bomb Mk 82 was used to estimate a value; see Section 7.1.3 and Paper I. The fragment distribution factor was in this way estimated to be 1.758 grams (0.062 oz), and as the weight of casing, W_c, is known the mass distribution was determined; see Figure C.1. The fragments were then divided into fractions of 0.1 grams and the number of fragments in each fraction was calculated.

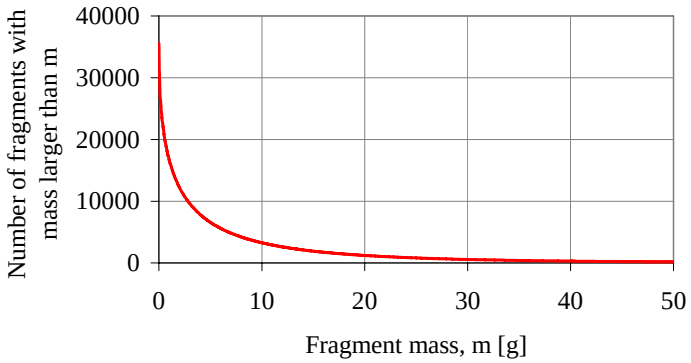

Figure C.1 Mass distribution of 250 kg GP-bomb with 50 weight per cent TNT.

The initial velocity of the fragments was calculated with the Gurney equation (Equation 3.7) and the velocity of the fragments at a stand-off of 5 metres was then calculated with Equation 3.8. As the impulse of each fragment is calculated as the mass of the fragment times its velocity, the total impulse per fraction of fragments could be calculated. The weight of the design fragment was then determined by finding the fragment weight that corresponds to the average impulse per fraction.

In this way the fragment weight was estimated as 21.9 grams, its striking velocity at a stand-off of 5 metres as 1 760 m/s and the diameter as 17.5 mm, giving a total impulse of 3 468 Ns.

Since it was assumed that 60% of the total fragment mass falls in a sector of 40°, as shown in Figure 7.4, and the fragments were assumed to be equal in size and shape, it can be said that 60% of the total number of fragments falls within this sector. Only 2.69% of these fragments strike a metre-wide strip of the wall, and the total weight of the fragments striking the wall strip, which is 3 metres high, is 2.0 kg, giving a mass density of 0.66 kg/m^2.

Paper I

Comparative numerical studies of projectile impacts on plain and reinforced concrete

Nyström, U. and Gylltoft, K.

Submitted to *International Journal of Impact Engineering*, April 2008

Comparative numerical studies of projectile impacts on plain and steel-fibre reinforced concrete

Ulrika Nyström*, Kent Gylltoft

Department of Civil and Environmental Engineering, Structural Engineering, Concrete Structures, Chalmers University of Technology, SE-412 96 Göteborg, Sweden
(*ulrika.nystrom@chalmers.se)

Abstract

The enhanced energy absorption characteristics of fibre-reinforced concrete, compared to plain concrete, motivate its increased usage in protective structures, but how does it influence the projectile resistance of a structure? The numerical hydrocode AUTODYN was used to simulate how steel-fibre volume fractions of about 0.2, 0.5 and 0.75% influence the depth of projectile penetration and crater formation on the front and rear face of a concrete target. The results were compared with numerical results of projectile impacts on plain concrete. Steel fibres added to the concrete mix had a minor influence on the depth of penetration while the crater size on both front and rear faces of the target decreased. The crack propagation beyond the crater on the front face was also reduced when fibres were added to the concrete. An increased amount of fibres in the concrete showed no effect on the crater size on the front face of the target, but led to further decreased size of the crater on the rear face of the concrete cylinder. It is concluded that the scabbing crater can be reduced in size and prevented by usage of steel-fibre reinforced concrete even if the depth of penetration is only slightly less than to penetration depth in plain concrete.

Keywords: Numerical simulation, Projectile impact, Steel-fibre reinforced concrete, Penetration

---

1. Introduction

Researchers have experimentally studied the behaviour of fibre-reinforced concrete under impact loading and observed a significant increase in impact resistance when compared to plain concrete [1-7]. In cases of projectile penetration, the depth of penetration was not significantly influenced while the crater diameters on the front and rear faces of the target were reduced [1,6,7]. However, the structural behaviours of targets subjected to impact are complicated, depending on material factors as well as test condition factors [4].

In order to improve the understanding of how the addition of fibres in concrete may influence responses in a target, numerical studies of projectile penetration in steel-fibre reinforced concrete have been conducted. Using a numerical-simulation tool is motivated by the high cost of undertaking impact tests and the ease of changing material properties. Hence, it is possible to study the influence of different parameters, such as fracture energy, which depends on the volume fraction of added fibres.

The objective of this paper is to study how the addition of steel fibres in concrete influences the depth of penetration and crater formation on the front and rear faces of steel-confined concrete cylinders of different lengths. This is a substudy within a research project whose long-term aim is to study the behaviour of concrete structures subjected to blast and fragment impacts, and the synergy effect of these loads. The research project is a collaboration between Chalmers University of Technology and the Swedish Rescue Services Agency. In earlier studies within the project, the effect of blast waves in reinforced-concrete structures, fragment impacts on plain concrete, design with regard to explosions and reinforced concrete subjected to projectile impact were studied by Johansson [8], Leppänen [9] and Nyström [10,11], respectively.

2. Theoretical framework

A projectile impact may cause local and global damage to a concrete structure. Global damage consists of flexural deformations, which, unlike local damage, may cause structural failure. Local damage may cause spalling and crushing of concrete on the front face and scabbing on the rear face of the target, together with projectile penetration into the target or even full penetration (i.e. perforation) of the target [12,13]. Different variables have been proposed to measure local damage, such as depth of penetration, perforation and scabbing thickness or ballistic limit (i.e. the minimum velocity at which the projectile penetrates the target) in plain or reinforced concrete [13]. These variables are often estimated by using empirical or semi-empirical equations proposed during the last century, especially after the Second World War [14]. Also purely analytical formulas have been proposed [13, 15-17] which can be single-, bi- or multi-stage models built on the theory of cavity expansion, that of shear-plug formation, or a combination of these two.

In general all these empirical, semi-empirical and analytical equations are intended for use within strict limitations of e.g. geometries and material properties of projectile and target, as well as impact conditions [12-19]. Even if these equations have the ability to predict local damage variables with high reliability under conditions similar to those used in developing the equations, they may not be generic enough to predict the variables under slightly different circumstances.

Another way to estimate the damage caused by projectile impact is to use hydrocode simulations. This is growing more common as computing becomes faster, cheaper and more powerful, and as the material models become more reliable. These computer codes are representations of the conservation laws for a continuum using different numerical schemes. Numerical simulations were performed by Tham [17] and Hansson [20], among others, using AUTODYN-2D and AUTODYN-3D [21], to study the perforation of concrete targets by steel projectiles. They concluded that the simulated local damage showed good agreement with experimental data.

2.1 Material properties

2.1.1 Plain concrete

A uni-axial stress-strain relationship, as shown in Fig. 1a, is often used to characterize the static material behaviour of concrete. The ultimate tensile strength, f_t, for normal-strength concrete is less than one tenth of the ultimate compressive strength, f_c, and an increasing value of the compressive strength leads to a decreasing ratio between tensile and compressive strengths; Fig. 1b.

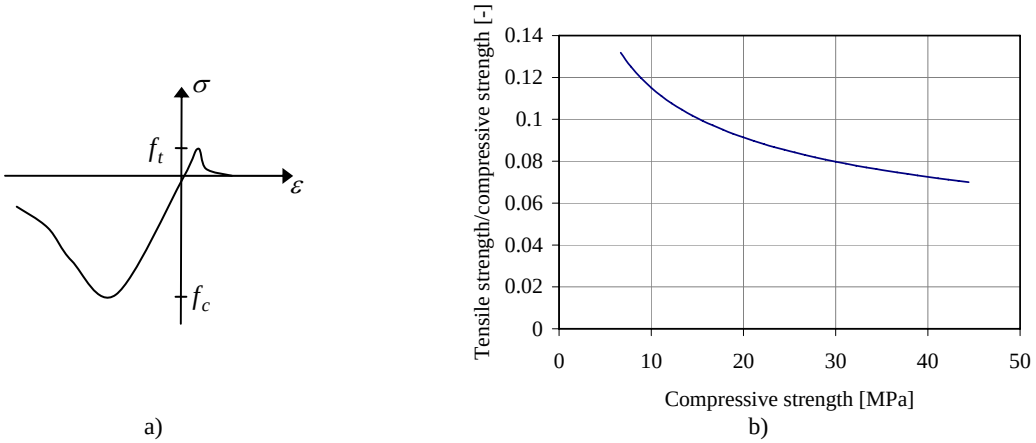

a) b)

Fig. 1. (a) Schematic view of the stress-strain relationship for concrete and (b) the relation between tensile and compressive strengths (uni-axial loading) according to CEB FIP Model Code 1990 [22].

Moreover, after failure initiation in uni-axial tension, stresses can be transferred over the crack. The crack can in a more literal way be described as a process zone consisting of a system of discontinuous micro-cracks. When the propagating micro-cracks have formed a continuous crack, the critical crack opening, w_c, is reached and no more stresses can be transferred over the crack. The softening behaviour is often shown as a relation between the stress and the crack opening, where the area under the curve

represents the fracture energy, G_F. To simplify, the softening branch is often idealised to a bi-linear (e.g. Gylltoft [23]) or power function (e.g. Hordijk-Reinhard expression, [24]) as shown in Fig. 2.

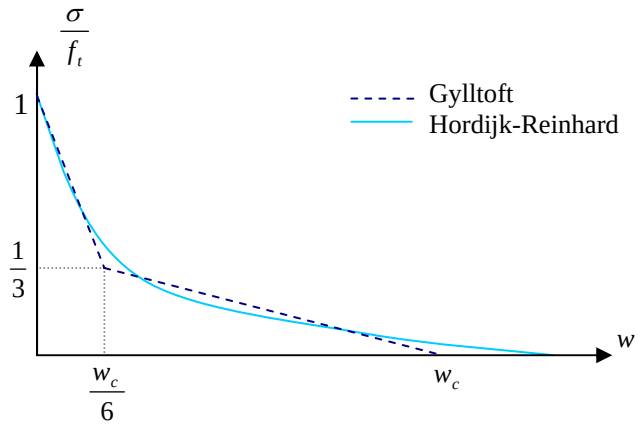

Fig. 2. Bi-linear and power function, respectively, describing the softening after failure initiation in concrete under uni-axial tension.

In building structures the state of stress is multi-axial, and in the case of impact loading, the lateral stresses may be very high. Compressed concrete also subjected to lateral confinement has increased strength and stiffness compared with unconfined concrete. Furthermore, confinement of concrete results in increased ductility.

The porosity of concrete results in non-linear behaviour for hydrostatic pressures. For low pressures, the relation between the hydrostatic pressure, p, and the density, ρ, of concrete is linear, meaning that these pressures only cause elastic deformation in the concrete matrix. If unloading takes place in this phase, the density goes back to the initial density for the concrete, ρ_0. However, further loading results in microcracking at a certain pressure level p_{crush}, and the relation becomes non-linear. When the microcracking starts, the plastic compaction phase is entered, where the concrete is compacted as the pressure continues to increase due to the collapse of pores. When all pores have collapsed and the concrete is fully compacted, the relation between the pressure and density becomes linear again and when unloading to zero pressure the density equals that of fully compacted concrete, ρ_s. This behaviour is described by the equation of state (EOS), shown in Fig. 3.

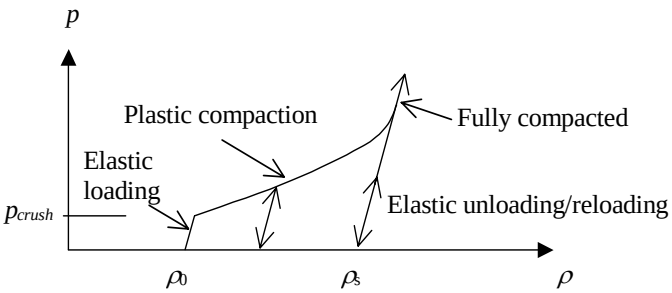

Fig. 3. Equation of state for concrete; from Leppänen [9].

Impact loading, such as fragment and missile impact, causes high strain rates in the target material, and since most materials are somewhat strain-rate-dependent, the strength of the target material will increase compared to the static strength. Concrete is also a strain-rate-sensitive material where a significantly increased strength can be seen for relatively low strain rates. The ultimate uni-axial compressive strength for normal-strength concrete may be more than doubled and, according to Bischoff [25] and Ross et al. [26], the ultimate uni-axial tensile strength can increase by a factor 5 to 7 at very high strain rates.

It has earlier been unclear whether the fracture energy is strain-rate-dependent or not, mostly due to the lack of reliable experimental test procedures for which the fracture energy for high strain rates could be measured. Weerheijm [27] concluded that the fracture energy is strain-rate-independent since experiments showed relatively constant fracture energy up to strain rates of 23 s^{-1}, but more recent studies ([28-30]) indicate that also the fracture energy is strain-rate-dependent. Schuler [28] has proposed a relation

between the dynamic increase factor for the fracture energy for concrete, defined as the ratio between the dynamic fracture energy and the static fracture energy, and the crack-opening velocity, as shown in Fig. 4.

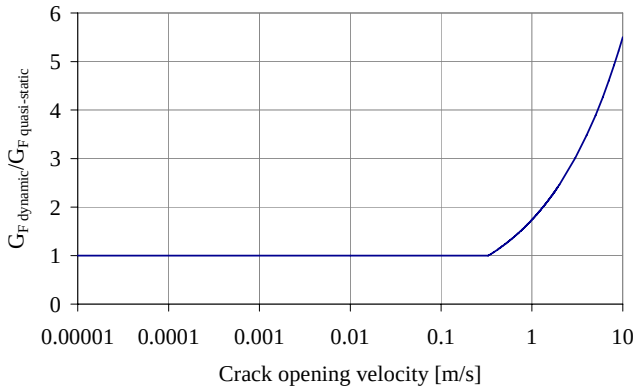

Fig. 4. Relation between dynamic increase factor for fracture energy and crack-opening velocity for concrete, according to Schuler [28].

2.1.2 Steel-fibre reinforced concrete

The primary effect of adding fibres to concrete is that they improve the post-cracking behaviour and the toughness, i.e. the capacity of transferring stresses after matrix cracking, whereas the modulus of elasticity and the tensile and compressive strengths are not significantly affected as long as a moderate dosage (<1%) of fibres is used [31]. However, the effect of fibres is highly dependent on the type of fibre used, the size and properties of the fibres, the volume fraction added and the properties of the concrete matrix.

In plain concrete, the shear capacity is explained as aggregate interlock and friction between the shear planes. When adding low and moderate dosages of fibres to the plain concrete, the cracking strength is not affected, but as soon as the matrix cracks the fibres are activated and start to be pulled out, leading to an increased shear-transfer capacity.

As the relation of the stress-crack opening (σ-w) curve for steel-fibre reinforced concrete is more or less complex, the relation is often simplified in the same manner as for plain concrete. For practical applications it has been found that the bi-linear relation according to Fig. 5 is often a sufficient approximation. By experiments Löfgren [31] has made phenomenological interpretations of the parameters in the bi-linear σ-w relation for steel-fibre reinforced concrete. The decreasing rate of the tensile-stress capacity directly after tensile-failure initiation in the material, parameter a_1, is essentially governed by the fracture properties of plain concrete, but may be slightly reduced compared to this. The slope of the second branch in the σ-w curve, parameter a_2, is principally related to the fibre length. The critical crack opening w_c, for which no more stresses can be transferred by the crack, is in the range of $L_f/10$ to $L_f/2$, where L_f is the length of the fibre, but poor fibre bond or fibre fracture may lead to a reduced critical crack opening. The value of parameter b_2 is primarily related to fibre dosage and increases with an increasing fibre-volume fraction.

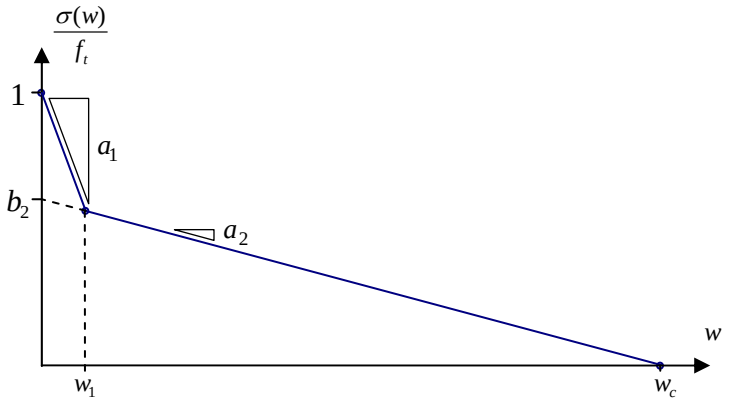

Fig. 5. Bi-linear stress-crack opening relation for steel-fibre reinforced concrete.

3. Study procedure and analyses

An experiment performed at the Swedish Defence Research Agency (FOI) in 1998, see [20], was used to validate the numerical model of projectile impact on plain concrete. In the comparative study presented in this paper, where the effect of added steel fibres in the concrete was limited to an improved post-cracking behaviour, the numerical model for fibre-reinforced concrete was not validated against measured damage variables from a specific experiment. The numerical results from simulations with fibre-reinforced concrete, which are assumed to give the overall behaviour of projectile impact on fibre-reinforced concrete compared to plain concrete, were compared to conclusions drawn from experiments described in [1-7]. The procedure is schematically illustrated in Fig. 6.

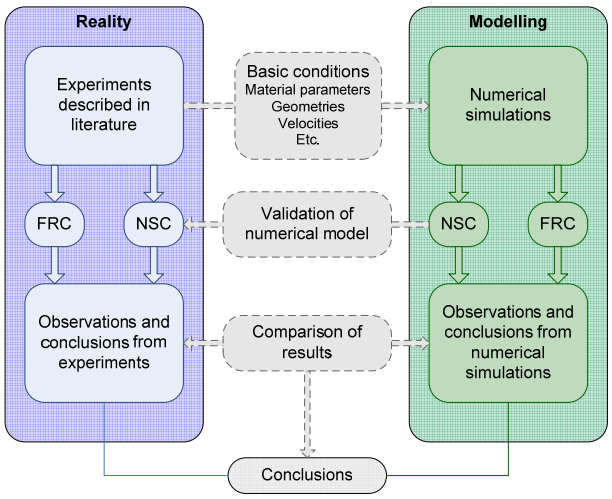

Fig. 6. Schematic illustration of study procedure, where *NSC* is *N*ormal-*S*trength *C*oncrete and *FRC* is *F*ibre-*R*einforced *C*oncrete.

3.1 Benchmark experiment

In the experiment reported by Hansson [20], two shots of 6.25 kg ogive-nosed steel projectiles were fired into a 2.0 m long and 1.6 m wide concrete cylinder cast in a steel culvert. The same striking velocity of 485 m/s was achieved in the two shots. In the first shot, where a support was used at the rear face of the target, the depth of penetration was 655 mm. The second shot, without support on the rear face, resulted in 660 mm penetration of the projectile. Hence, the support at the rear face of the target had a negligible effect on the depth of the penetration of the projectile. The diameter of the front-face crater was approximately 800 mm in both shots. The projectile had a length of 225 mm, a diameter of 75 mm, a density of 7 830 kg/m^3, a bulk modulus of 159 GPa, a shear modulus of 81.8 GPa, and a yield stress of 792 MPa. The concrete cube strength was approximately 40 MPa (tested on 150 mm cubes).

3.2 Numerical simulations

3.2.1 Studied bodies

In order to study how the addition of steel fibres to the concrete affects the impact resistance, numerical simulations of projectile impact on plain and steel-fibre reinforced concrete were conducted. Three different fibre-reinforced-concrete mixes (called FRC1, FRC2 and FRC3) were used in the simulations. The length, L, of the cylindrical target was varied, and two different striking velocities of the projectile, v_{proj}, were used in order to study the effect on the scabbing and perforation limit of the target. The simulations of plain concrete (called NSC) were also used to validate the numerical model by comparing the results to the findings from the benchmark experiment described in the previous section. Table 1 sums up the numerical simulations and shows the values of the parameters that vary in between them. The hydrocode AUTODYN-2D [17] was used for all simulations.

Table 1
Numerical simulations.

Ident	*Concrete*	*Tensile failure model* [a]	σ-*w curve*	δ [-] [a]	L [mm]	v_{proj} [m/s]
NSC001	NSC	Hydro	-	0.025	2000	485
NSC002	NSC	Hydro	-	0	2000	485
NSC003	NSC	Principal Stress	Linear	0	2000	485
NSCs001	NSC	Principal Stress	Bi-linear	0	2000	485
NSCs002	NSC	Principal Stress	Bi-linear	0	1100	485
NSCs003	NSC	Principal Stress	Bi-linear	0	1000	650[b]
NSCs004	NSC	Principal Stress	Bi-linear	0	1300	485
FRC1001	FRC1	Principal Stress	Bi-linear	0	2000	485
FRC1002	FRC1	Principal Stress	Bi-linear	0	1100	485
FRC1003	FRC1	Principal Stress	Bi-linear	0	1000	650[b]
FRC1004	FRC1	Principal Stress	Bi-linear	0	1300	485
FRC2001	FRC2	Principal Stress	Bi-linear	0	2000	485
FRC2002	FRC2	Principal Stress	Bi-linear	0	1100	485
FRC3001	FRC3	Principal Stress	Bi-linear	0	2000	485
FRC3002	FRC3	Principal Stress	Bi-linear	0	1100	485
FRC3003	FRC3	Principal Stress	Bi-linear	0	1000	650[b]

[a] Brief descriptions of tensile-failure models and the parameter δ are found in section 3.2.2; for further documentation see [21]. If $\delta \neq 0$, strain-rate effects on ultimate tensile strength are taken into account.
[b] A 4.5 kg, flat-nosed, steel projectile was used in these simulations.

3.2.2 Material models

The RHT model, developed by Riedel, Hiermayer and Thoma [32], was used for modelling both plain and steel-fibre reinforced concrete. However, some modifications of the model had to be made to conduct this study. The standard version of the RHT model consists of three pressure-dependent surfaces: an elastic limit surface, a failure surface, and a surface for residual strength. It also includes pressure hardening, strain hardening and strain-rate hardening. Furthermore, the deviatoric section of the surfaces depends on the third invariant.

Since the primary effect of adding fibres to concrete is the improved post-cracking behaviour, and moderate volume fractions of steel fibres only result in minor effects on the ultimate tensile and compressive strengths, the only difference used in the material models for plain and steel-fibre reinforced concrete is the failure description in tension, i.e. the post-crack behaviour.

A modified crack-softening behaviour could only be used in combination with the principal-stress-failure model, and not with the hydrodynamic-tensile-failure model, used as default in the RHT material model. In the hydrodynamic-tensile-failure model tensile failure is assumed to occur if the value of the hydrodynamic pressure in a cell falls below a specified limit. When using a modified crack-softening law, the strain-rate dependence of the tensile strength, used in the standard RHT strength model, is cut off. This means that the tensile strength will be unaffected by the strain rate. In an attempt to reintroduce a strain-rate dependence in tension, by use of a subroutine, it was found that this could not be done without getting unwanted effects on the crack-softening behaviour, such as serious underestimations of the

fracture energy. This problem arises from the requirement, built into the program, that the user-defined tensile stress is used only if it falls inside the RHT failure surface. The parameter δ, used to describe the strain-rate dependence in tension in the RHT model, was set to zero in simulations where the modified RHT material model was used. This means that no strain-rate dependence for the ultimate tensile strength is taken into account in these simulations.

In AUTODYN [21] a linear crack-softening law is used to describe the post-crack behaviour in tension. However, a bi-linear crack-softening law is more convenient to use for concrete, since it is a very brittle material and the strength decreases rapidly after the failure initiation. Hence, a modification of the model, allowing for a multi-linear crack-softening relation, has been developed and used in the simulations. The bi-linear crack-softening law proposed by Gylltoft [23] was used for plain concrete, and the one proposed by Löfgren [31] was used for steel-fibre reinforced concrete. In order to see how the parameter δ and the change from hydrodynamic-tensile-failure model to principal-stress-failure model influence the results, simulations with different combinations of these were conducted for the plain concrete.

Three different values of fracture energy, 2000, 4000 and 6000 Nm/m^2, were used in the simulations of steel-fibre reinforced concrete target, Fig. 7. In Table 2 the parameters for the bi-linear crack-softening relation described in section 2.1.2 and approximate values of corresponding steel-fibre volume fractions calculated according to [31] are shown together with the values used for simulations of plain concrete targets.

In order to determine the relation between stress and strain for the crack softening, necessary for calculations in programs following a smeared crack approach, e.g. AUTODYN, a relation between the crack opening, w, and the strain, ε, must be assumed. The crack width is smeared out over a length l_{el}, which is related to the size of the local element. In AUTODYN the length l_{el} is calculated as the diameter of a sphere whose volume equals the volume of the local element [21].

The steel (i.e. the projectile and confining steel around the concrete) is modelled with the von Mises material model without any strain hardening and with a linear EOS. Material parameters for the concrete used in the numerical simulations are shown in Appendix A.

Table 2
Bi-linear crack-softening-relation parameters for steel-fibre reinforced concrete.

Concrete	G_F [Nm/m^2]	a_1 [mm^{-1}]	a_2 [mm^{-1}]	b_2 [mm^{-1}]	w_1 [mm]	w_c [mm]	*No of fibres* [#/cm^2]	V_f [%]
NSC	100	26.4	2.64	0.4	0.025	0.152	0	0
FRC1	2000	26.4	1.32	0.445	0.021	3.379	0.403	0.20
FRC2	4000	26.4	1.32	0.632	0.014	4.794	1.074	0.50
FRC3	6000	26.4	1.32	0.774	0.0086	5.875	1.587	0.75

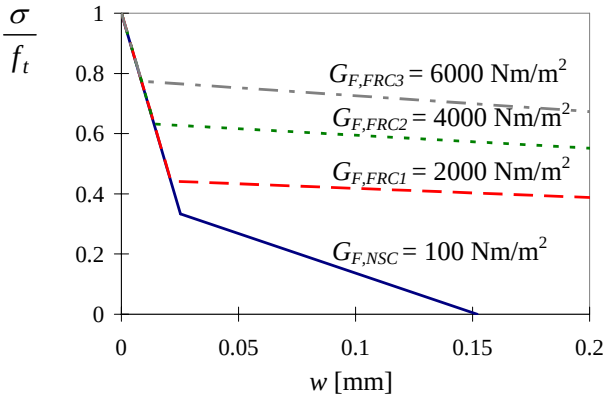

Fig. 7. Crack softening for concrete NSC, FRC1, FRC2 and FRC3.

3.2.3 Mesh

It is well known that the size of the elements used in a numerical mesh affects the results, and that a refined mesh extends the computational time. In the simulations, made in 2D with axial symmetry, quadratic Lagrangian elements with length 5 mm were used for the concrete target. Based on experience,

this element size was found to give reasonable results and a finer mesh was believed not to give an increased accuracy worth the increased computational time. The projectile was modelled with 4 elements across the radius and totally 8 and 4 elements along the length for the ogive-nosed and flat-nosed projectiles, respectively. For the 2 m long concrete target, the steel culvert also covers the rear face of the target, while it does not in the simulations with the shorter cylinders (i.e. 1.0, 1.1 and 1.3 m long targets). Full interaction between the steel culvert and the concrete is assumed in all cases. The numerical mesh for simulations NSCs001 and NSCs003 is shown in Fig. 8.

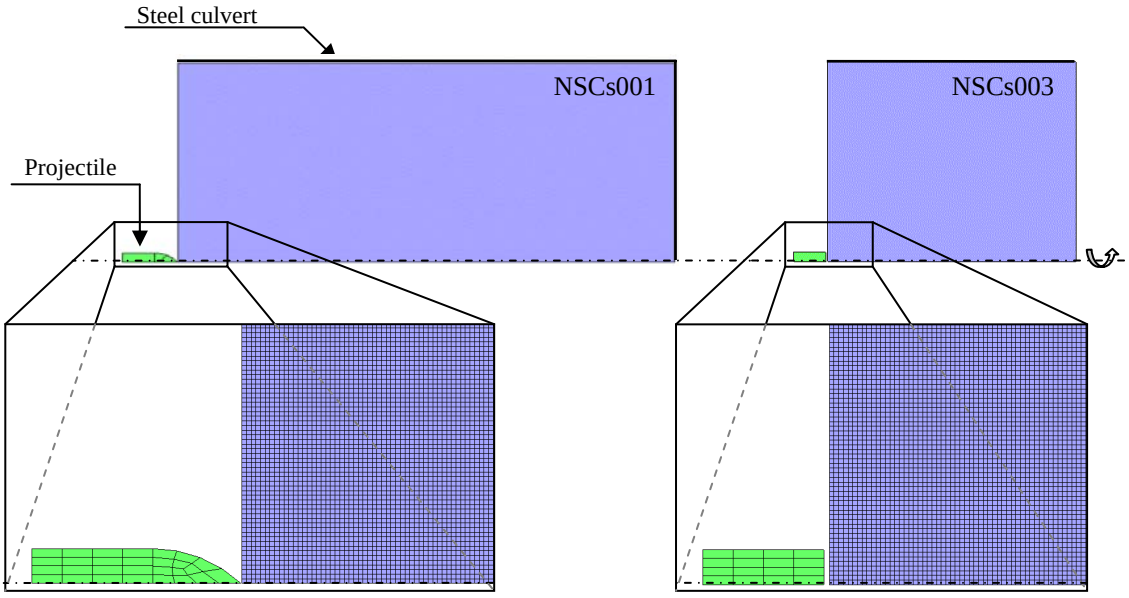

Fig. 8. Numerical mesh for simulation NSCs001 and NSCs003.

4. Results

The results, i.e. the depth of penetration and crater size on front and rear face of the concrete target, from simulations described in section 3.2 are shown in Table 3.

Table 3
Simulation results

Ident	*Depth of penetration [mm]*	*Crater diameter on front face [mm]*	*Crater diameter on rear face [mm]*
NSC001	660	800	0
NSC002	825	740	0
NSC003	1000	700	0
NSCs001	960	1020	0
NSCs002	perforation	860	890
NSCs003	480	840	980
NSCs004	960	920	0
FRC1001	880	560	0
FRC1002	perforation	640	600
FRC1003	430	660	0
FRC1004	950	700	0
FRC2001	900	520	0
FRC2002	perforation	540	530
FRC3001	890	550	0
FRC3002	perforation	550	460
FRC3003	400	660	0

4.1 Effect of tensile-failure description for plain concrete

The standard RHT material model gives a close approximation of the depth of penetration and crater size on the front face of the concrete target, which can be seen when comparing the results from simulation NSC001 to the results from the experiment described in section 3.1; see Fig. 9a. However, the cavitated region in the results from this simulation should have been narrower in order to agree with the experimental results. Since no data of the cavitated region in the experiments are presented in [20] this is not shown in Fig. 9a.

When using a strain-rate independence for the tensile strength (δ=0 in the RHT material model) (NSC002) the depth of penetration increases by 25% compared to the case where the dynamic effect of the tensile strength is taken into account (NSC001), as seen in Fig. 9b. Changing from a hydrodynamic-tensile-failure model (used in NSC002) to a principal-tensile-stress-failure model (NSC003) gives a further increase of the depth of penetration with approximately 20%.

Using a bi-linear crack-softening law for the simulations with plain concrete (NSCs001) results in damage more similar to that estimated with hydrodynamic-tensile-failure model and no strain-rate dependence in tension (NSC002) than the simulations with a linear crack-softening law (NSC003), even though the diameter of the front-face crater is overestimated; see Fig. 9c where the front-face crater size is marked. However, it is to be observed that the size of the crater diameter is ambiguous and depends on the way chosen to analyse the results. In Fig. 10 magnifications of the front-face crater and different ways to measure it are shown for case NSCs001. The unsmoothed damage of the elements is plotted in Fig. 10a and the border of the crater is estimated as the elements where the fully developed crack located furthest from the central line of the cylinder reaches the front face. This method of measuring the crater size is used in the present study. In Fig. 10b and c, the crater sizes are measured by means of the diameter of the fully damaged outermost layer in a smoothed-damage plot and node-velocity vectors, respectively.

The results from the simulations of projectile impact on plain concrete with a bi-linear crack-softening law are used to make a relative comparison of damage in fibre-reinforced concrete impacted by the same projectile.

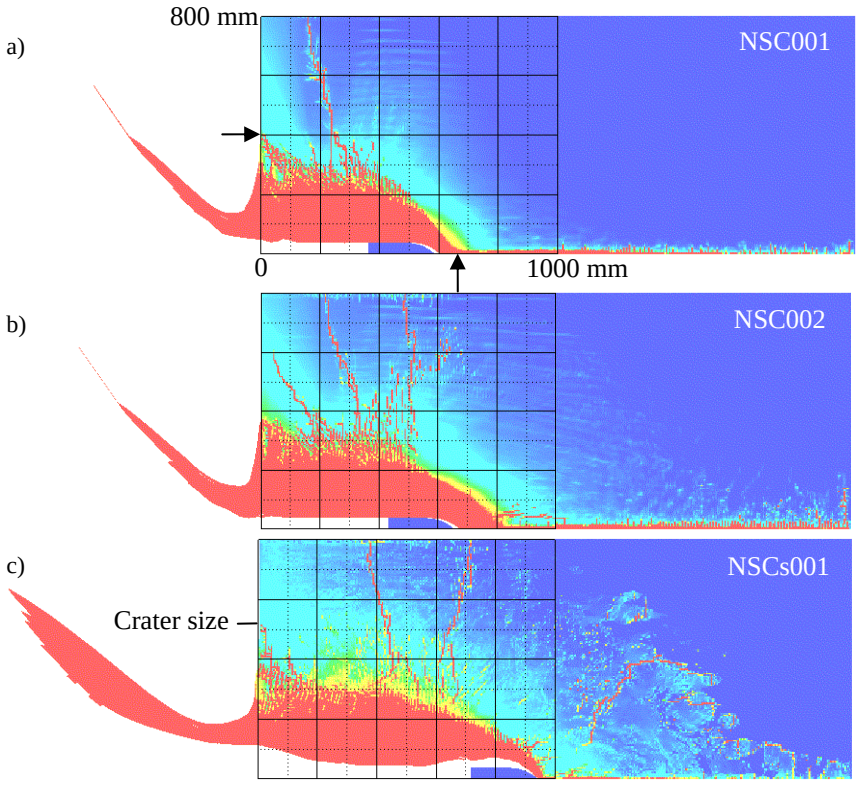

Fig. 9. Simulation results for plain concrete, case (a) NSC001 with standard RHT material model, (b) NSC002 where no strain-rate dependence for tensile strength is used, and (c) NSCs001 with principal-tensile-stress-failure model and bi-linear crack-softening law. The arrows in (a) indicate the crater diameter and penetration depth reported by Hansson [20].

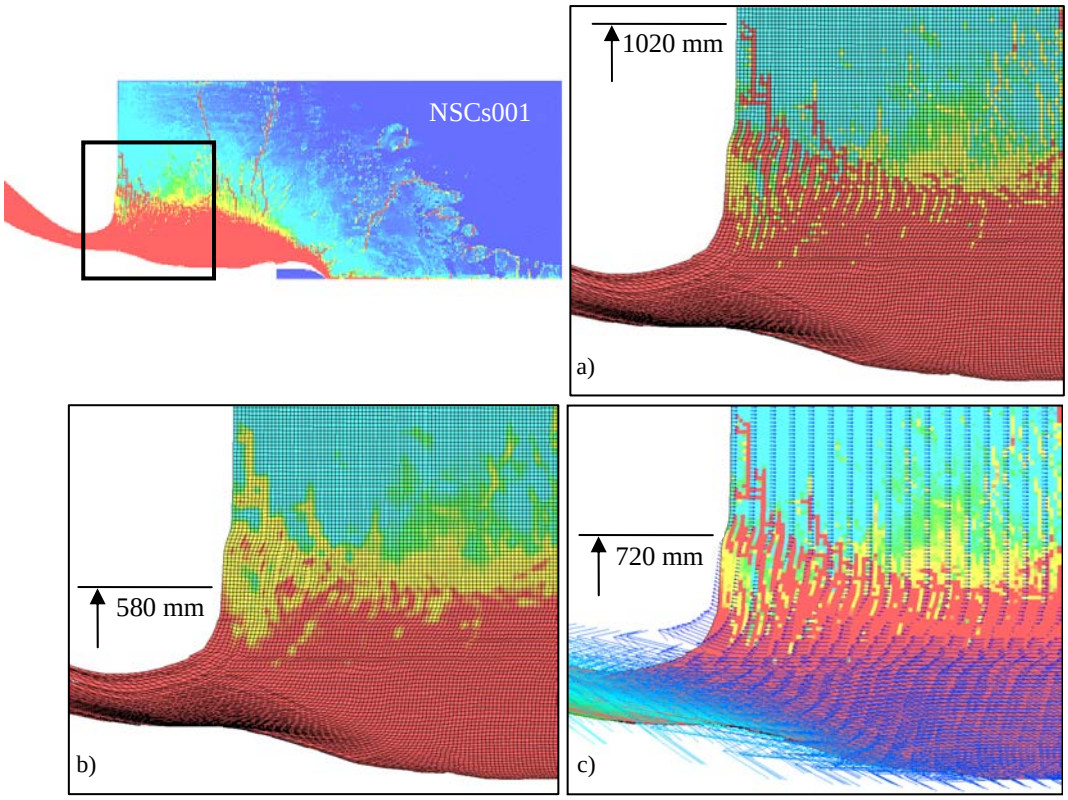

Fig. 10. Magnifications of the front-face crater for case NSCs001 with estimations of its size by use of plots with (a) unsmoothed damage, (b) smoothed damage and (c) node-velocity vectors.

4.2 Effect of adding fibres to plain concrete

The relative effect of adding an approximate fibre-volume fraction of 0.2% to plain concrete can be seen by comparing results from simulations FRC1001-FRC1004 with NSCs001-NSCs004, respectively. In those cases where the projectile stops inside the target, i.e. no perforation occurs, it can be seen that the addition of fibres has a minor influence on the depth of penetration, but also that the influence on the front-face crater size is considerable. The same behaviour is seen when comparing results from simulations with approximate fibre-volume fraction of 0.5% and 0.75% (FRC2001, FRC2002 and FRC3001 and FRC3002) with results from simulations with plain concrete (NSCs001 and-NSCs002). In Table 3 it can also be seen that increasing the fibre content in concrete from a volume fraction of 0.2% to 0.5% results in a decreasing crater size on the front face of the target, but a further increased volume fraction (from 0.5 to 0.75%) does not lead to additional reduction of the crater diameter. Moreover, by comparing Fig. 9 to Fig. 12 it can be seen that the addition of fibres and an increasing dosage of fibres results in reduced crack propagation beyond the crater region

Further, the addition of fibres to plain concrete results in a large reduction of the rear-face crater size, which can be seen when comparing results from simulation NSCs002 with results from FRC1002, FRC2002 and FRC3002. From these results it can also be seen that, unlike the size of the front-face crater, the size of the rear-face crater decreases also when increasing the volume fraction of fibres from 0.5 to 0.75%. In simulations with the ogive-nosed projectile, scabbing could not be differentiated from penetration. However, the flat-nosed projectile used in simulations NSCs003 caused scabbing even though the penetration depth was only half of the target length. In simulations FRC1003 and FRC3003, where the same flat-nosed projectile was used, scabbing does not occur. Even though crack initiation takes place on the rear ends of the targets due to the reflected stress wave also in these cases the effect of the fibres prevents the initiated crack from developing into a continuous crack which causes scabbing, as in case NSCs003.

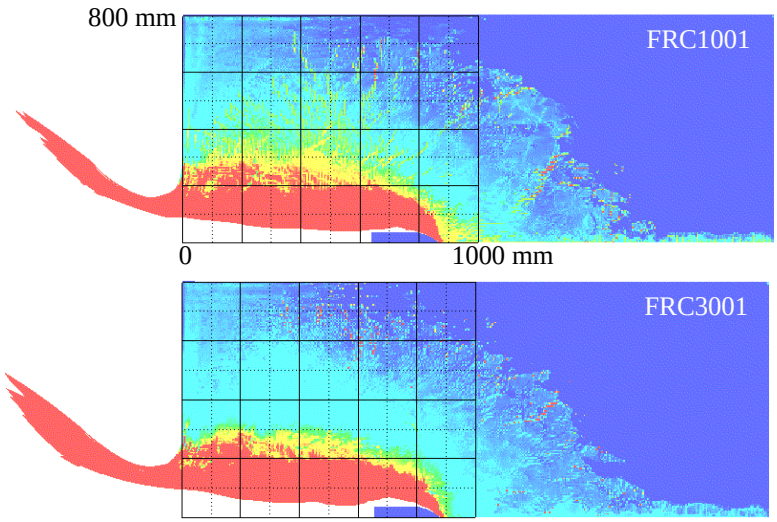

Fig. 11. Simulation results for fibre-reinforced concrete, cases FRC1001 and FRC3001.

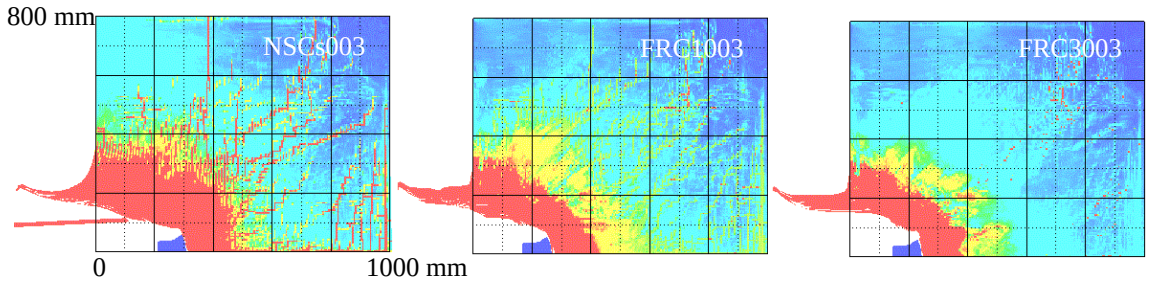

Fig. 12. Simulation results for plain (NSCs003) and fibre-reinforced concrete (FRC1003 and FRC3003).

5. Discussion

The addition of fibres to concrete increases the impact resistance, but the structural behaviours of targets subjected to high-velocity impact are complicated. In order to further study how the addition of various volume fractions of fibres to concrete affect the projectile resistance, numerical simulations were conducted in the programme AUTODYN.

Due to limitations in the numerical-simulation tool, the strain-rate dependence in tension for concrete used in the RHT material model, often used for modelling concrete subjected to projectile or fragment impact, could not be used in combination with a modified crack-softening curve.

When using the standard RHT material model in the numerical simulations the depth of penetration and crater diameter on the front face of the 2.0 m long concrete target agree well with the experimental results. However, the size of the cavitated region is overestimated in the numerical simulation, which, according to [21], may be explained by the simplicity of the hydrodynamic tensile failure. In [21] it is also pointed out that users of the model should avoid drawing conclusions from details within the spalled or cavitated regions. Since the standard RHT material model cannot be used with a modified crack-softening law, necessary to capture the effect of the added fibres in the concrete, the principal-tensile-stress-failure model was used instead of the hydrodynamic-tensile-failure model in the simulations, which also means that the strain-rate dependence of the tensile strength is turned off. These changes led to an increased depth of penetration. The increment caused by the strain-rate independence of the tensile strength was expected since the depth of penetration depends on the tensile strength, but the increased penetration depth due to the change of tensile failure model probably derives from the different ways of taking the third invariant and its dependence on the hydrostatic pressure into account.

Since the fibre-reinforced concrete is not modelled as discrete fibres within a concrete matrix, but the fibres and concrete are instead modelled as one material with an improved post-cracking behaviour compared to plain concrete, the results must be used with care. There are effects of the fibres that get lost due to this simplification. Furthermore, since the effect of the fibres is not notable until after tensile-failure initiation in the concrete (i.e. crack initiation), the results are highly dependent on the crack

distribution within the concrete target. The possibility to predict the real crack distributions within a concrete target by means of numerical-simulation tools is strictly limited, and it should therefore be pointed out that the results presented in this paper should be used in a comparative way and the reader should treat the results with care and avoid drawing conclusions from details in the results.

The relative effect of fibres added to the concrete mix was found by comparing results from simulations of projectile impact on plain concrete, modelled with bi-linear crack-softening in tension, to projectile impact on fibre-reinforced concrete also modelled with bi-linear crack softening, but with larger fracture energies than in plain concrete. In agreement with the literature [7] it was found that the addition of fibres has a negligible effect on the depth of penetration, while it decreases the crater size on both the front and rear face of the target. The influence on the scabbing crater is found to be larger than on the spalling crater, which can be explained by the fact that a considerable part of the damage in the front-face crater is caused by crushing of the material while the scabbing crater is mainly caused by tensile failure, for which the effect of the fibres is larger. For the same reason the effect of increasing the number of fibres is more visible on the rear-face crater than on the front-face crater.

6. Conclusions

The comparative numerical study of the resistance of fibre-reinforced concrete and plain concrete to projectile impact showed that the addition of moderate dosage (<1%) of fibres to concrete gives:

- A negligible decrease of projectile-penetration depth compared to plain concrete.
- A decrease of crater diameter on both front and rear faces of the concrete target, but where the effect on the rear face is larger than on the front face.
- Reduced crack propagation beyond the crater region, so that damage is confined to a more localized volume.

An increasing amount of fibres in the concrete results in a:

- Relatively small size reduction of the front-face crater.
- Decreasing diameter of the rear-face crater in cases where scabbing occurs.
- Reduced crack propagation beyond the crater region.

It can also be concluded that scabbing in concrete structures caused by projectile impact may be prevented by use of fibre-reinforced concrete if scabbing is due to the reflected stress wave caused by the impact alone, and not in combination with the shear-plugging effects from the projectile.

Acknowledgement

The research presented in this paper is done within the research project “Concrete structures subjected to blast and fragment impacts: dynamic behaviour of reinforced concrete”, financially supported by the Swedish Rescue Services Agency. The authors would like to thank the members of the reference group for the research project: Björn Ekengren, M.Sc., at the Swedish Rescue Services Agency, Morgan Johansson, Ph.D., at Reinertsen AB, and Joosef Leppänen, Ph.D., at FB Engineering AB.

References

[1] Zhanga MH, Shimb VPW, Lua G, Chewa CW. Resistance of high-strength concrete to projectile impact. Int J Impact Engng 2005;31:825-841.

[2] Maalej M, Quek SR, Zhang J. Behavior of hybrid-fiber engineered cementitious composites subjected to dynamic tensile loading and projectile impact. J Mater Civil Eng 2005;17(2):143-152.

[3] Nataraja MC, Nagaraj TS, Basavaraja SB. Reproportioning of steel fibre reinforced concrete mixes and their impact resistance. Cem Concr Res 2005;35:2350-2359.

[4] Luo X, Sun W, Chan SYN. Characteristics of high-performance steel fiber-reinforced concrete subject to high velocity impact. Cem Concr Res 2000;30:907-914.

[5] Ong KCG, Basheerkhan M, Paramasivam P. Resistance of fibre concrete slabs to low velocity projectile impact. Cem Concr Res 1999;21:391-401.

[6] Cánovas MF, Pamies RG, Simón del Potro JR, Almansa EM. Impact effects on the primary fragmentation generated by the HE81 mortar grenade on conventional concrete and steel fibers reinforced concrete. In: Bulson PS (ed.). Proceedings of the Third International Conference on Structures Under Shock and Impact, Madrid (Spain): Computational Mechanics Publications, 1994, pp. 37-44.

[7] Almansa, EM, Cánovas MF. Behaviour of normal and steel fiber-reinforced concrete under impact of small projectiles. Cem Concr Res 1999;29:1807-1814.

[8] Johansson M. Structural Behaviour in Concrete Frame Corners of civil Defence Shelters, Non-linear Finite Element Analyses and Experiments. Doctoral Thesis, Department of Structural Engineering, Concrete Structures, Göteborg (Sweden): Chalmers University of Technology, 2000. 220 pp.
[9] Leppänen J. Concrete Structures Subjected to Fragment Impacts, Dynamic Behaviour and Material Modelling. Doctoral Thesis, Department of Structural Engineering and Mechanics, Concrete Structures, Göteborg (Sweden): Chalmers University of Technology, 2004. 127 pp.
[10] Nyström U. Design with regard to explosions. Master's Thesis, Department of Civil and Environmental Engineering, Structural Engineering, Concrete Structures, Göteborg (Sweden): Chalmers University of Technology, 2006. 205 pp.
[11] Nyström U, Leppänen J. Numerical Studies of Projectile Impacts on Reinforced Concrete. In: Fan SC, Chua HK (eds.). Proceedings of the Second International Conference on Design and Analysis of Protective Structures, Singapore (Singapore): Nanyang Technical University, 2006. p. 310-319.
[12] Kennedy RP. A review of procedures for the analysis and design of concrete structures to resist missile impacts. Nucl Eng Des 1976;37:183-203.
[13] Vossoughi F, Ostertag CP, Monteiro PJM, Johnson GC. Resistance of concrete protected by fabric to projectile impact. Cem Concr Res 2007;37:96-106.
[14] Corbett GG, Reid SR, Johnson W. Impact loading of plates and shells by free-flying projectiles: A review. Int J Impact Engng 1996;18(2):141-230.
[15] Chen XW, Li QM. Deep penetration of a non-deformable projectile with different geometrical characteristics. Int J Impact Engng 2002;27:619-637.
[16] Chen XW, Li QM. Oblique and normal perforation of concrete targets by a rigid projectile. Int J Impact Engng 2004;30:617-637.
[17] Tham CY. Numerical and empirical approach in predicting the penetration of a concrete target by an ogive-nosed projectile. Finite Elem Anal Des 2006;42:1258-1268.
[18] Chen XW, Li QM. Dimensionless formulae for penetration depth of concrete target impacted by a non-deformable projectile. Int J Impact Engng 2003;28:93-116.
[19] Forrestal MJ, Frew DJ, Hanchak SJ, Brar NS. Penetration of grout and concrete targets with ogive-nose steel projectiles. Int J Impact Engng 1996;18(5):465-476.
[20] Hansson H. Numerical simulation of concrete penetration. FOA report 98-00816--311--SE, Defence research establishment, Tumba (Sweden), 1998, 17 pp.
[21] ANSYS AUTODYN User Manual, Version 11.0. Concord (CA, USA): Century Dynamics Inc., 2007. 528 pp.
[22] CEB-FIP Model Code 1990. Designe Code, Lausanne, Switzerland: Thomas Telford. 1993. 437pp.
[23] Gylltoft K. Fracture mechanics models for fatigue in concrete structures. Doctoral Thesis, Division of Structural Engineering, Luleå (Sweden): Luleå University of Technology, 1983. 210 pp.
[24] van Mier JGM. Strain-softening of concrete under multiaxial loading conditions. Doctoral Thesis, Eindhoven (The Netherlands): Eindhoven University of Technology, 1984. 349 pp.
[25] Bischoff PH, Perry SH. Compressive behaviour of concrete at high strain rates. Mater Struct 1991;24:425-450.
[26] Ross CA, Jerome DM, Tedesco JW, Hughes ML. Moisture and strain rate effects on concrete strength. ACI Mater J 1996;93(3):293-300.
[27] Weerheijm J. Concrete under Impact Tensile Loading and Lateral Compression. Doctoral Thesis, Delft University of Technology, Delft (The Netherlands), 1992.
[28] Schuler H. Experimentelle und numerische Untersuchungen zur Schädigung von stoßbeanspruchtem Beton (in German). Doctoral Thesis, Universität der Bundeswehr München, Freiburg (Germany): Intitut Kurzzeitdynamik, Ernst-Mach-Institut, 2004. 184 pp.
[29] Brara A, Klepaczko JR. Fracture energy of concrete at high loading rates in tension. Int J Impact Engng 2007;34(3):424-435.
[30] Weerheijm J, van Doormaal JCAM. Tensile failure of concrete at high loading rates: New test data on strength and fracture energy from instrumented spalling tests. Int J Impact Engng 2007;34(3):609-626.
[31] Löfgren I. Fibre-reinforced concrete for industrial construction: a fracture mechanics approach to material testing and structural analysis. Doctoral Thesis, Department of Civil and Environmental Engineering, Structural Engineering, Göteborg (Sweden): Chalmers University of Technology, 2005. 243 pp.
[32] Riedel W. Beton unter dynamischen lasten, meso. und makromechanische modelle und ihre parameter (in German). Doctoral Thesis, Universität der Bundeswehr München, Freiburg (Germany): Institut Kurzzeitdynamik, Ernst-Mach-Institut, 2000. 210 pp.

[33] Attard MM, Setung S. Stress-strain relationship of confined and unconfined concrete. ACI Mater J 1996;93(5):432-442.

Appendix A Model input data

Table 4:
Input data for concrete and steel-fibre reinforced concrete: RHT model.

Parameter	Value	Comments
Shear Modulus [kPa]	$1.433 \cdot 10^7$	a
Compressive Strength f_c [kPa]	$3.38 \cdot 10^4$	a
Tensile Strength f_t/f_c	0.078	a
Shear Strength f_s/f_c	0.18	b
Intact Failure Surface Constant *A*	2	c
Intact Failure Surface Exponent *N*	0.7	c
Tens./Compr. Meridian Ratio	0.6805	b
Brittle to Ductile Transition	0.0105	b
G(elastic)/G(elastic-plastic)	2	b
Elastic Strength/f_t	0.7	b
Elastic Strength/f_c	0.53	b
Fractured Strength Constant *B*	1.5	c
Fractured Strength Exponent *M*	0.7	c
Compressive Strain Rate Exponent α	0.032	b
Tensile Strain Rate Exponent δ	0, 0.025	d
Maximum Fracture Strength Ratio	$1 \cdot 10^{20}$	b
Use CAP on Elastic Surface	Yes	b
Damage Constant *D1*	0.04	b
Damage Constant *D2*	1	b
Minimum Strain to Failure	0.01	b
Residual Shear Modulus Fraction	0.13	b
Tensile Failure	Hydro, Principal Stress	e
Principal Tensile Failure Stress [kPa]	$2.6364 \cdot 10^3$	
Maximum Principal Stress Difference/2	$1.01 \cdot 10^{20}$	b
Crack softening	Yes	
Fracture energy [Nm/m^2]	100, 2000, 4000, 6000	f
Flow Rule	No-bulking	b
Stochastic Failure	No	b
Erosion Strain/Instantaneous Geometric Strain	1.5	g

a. Calculated according to CEB-FIB Model Code 1990 [22].
b. Default value in AUTODYN material library for concrete with compressive strength of 35 MPa.
c. Determined by Leppänen [9], based on model proposed by Attard and Setunge [33].
d. No strain-rate dependence of tensile strength used in combination with modified RHT material model: for standard RHT model the δ parameter is set to 0.025.
e. Principal-stress-failure model is used in modified RHT material model, and hydrodynamic-tensile-failure model for standard RHT material model.
f. G_F = 100 Nm/m^2 for plain concrete and G_F = 2000, 4000 and 6000 Nm/m^2 for the steel-fibre reinforced concrete.
g. Calibrated by parameter studies; see Nyström [11].

Table 5:
Input data for concrete: equation of state (EOS).

Parameter	Value
Reference Density [g/cm^3]	2.75
Porous Density [g/cm^3]	2.4
Porous Sound Speed [m/s]	2920
Initial Compaction Pressure [kPa]	$2.33 \cdot 10^4$
Solid Compaction Pressure [kPa]	$6 \cdot 10^6$
Compaction Exponent	3
Solid *EOS*	Polynomial
Bulk Modulus *A1* [kPa]	$3.527 \cdot 10^7$
A2 [kPa]	$3.958 \cdot 10^7$
A3 [kPa]	$9.04 \cdot 10^6$
B0	1.22
B1	1.22
T1	$3.527 \cdot 10^7$
T2	0
Reference Temperature [K]	300
Specific Heat [J/kgK]	654
Thermal Conductivity [J/mKs]	0
Compaction Curve	Standard

Paper II

Numerical studies of the combined effects of blast and fragment loading
Nyström, U. and Gylltoft, K.

Submitted to *International Journal of Impact Engineering*, April 2008

Numerical studies of the combined effects of blast and fragment loading

Ulrika Nyström*, Kent Gylltoft

Department of Civil and Environmental Engineering, Structural Engineering, Concrete Structures, Chalmers University of Technology, SE-412 96 Göteborg, Sweden
(*ulrika.nystrom@chalmers.se)

Abstract

The well-known synergetic effect of blast and fragment loading, observed in numerous experiments, is often pointed out in design manuals for protective structures. However, since this synergetic effect is not well understood it is often not taken into account, or is treated in a very simplified manner in the design process itself. A numerical-simulation tool has been used to further study the combined blast and fragment loading effects on a reinforced concrete wall. Simulations of the response of a wall strip subjected to blast loading, fragment loading, and combined blast and fragment loading were conducted and the results were compared. Most damage caused by the impact of fragments occurred within the first 0.2 ms after fragments' arrival, and in the case of fragment loading (both alone and combined with blast) the number of flexural cracks formed was larger than in the case of blast loading alone. The overall damage of the wall strip subjected to combined loading was more severe than if adding the damages caused by blast and fragment loading treated separately, which also indicates the synergetic effect of the combined loading.

Key-words: Numerical simulation, Blast load, Fragment impact, Combined loading, Concrete

---

1 Introduction

The combined loading of blast and fragments, caused by explosions, is considered to be synergetic in the sense that the combined loading results in damage greater than the sum of damage caused by the blast and fragment loading treated separately, [1]. This is a well-known phenomenon pointed out in some of the literature and design manuals within the area of protective design [2]. However, due to the complex nature of the effect of combined loading, its high parameter dependence and the limited number of documentations and comparable experiments, the design manuals often disregard the effect or treat it in a very simplified manner.

In order to increase the understanding of the combined effects of blast and fragment loading, numerical simulations were conducted. The simulations consist of a wall strip subjected to blast and fragment loading, applied both separately and simultaneously. Both the wall strip and the loads used in the simulations are based on requirements of protective capacity stated in the Swedish Shelter Regulations, [3]. Using a numerical-simulation tool is motivated by e.g. the high cost of undertaking tests, and the possibility to better follow and understand the principal phenomena related to this kind of loading.

This work is a substudy within a project with the long-term aim to study and increase the knowledge of blast and fragment impacts, and the synergy effect of these loads, on reinforced concrete structures. The research project is a collaboration of many years' duration between Chalmers University of Technology and the Swedish Rescue Services Agency. In earlier studies within the framework of this project, the effect of blast waves in reinforced concrete structures, fragment impacts on plain concrete, and design with regard to explosions and concrete, reinforced and fibre-reinforced, subjected to projectile impact were studied by Johansson [4], Leppänen [5] and Nyström [6,7], respectively.

2 Theoretical framework

2.1 Weapon load characteristics

As detonation of the explosive filler in a cased bomb is initiated, the inside temperature and pressure will increase rapidly and the casing will expand until it breaks up in fragments. The energy remaining after swelling and fragmenting the casing, and imparting velocity to the fragments, expends into the surrounding air and thus creates a blast wave. Thereby, the structures around a bomb detonation will be exposed to both blast and fragment loading, which means that at least three types of loading effects must be considered:

- impulse load from blast wave
- impulse load from striking fragments
- impact load from striking fragments

where impulse is considered to give a global response and impact a local response caused by the penetration of the fragments.

There are many different types of weapons, designed to have a specific effect on the surroundings. In design of protective structures a threat-determination methodology, based on probability aspects, must be used to decide what load conditions the structure is to be designed for. There are methodologies for calculating the characteristics of the blast and fragment loads caused by explosion, which are well accepted in the design of protective structures. However, even though the blast load characteristics for a bare high-explosive detonation can be estimated with great accuracy, the loads from a cased bomb cannot be determined as accurately [2]. Due to the complexity of not only the blast itself but also the fragmentation of the casing, these load estimations are more uncertain.

Since the properties of the bomb (geometry, casing material and thickness, type of explosive filler, etc.) and its position relative to the target, as well as the surrounding environment, have influence on the loading conditions, all these parameters must be considered during analysis of the loading effect. Also the distance from the detonation (stand-off) will greatly influence the loading properties. This is mainly due to the change in peak pressure for the blast wave and the change in velocity of the fragments, which both decrease with increasing distance. The retardation of the blast wave is larger than that of the fragments, leading to a difference in arrival time; see Fig. 1. In the range closest to the bomb, i.e. within a few metres, the blast wave will reach the target before the fragments, while at larger distances the fragments will arrive before the blast wave. For a 250 kg general-purpose bomb (GP-bomb), with 50 weight per cent TNT, the blast front and the fragments will strike the target at the same time at an approximate distance of 5 metres.

Fig. 1. Time of arrival for blast wave and fragments as functions of the stand-off for a 250 kg GP-bomb with 50 weight per cent TNT, from [5].

2.1.1 Blast loading

The blast load resulting from a detonation of an uncased charge in "free air", i.e. distant from the nearest reflecting surface, is well known and often idealised as shown in Fig. 2. The detonation takes place at time $t = 0$ and arrives at the point studied at time t_a. As the blast wave arrives, the pressure increases from the ambient pressure, P_0, to $P_0+P_s^+$, where P_s^+ is the incident overpressure caused by the

detonation. As time goes on, the overpressure decays and at time T^+ after the time of arrival the pressure is again equal to the ambient pressure P_0 and the positive phase is over. Due to a partial vacuum formed behind the blast front [8] a negative pressure P_s^- (relative to the ambient pressure) appears and the negative phase is entered. The duration of the negative phase is longer than the positive phase, but the amplitude of the negative pressure is limited by the ambient pressure, P_0, and is often small compared to the peak overpressure, P_s^+. However, in design with regard to explosions the negative phase is considered less important than the positive phase and is therefore often disregarded.

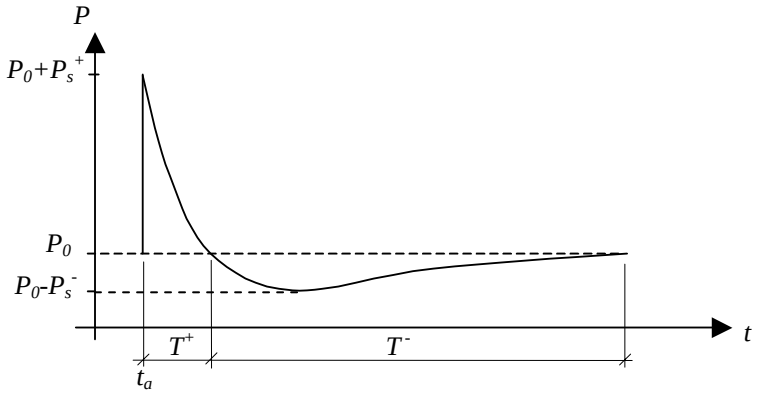

Fig. 2. Incident blast wave idealisation for 125 kg TNT at 5 meters stand-off, based on [4].

As the blast wave strikes a surface, e.g. a wall, it is reflected and its behaviour changes. The so-called normal reflection, taking place as the blast wave is reflected against a perpendicular surface, may lead to significantly enhanced pressures, where the reflected peak overpressure P_r^+ will be between 2 and 8 [2], and according to [8,9] as much as 20, times higher than the incident overpressure P_s^+. According to [10] the shape of the reflected pressure has the same general shape as the incident pressure, as shown in Fig. 3.

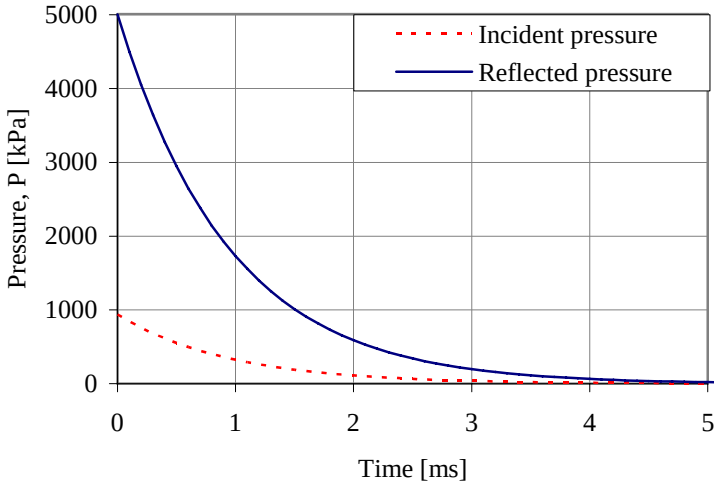

Fig. 3. Positive phase of reflected and incident blast wave for 125 kg TNT at 5 metres stand-off, calculated according to [10].

For cased charges the blast load characteristics depend not only on the type and amount of explosive and the stand-off distance, but also on the properties (geometrical and material) of the casing. Since there is less knowledge about how the casing affects the blast wave, there are also less generic expressions describing this. In [11] an expression for calculating an equivalent uncased charge weight is given as a function of the ratio between the casing weight and the actual charge weight. However, the reduced blast pressure due to the energy consumed during casing break-up is often not taken into account in the design manuals [2], which also is used in this study.

2.1.2 Fragment loading

As mentioned earlier, the casing of a bomb will swell after initiation of the explosive filler due to the high pressure. During swelling, cracks will form and propagate in the casing; and as the cracks meet or reach a free border, fragments are formed [12]. The nose and the tail section of the bomb will break up in a smaller number of massive fragments and the body will fracture into many small fragments.

Derivation of theoretical expressions describing the fragmentation process and its characteristics for cased bombs is difficult. This is partly due to the complexity of the phenomenon itself and partly due to the great variation of bomb properties, which highly influences the fragmentation process. However, there are expressions for estimating the mass distribution and velocities of the fragments that are based on theoretical considerations and confirmed with a large number of tests [13]. In the derivation of these expressions, the bomb casing is normally idealised as a cylinder with evenly distributed explosives, meaning that the methods apply especially to items that can reasonably be approximated as either cylindrical items or as a series of cylindrical items [13]. The more an item deviates from this ideal, the less reliable are the estimations made using these methodologies.

In order to estimate the fragment mass distribution, a relationship developed by Mott [14,15] (presented in e.g. [13,16]) is often used. For design purposes a design fragment is used. The mass of the design fragment is often determined by specifying a confidence level giving the probability that the weight of the fragment is the largest fragment produced. However, this method of determining the design fragment is justified in design where the damage caused by the individual fragments is of interest as the hazardous case. In the case of design against the fragment cluster, another approach may be more desirable where the combined effect of the fragment impact and impulse is of interest. This is discussed further in Section 4.2.

The initial velocity of the fragments can be estimated from the Gurney equation [17] (presented in e.g. [13,16]), which also derives from an assumption of a cylindrical casing. Since this equation is based on energy balance within the explosive and metal case system, without taking into account the loss of energy during rupture of the casing, it is an upper bound estimation.

As the fragments travel through the air their velocity will decrease due to the air resistance. Smaller, lighter fragments will retard faster than larger, heavier fragments. Equations describing this behaviour exist as well, e.g. [13,16].

2.2 Concrete behaviour under static and dynamic loading

It is well known that the two most pronounced disadvantages of concrete are its low tensile strength and brittle behaviour. The tensile strength of normal-strength concrete is less than one tenth of the compressive strength, and after fracture initiation, i.e. after the tensile strength is reached, the ability to transfer stresses through the material decreases rapidly. For high-strength concrete the brittle behaviour can also be seen in the case of uni-axial compression, but the post-fracture ductility in compression increases, with a decreasing compressive strength.

In multi-axial loading conditions the behaviour of concrete differs from the behaviour under uni-axial loading. The ductility, stiffness and strength in compression increase with increased confinement, and for very high lateral pressures the compressive strength may be more than 15 times higher than the uni-axial compressive strength [5]. Such high lateral pressures may occur during impact and perforation of e.g. projectiles and fragments.

High dynamic loading, giving a high strain rate in the material, also affects the strength and ductility of the concrete. In the case of high-rate tensile loading, the ultimate uni-axial tensile strength may be as much as 5 to 7 times higher than the static tensile strength [18], and even though the effect on the ultimate compressive strength is less pronounced it may still be more than doubled [19]. It has recently also been indicated that the fracture energy is strain-rate-dependent [20-22].

3 Method

Tests have been conducted around the world to study the combined effects of blast and fragment loading, but these are often not suitable for drawing general conclusions about the local or global structural behaviour. This is due to the great variation of parameters involved, e.g. load characteristics and stand-off, which affects the results. Numerical simulations are often used to investigate the effect of blast and fragments, and make it possible to study the influence of different parameters – stand-off

distance, fragment size, materials etc. – which is costly in experimental testing. Nevertheless, the numerical simulations cannot fully supersede experiments, but should be used in combination, and experiments are needed to verify the numerical models used in the simulations.

The reinforced concrete structure used in the study presented here corresponds to a wall strip in a civil defence shelter, fulfilling the requirements of protective capacity related to conventional bombs in the Swedish Shelter Regulations [3]. The loads applied, i.e. the blast wave and fragment loading, also correspond to the load definitions in [3].

As no suitable experiments, with combined blast and fragment loading, were found for this study, two separate experiments on blast load and single fragment impact were used to verify and calibrate the numerical model. The validation and calibration process was done within a preliminary study and is only briefly described in this paper. Conclusions from the preliminary study were used to build up the numerical model of the wall strip subjected to blast and fragment impacts used in the main study. Single-degree-of-freedom analyses were used to find what load combination caused the largest deflection: simultaneous arrival of the two loads, blast load arriving first, or fragments arriving first. The results from the SDOF analyses were used to decide the arrival times for the loads in the numerical simulation of combined loading. The numerical results of the wall-strip response were compared and analysed in order to see the effects of combined loading.

For further information about this study the reader is referred to [23] where a detailed description of the load characterisation and the preliminary study is presented.

4 Wall element and load characteristics

The Swedish Shelter Regulations [3] govern the design of civil defence shelters in Sweden, and contain the requirements specified for these protective structures. Here only the criteria for protective capacity related to conventional bombs are specified, but it should be pointed out that civil defence shelters also are designed to withstand e.g. radioactive radiation, chemical and biological warfare, and explosive gases.

According to [3], a civil defence shelter should be designed to withstand the effect of a pressure wave corresponding to that produced by a 250 kg GP-bomb with 50 weight per cent TNT, which bursts freely outside at a distance of 5.0 metres from the shelter during free pressure release. Further, the shelter must also be able to withstand the effect of fragments from a burst as described above. In the case of fragment loading it is the fragment cluster that is meant, while larger individual fragments may damage and penetrate the shelter.

4.1 Wall element

In the Swedish Shelter Regulations [3], the civil defence shelter is conceived as a reinforced, solid concrete structure. For a shelter without backfilling the minimum thicknesses of the roof, walls and floor are specified as 350, 350 and 200 mm, respectively, and the concrete should fulfil a requirement of at least C25/30, according to [24] (corresponds to mean cylindrical compressive strength of 25 MPa). Hot-rolled reinforcement bars with a specified requirement of strain hardening must be used. The reinforcement must be placed in two perpendicular alignments in both edges of the structural element and the minimum and maximum reinforcement content is 0.14 and 1.10%, respectively. A minimum reinforcement-bar diameter of 10 mm and maximum bar spacing of 200 mm are required, with a maximum concrete cover of 50 mm.

The wall studied has a total height of 3 metres and is simplified to be simply supported with a span length of 2.7 m, as seen in Fig. 4. The rough simplification of the support conditions was not made in an attempt to imitate the real behaviour of the wall.

In [3], equivalent static loads, representing the weapon effect, are used in the design process. A static load of 50 kN/m^2 is used to calculate the required amount of reinforcement in the walls, giving reinforcement bars ø10 s170 (465 mm^2/m in each face of the wall element). Deformed reinforcement bars (B500BT), with a yield strength of 500 MPa were assumed and the distance from concrete edge to centre of reinforcement bars was chosen as 35 mm. The concrete was assumed to have a concrete strength of 35 MPa.

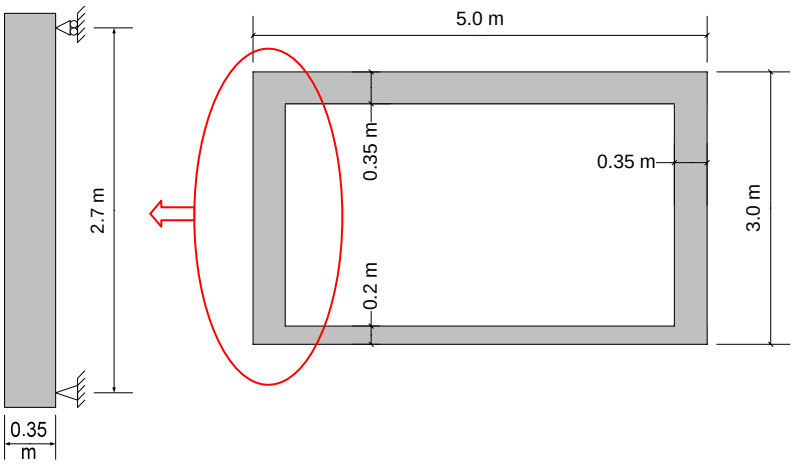

Fig. 4. Civil defence shelter and simplified model of one of its walls.

4.2 Load characteristics

In Fig. 5 the blast load caused by the GP-bomb specified in Section 4 with a stand-off of 5.0 metres, calculated with ConWep [25], is shown together with a simplified relationship. It should be kept in mind that design codes do often not take into account the energy consumed for swelling and fragmenting the casing of bombs. As an approximation this energy loss is also neglected in the present study even though it would be more accurate to reduce the pressure of the blast load in order to imitate the real behaviour. The blast load is assumed to be uniform over the wall, which is reasonably accurate for this stand-off [4]. The impulse density of the blast load is, according to [25], 2 795 Ns/m^2.

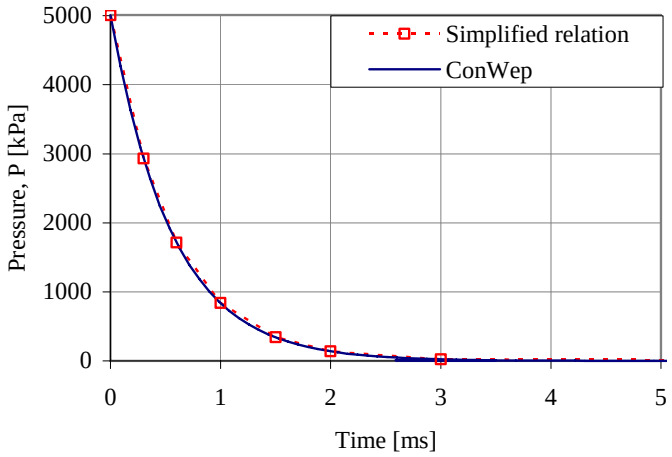

Time [ms]	Pressure [kPa]
0.0	5 006
0.3	2 930
0.6	1 713
1.0	836
1.5	340
2.0	137
3.0	22
8.974	0

Fig. 5. The reflected pressure load as function of time for 125 kg TNT at a distance of 5.0 metres, according to ConWep [25], and the simplified relationship for this which is used in this study, based on [4].

Since the geometry and casing material of the bomb used in the design of civil defence shelters are not specified, the size and mass distribution cannot be calculated without making certain assumptions. In this study, the American GP-bomb Mk82 was used as a reference when estimating the mass distribution of the bomb specified in the Swedish Shelter Regulations. According to ConWep [25] the Mk82 has a nominal weight of 500 lb (226.8 kg) and contains 192.0 lb (87.09 kg) of the high explosive H-6, corresponding to 242.9 lb (110.2 kg) equivalent weight of TNT, and is therefore relatively close to the bomb specified in the Swedish Shelter Regulations [3]. The mass distribution was estimated by scaling the inner casing

diameter and the casing thickness to correspond to the somewhat increased volume of explosive filler compared to the Mk82; for more details see [23].

In order to reduce the complexity of both the numerical model and the results produced, all fragments were assumed to be spherical and of the same size, corresponding to a design fragment. It was further assumed that the fragments were uniformly distributed over the wall.

As mentioned in Section 2.1.2, the design fragment, calculated with a confidence level (often taken as 95%), is used for design with regard to fragment impact. However, this design fragment and the corresponding effect on the target are not representative of the fragment impulse load, so another approach must be used to find a representative fragment size in this study. It was decided to use the impulse caused by the fragments to define a representative weight of the fragments; from estimations of the mass and velocity distribution among the fragments, the corresponding fragment impulse distribution was calculated, and a representative fragment size was determined as the fragment mass giving the average impulse on the structure, for details see [23]. This resulted in a fragment mass of 21.9 g and a fragment diameter of 17.5 mm. The initial fragment velocity was calculated to approximately 1 890 m/s (by use of the Gurney equation), and at the distance of 5.0 metres the velocity is decreased to 1 760 m/s. The fragment density is approximately 0.65 kg/m^2 and the corresponding impulse intensity caused by the fragments is 1 125 Ns/m^2.

4.3 SDOF estimations

The single-degree-of-freedom method (SDOF method) was used in order to find what combination of arrival times of the blast and fragment load that resulted in the maximum deflection. The simplified relation of the blast load, presented in Section 4.2, was used for the blast load and a triangular load was assumed for the fragment loading. The duration of the fragment loading was assumed to 0.1 ms, which is the approximate time it takes for the fragment to penetrate the concrete, and its impulse intensity was as defined in Section 4.2, giving a peak pressure of 22.5 MPa. It should be pointed out that only the impulse load of the fragments was taken into consideration in the SDOF analyses presented in this paper, since the penetration by the fragments and the subsequent damage were not considered. An ideal-plastic material response of the SDOF system was used and the maximum value of the internal dynamic resistance R_m of the wall strip was calculated to be 275 kN; for details see Appendix A and [23].

In Fig. 6 the results are shown for five different cases of combined loading:

1. loads arrive at the same time (simultaneous loading)
2. blast wave first, fragments arrive at maximum wall velocity caused by the blast
3. blast wave first, fragments arrive at maximum wall deflection caused by the blast
4. fragments first, blast wave arrives at maximum wall velocity caused by the fragments
5. fragments first, blast wave arrives at maximum wall deflection caused by the fragments

As seen, the case of simultaneous loading causes the most severe deflection (equalling 139.2 mm at time 42.2 ms). For further information about the SDOF method the reader is referred to [6] and [16].

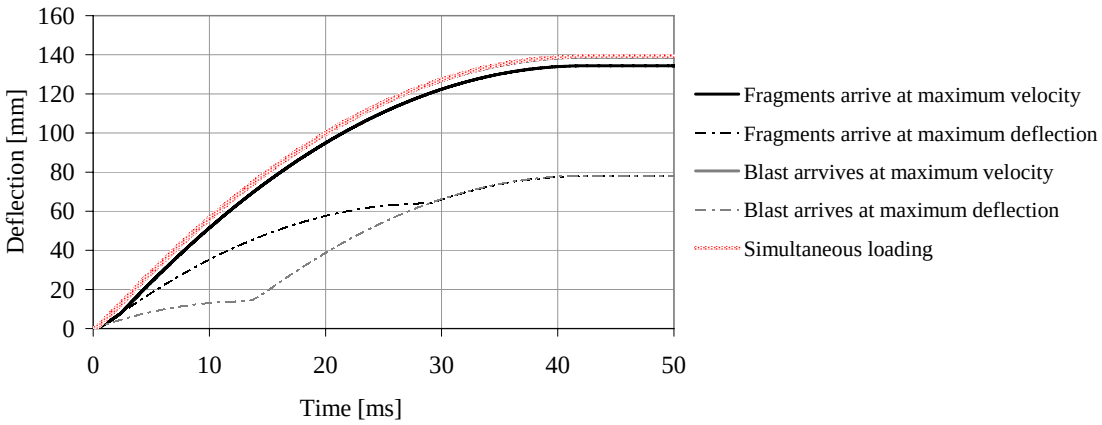

Fig. 6. Mid-point deflection of wall strip subjected to blast load and fragment impulse load, calculated with SDOF method. Since the response of simultaneous loading and loading where fragments arrive first and blast at time of maximum velocity are almost identical these lines are seen as one in the figure.

5 Numerical model

Hydrocodes are used for highly time-dependent dynamic problem-solving by use of finite difference, finite volume and finite element techniques. The differential equations for conservation of mass, momentum and energy, together with material models, describing the behaviour of the materials involved, and a set of boundary conditions give the solution of the problem. The numerical hydrocode AUTODYN 2D and 3D [26] was used in this study, and the Lagrangian solver technique was employed.

5.1 Calibration and validation of numerical model

Experiments and findings from numerical simulations of experiments described in the literature were used in the calibration and validation process for the numerical model used in this study. The numerical simulations for the calibration process were performed in 2D and 3D. The latter with the width of one element and use of boundary conditions to emulate a 2D simulation and thereby reduce the computational time. Below is a brief summary of the calibration and validation process; for further description see [23].

Magnusson and Hansson [27] described experiments on reinforced concrete beams, of length 1.72 m, subjected to blast loading, and thereafter used AUTODYN 3D to simulate the beam response. They concluded that it was possible to simulate the beam response with the RHT material model provided that the principal-stress tensile-failure model with an associated flow rule (in AUTODYN named Bulking) was used in the simulations, together with crack softening. This was also found by means of numerical simulations of the same experiment conducted within the calibration process made in the study presented here. In this process it was also found that an element length of 12 mm gave approximately the same beam response as a finer mesh of 6-mm elements; hence, the coarser mesh of 12-mm elements should be accurate enough to simulate the beam response when subjected to blast loading.

Leppänen [28] performed and described experiments with a single fragment impacting a concrete block, with size 750 x 350 x 500 mm. An AUTODYN 2D model with axial symmetry and different element sizes (1 and 2 mm) was used in the calibration process, and it was concluded that the numerical model gave accurate results. However, the size of the fragment used in [28] differed from the fragment size used in this study, and hence, additional 2D simulations were conducted to investigate the effect of the element size. It was concluded that the resulting crater in the simulations with an element size of 6 mm was somewhat different from the experimental crater, but still an acceptable approximation of the damage caused by the fragment impact. Thus, it was not considered worth the greatly increased computational time to use a finer mesh in the main study.

5.2 Material models

The standard material model for concrete with compressive strength of 35 MPa in the material library of AUTODYN was used to describe the behaviour of concrete. This material model was developed by Riedel, Hiermayer and Thoma (therefore called the RHT model) [29], and consists of three pressure-dependent surfaces in the stress space. The RHT model also takes into account pressure hardening, strain hardening and strain-rate hardening as well as the third invariance in the deviatoric plane. However, the preliminary study, i.e. the calibration and validation process described in Section 5.1, showed that it was necessary to make some modifications within the model to get accurate results. For example, it was concluded that the principal-stress tensile-failure model was necessary to describe the behaviour of the wall strip in the case of blast loading. The change to a principal-stress tensile-failure model leads to a cut-off of the strain-rate dependence of the ultimate tensile strength.

To describe the behaviour of the reinforcing steel, a piecewise linear Johnson-Cook material model was used, including strain hardening but not strain-rate effects. A linear elastic steel material model, with a shear modulus of 81.1 GPa, was used for the supports, and a von Mises material model, simplifying the material behaviour to linear-elastic–ideal-plastic with yield strength of 800 MPa, was used for the fragments. For further information about the material models used, the reader is referred to [23,29,30].

5.3 Mesh

Since fragment penetration is a local effect, requiring relatively small elements, a numerical model of even a 1.0-metre wide strip of the shelter wall would have been very large and required extensive computational time. By use of symmetries and planar-strain-boundary conditions the model was limited to a 84 x 1 512 x 350 mm part of the wall, representing 4.25% of a metre-wide wall strip.

Due to the varying need of element sizes when simulating the effects of blast and fragment impact, a finer mesh of Lagrangian elements (size 6 x 6 x 6 mm) was used on the front face of the wall strip, and a coarser mesh of elements (size 12 x 12 x 6 mm) of the same element type was used on the rear side of the wall strip; see Fig. 7.

The wall strip was supported by two semicylindrical supports with a radius of 84 mm to avoid local crushing of the elements around the supports. The nodes of the support were joined together with the interfacing concrete nodes. In order to allow for rotation around the supports only the line of back nodes was prevented from moving in the x-direction. The supports were modelled with 4 elements along the radius of the half-cylinders.

In the simulations including impacting fragments, these were modelled with two elements along their radius. Embedded beam elements with the same length as the surrounding concrete elements and with circular cross-section were used to model the reinforcement bars.

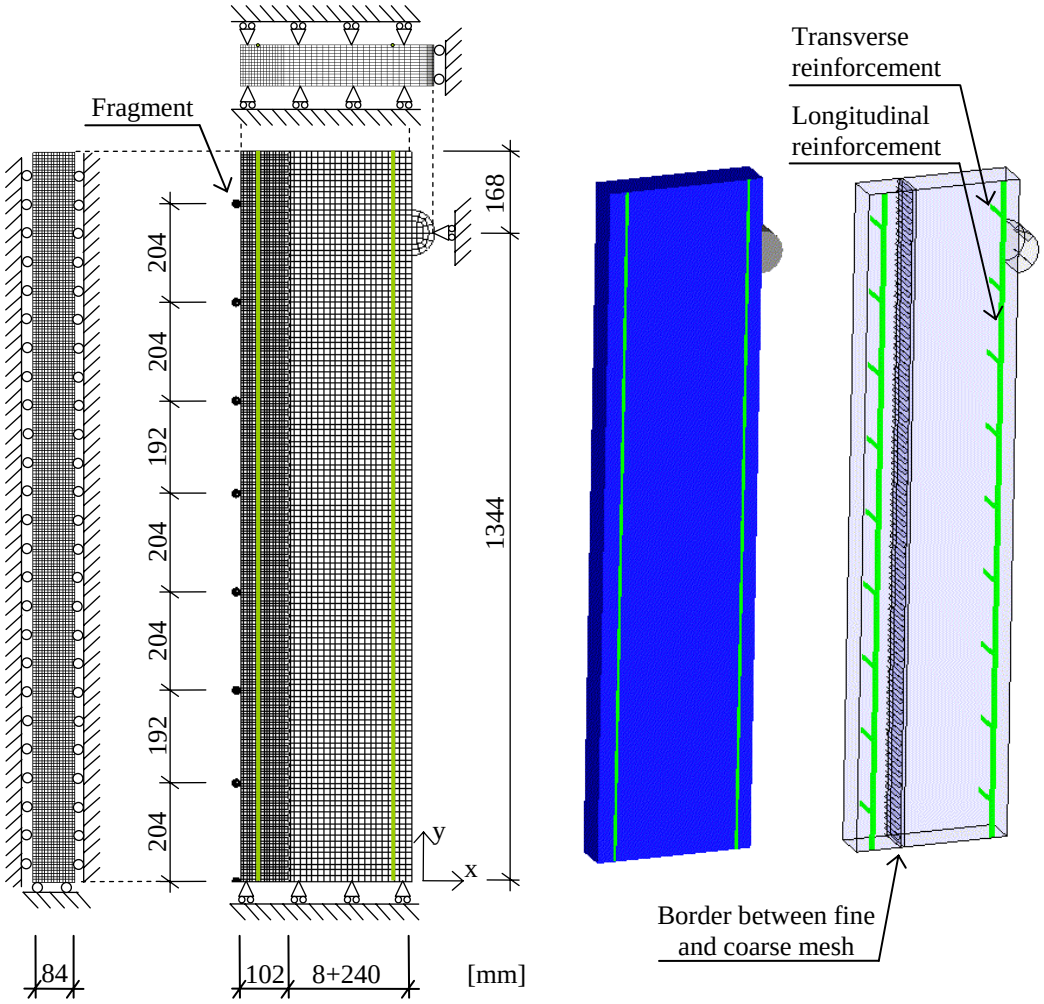

Fig. 7. Numerical mesh of wall strip used in simulations, also showing reinforcement in the modelled wall strip.

6 Results

The responses of the wall strip estimated in the numerical simulations for blast loading, fragment loading, and combined blast and fragment loading (simultaneous loading) are presented and discussed below. As the damage differs at different locations within the wall strip, the damage is shown in three views for each case: a top view, a side view at the section of reinforcement, and one in the middle of the wall strip (the section where the fragments strike the wall strip). In the figures with the wall strip responses, the colour red indicates fully damaged concrete.

6.1 Blast loading

In the case of blast loading, the maximum deflection is 65.2 mm and takes place 29.0 ms after the arrival. In Fig. 8 the damage in the wall strip is shown at time of maximum deflection, where it can be seen that cracks have formed at the rear side of the wall strip and have propagated towards the front face. The damage is localised to relatively few cracks, even though it can be seen that crack initiation has taken place rather densely along the length of the strip. Damaged concrete can also be seen along the reinforcement close to the fully developed cracks; at these locations the reinforcement bars were yielding.

When studying the crack development, it was seen that the localised crack closest to the support was formed already after 1 ms, while no damage of the concrete was observed in the middle of the beam at this time. This indicates a direct shear crack due to the inertia effects, i.e. internal momentum, related to severe dynamic loading. After approximately 2 ms, also the localised cracks in the middle of the beam have formed, and these have the character of flexural cracks.

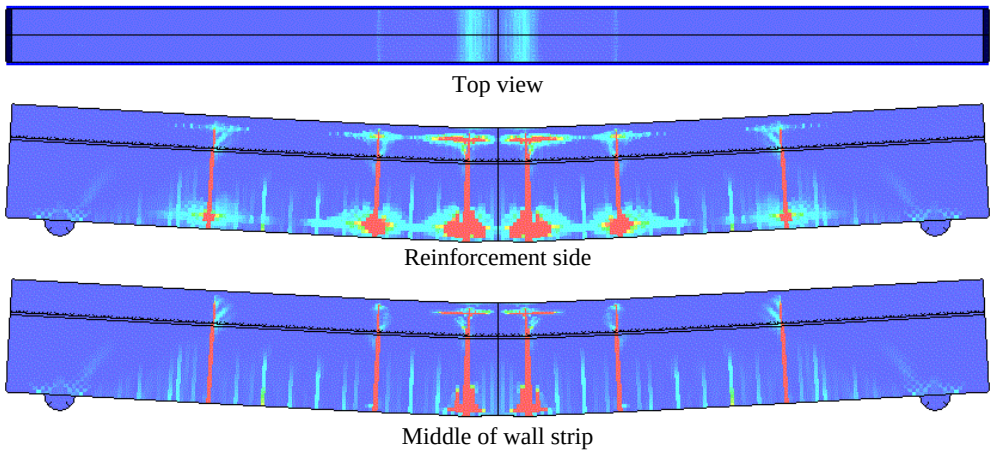

Fig. 8. Response of wall strip subjected to blast load at time of maximum mid-point deflection.

6.2 Fragment loading

In Fig. 9 the wall strip subjected to fragment loading is shown at time of maximum deflection. This is reached 13.3 ms after the fragments strike the wall, and amounts to 11.0 mm. As can be seen, the simulated damage caused by the multi-fragment impact is more complex than in the case of blast loading. The total damage consists of local damage on the front face, i.e. craters, scabbing cracks at the rear of the wall strip, direct shear cracks close to the supports, and bending cracks in the more central parts of the beam. When comparing Fig. 8 and Fig. 9, it can be seen that there are more bending cracks formed in the case of fragment impact than for blast loading, resulting in an increased energy-absorbing capacity since the reinforcement bars can yield at more locations. This means that also the load-bearing capacity may increase. However, the load-bearing capacity will at the same time be reduced by the decreased effective height due to the damage on the front face of the wall strip.

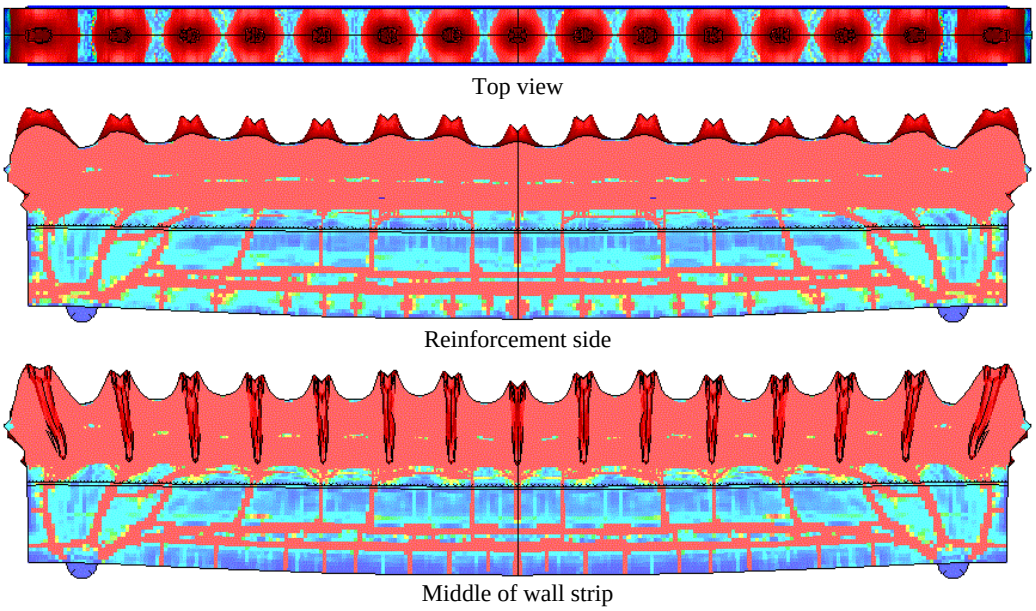

Fig. 9. Response of wall strip subjected to fragment impacts at time of maximum mid-point deflection.

To better distinguish the modes of damage and to better understand their evolution, the beam response is shown at different times, i.e. after 0.25, 0.6 and 9 ms, in Fig. 10. After 0.25 ms (Fig. 10a) the fragment impacts have caused craters on the front face, and the reflected stress wave has caused scabbing cracks at the rear of the wall strip. The scabbing effect was not expected in the simulations, but 2D simulations of fragment impact, taking the multiple simultaneous impact of fragments and also the strain-rate dependence of the tensile strength into account, confirm this behaviour; see [23]. However, in reality the two scabbing cracks probably represent one crack which appears at the level of tensile reinforcement and not in between the two reinforcement layers, as in this case.

Approximately 0.6 ms after the arrival of fragments, cracks propagate at the rear side of the wall strip, close to the supports, see Fig. 10b. These are probably direct shear cracks, as also observed in blast loading; see Section 6.1.

At time 9 ms, flexural cracks have started to propagate in the wall strip, as seen in Fig. 10c. These cracks form at the rear face of the target, but also at the level of the scabbing cracks, which indicates that the wall strip has started to act as two separate structures with sliding between the two separate planes formed by the horizontal scabbing cracks.

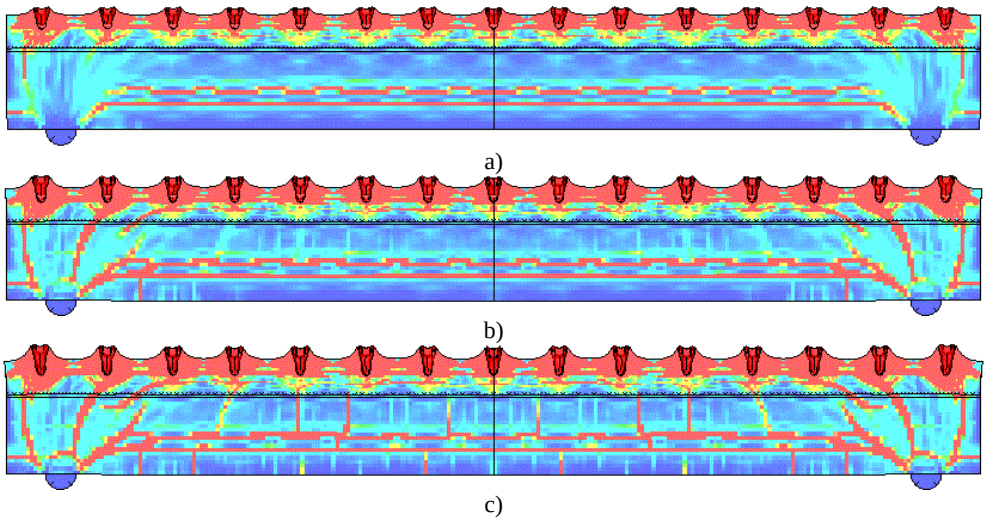

Fig. 10. Response of wall strip subjected to fragment impacts at time (a) 0.25 ms, (b) 0.6 ms and (c) 9 ms after time of fragment arrival, seen at section of reinforcement.

6.3 Combination of blast and fragment loading

The maximum mid-point deflection in case of simultaneous loading of blast and fragment is 85.7 mm and occurs after 33.4 ms. The response of the wall strip at time of maximum deflection is shown in Fig. 11. As the damage caused by the fragment impact, i.e. the front face craters and the scabbing cracks at the rear of the strip, appears very early (at less than 0.25 ms, as seen in Section 6.2) the damage in the case of combined, simultaneous loading is rather similar to the case of fragment loading alone. Due to the blast load, the deflection is larger and the damage in the concrete surrounding the reinforcement bars is more severe than in the case of fragment impact alone.

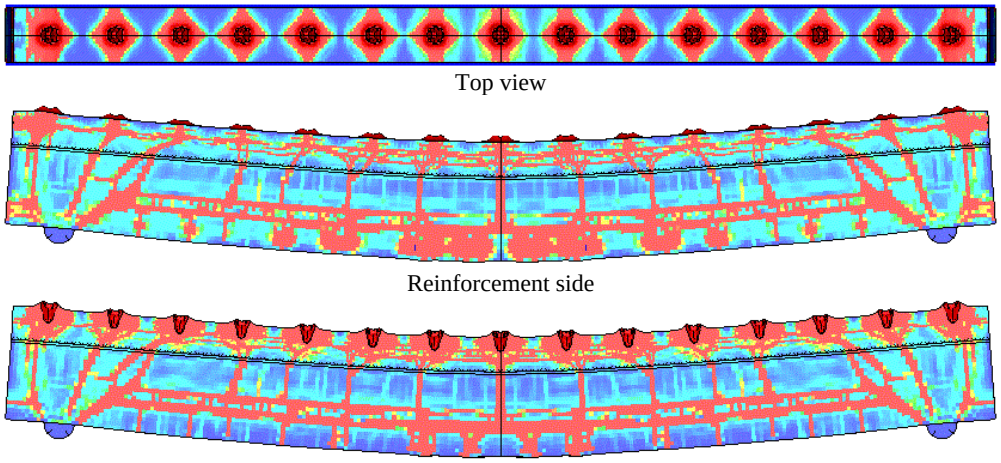

Fig. 11. Response of wall strip subjected to combined blast and fragment loading at time of maximum mid-point deflection.

Further, the diameters of the front face craters are reduced in case of combined loading compared to fragment loading alone. This can probably be explained by increased confinement effects. The blast wave causes pressure on the front face, acting perpendicular to the concrete surface, and gives a lateral pressure to the material compressed by the fragment penetration; schematically shown in Fig. 12. This reduction of front-face damage may lead to a higher load-bearing capacity than in the case with fragment impacts alone, but since the effective height of the wall strip is reduced, the load-bearing capacity is still affected. However, as in the case of fragment loading alone, the number of flexural cracks formed is larger than in the case of blast loading alone, allowing the reinforcement bars to yield at more locations, which may improve the load-bearing capacity.

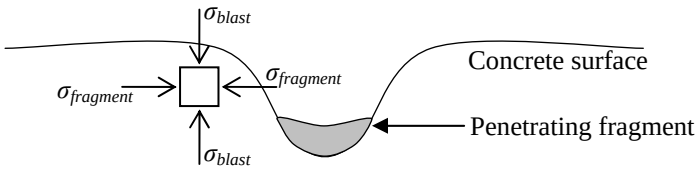

Fig. 12. Schematically shown confinement effects from blast loading, σ_{blast}, on concrete element compressed by $\sigma_{fragment}$ due to fragment penetration.

7 Comparison of mid-point deflections and velocities

In Fig. 13 the mid-point deflections of the three wall strips subjected to blast, fragment and combined loading, respectively, are shown. As seen, the mid-point deflection in the case of combined loading is larger than the sum of the deflections caused by blast and fragment loading separately, which indicates a synergy effect.

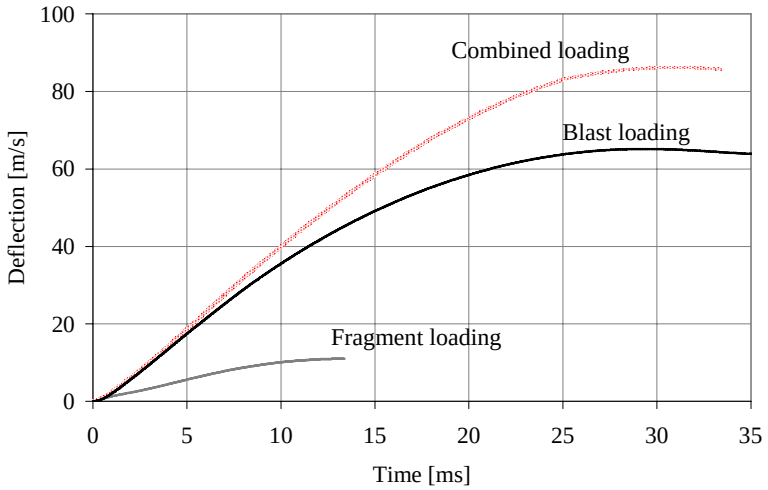

Fig. 13. Mid-point deflection of wall strip subjected to combined, blast and fragment loading from numerical simulations.

In Fig. 14 the mid-point velocities from the simulations with blast, fragment and combined loading are shown. The velocity for combined loading is first influenced by the fragment impact, but already after a fraction of a millisecond the velocity seems close to the velocity of the wall strip subjected to blast loading alone. After approximately 2 ms, the velocity for combined loading increases and exceeds the velocity for blast loading.

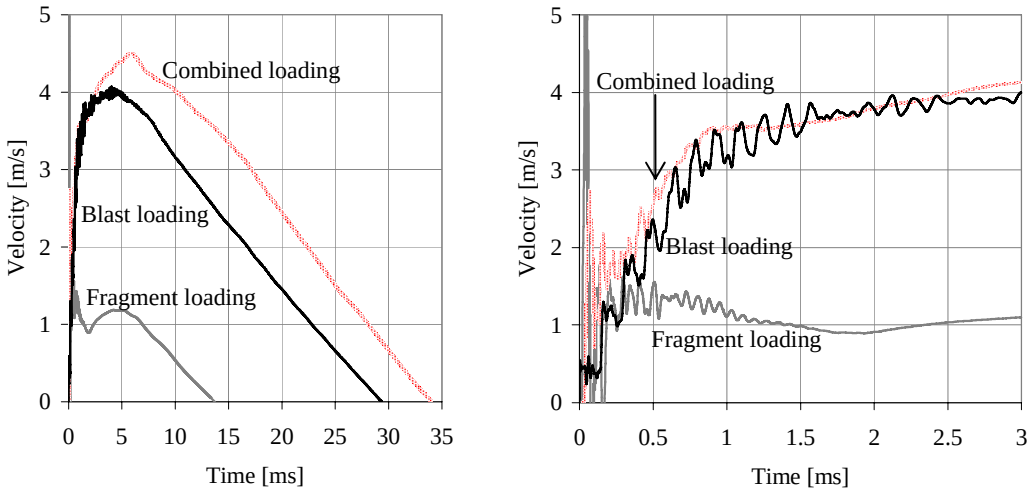

Fig. 14. Mid-point velocity of wall strip subjected to blast and fragment loading from numerical simulations.

In Table 1 the mid-point deflections estimated in the numerical analyses are presented together with results from SDOF analyses. Input parameters for the SDOF analyses are shown in Appendix A.
In the case of blast loading the estimations of the deflection made in SDOF and numerical simulations agree well. In the case of fragment loading the difference is larger, which probably can be explained by the limitations in the SDOF analyses to take into account e.g. the energy consumed during penetration and subsequent crushing of the concrete, the formation of many flexural cracks, and inertia effects, which may increase the load-bearing capacity. The results from the numerical simulation and the SDOF analysis differ also for combined loading. The difference is even larger than in the case of fragment loading and may be explained by magnification of the limitations already used as explanation for the case of fragment loading.

Table 1.
Mid-point deflections.

Load	$u_{AUTODYN}$ [mm]	u_{SDOF} [mm]
Blast	65.2	64.0
Fragment	11.0	13.9
Combined	85.7	139

8 Summary and conclusions

In blast loading, the elongation of the rear face of the wall strip is localised to a few cracks where yielding of the reinforcement takes place. In fragment loading, the flexural cracks to which the elongation of the reinforcement is localised are numerous, the energy-absorbing capacity of the wall strip may thus be increased.

In the simulations involving fragment loading, scabbing cracks formed due to the reflected stress wave. The appearance of these cracks were unexpected, but was confirmed with a 2D simulation study, indicating that the case of multi-fragment impact may lead to scabbing also when the single fragment impact does not. It may therefore be necessary to take this effect into account in design of protective structures. However, it is questionable whether the location and size of the scabbing cracks simulated are realistic.

Most damage caused by the fragment impact occurs within 0.2 ms after arrival, which is short compared to the response time of the element, indicating that in the case of combined loading the bearing capacity and the mid-point deflection of the wall strip may be highly influenced by the fragment impact since the structure thus loses part of its effective height.

The larger mid-point deflection of the wall strip subjected to blast loading, compared to the deflection in the case of fragment loading, was expected since the impulse from the blast was almost 2.5 times the impulse caused by the fragments.

The damage caused by combined loading is more severe than if adding the damages caused by the blast and fragment loading treated separately. The size of the front face craters, though, is an exception since these are larger in the case of fragment loading than in combined loading. It can be concluded that the mid-point deflection in combined loading (85.7 mm) is larger than the sum of mid-point deflections for blast and fragment loading treated separately (in total 76.2 mm), indicating a synergy effect in combined loading.

Acknowledgement

The work presented in this paper is done within the research project "Concrete structures subjected to blast and fragment impacts: dynamic behaviour of reinforced concrete", financially supported by the Swedish Rescue Services Agency. The authors would like to thank the members of the reference group for the project: Björn Ekengren, M.Sc., at the Swedish Rescue Services Agency, Morgan Johansson, Ph.D., at Reinertsen AB, and Joosef Leppänen, Ph.D., at FB Engineering AB.

References

[1] Girhammar UA. Brief review of Combined Blast and Fragment Loading Effects. Report C7:90. National Fortifications Administration, Eskilstuna, Sweden, 1990. 15 pp.

[2] ASCE. *Structural Design for Physical Security – State of the Practice*. Task committee: Conrath, E.J. *et al*., American Society of Civil Engineers, 1999. 264 pp.

[3] Ekengren B. Skyddsrum SR 06 (Shelter regulations SR06, in Swedish). Swedish Rescue Services Agency, Karlstad (Sweden), 2006. 113 pp.

[4] Johansson M. Structural Behaviour in Concrete Frame Corners of Civil Defence Shelters, Non-linear Finite Element Analyses and Experiments. Doctoral Thesis, Department of Structural Engineering, Concrete Structures, Göteborg (Sweden): Chalmers University of Technology, 2000. 220 pp.

[5] Leppänen J. Concrete Structures Subjected to Fragment Impacts, Dynamic Behaviour and Material Modelling. Doctoral Thesis, Department of Structural Engineering and Mechanics, Concrete Structures, Göteborg (Sweden): Chalmers University of Technology, 2004. 127 pp.

[6] Nyström U. Design with regard to explosions. Master's Thesis, Department of Civil and Environmental Engineering, Structural Engineering, Concrete Structures, Göteborg (Sweden): Chalmers University of Technology, 2006. 205 pp.

[7] Nyström U, Leppänen J. Numerical Studies of Projectile Impacts on Reinforced Concrete. In: Fan C, Chua HK (eds.). Proceedings of the Second International Conference on Design and Analysis of Protective Structures, Singapore (Singapore): Nanyang Technical University, 2006. p. 310-319.

[8] Johansson M, Laine L. Bebyggelsens motståndsförmåga mot extrem dynamisk belastning, Delrapport1: Last av luftstötvåg (The capacity of buildings to resist severe dynamic loading, Part 1: Blast wave loading, in Swedish). Swedish Rescue Services Agency, Karlstad (Sweden) 2007. 114 pp.

[9] Baker WE. Explosions in Air. University of Texas Press, Austin (TX, US), 1973. 285 pp.

[10] U.S. Army. Fundamentals of Protective Design for Conventional Weapons. Technical Manual TM 5-855-1. 1992. 271 pp.

[11] Forsén R, Nordström M. Damage to reinforced concrete slabs due to the combination of blast and fragment loading. (Reprint from the Second International Conference of Structures under Shock and Impact, Portsmouth, UK, 1992.) FOA report B 20101-2.6. National Defence Research Establishment, Sundbyberg (Sweden), 1992. 12 pp.

[12] Curran DR. Simple fragment size and shape distribution formulae for explosively fragmenting munitions. Int J Impact Engng 1997;20:197-208.

[13] DDESP. Methodologies for calculating primary fragment characteristics. Report No. DDESP TP 16, Department of Defence Explosives Safety Board, Alexandra, (U.S.), 2003. 53 pp.

[14] Mott NF, Linfoot EH. A Theory of Fragmentation. Ministry of Supply report No A.C.3348, January 1943.

[15] Mott NF. A Theory of Fragmentation of Shells and Bombs. Ministry of Supply report No A.C.4035, May 1943.

[16] Krauthammer T. Modern protective structures – Design, analysis and evaluation. Course notes for course Modern Protective Structures, State College (USA), July 2006. 412 pp.

[17] Gurney RW. The Initial Velocities of Fragments from Bombs, Shells and Grenades. US Army Ballistic Research Laboratory Report BRL 405, Aberdeen Providing Ground, MD, September 1943.

[18] Malvar LJ, Ross CA. Review of Strain Rate Effects for Concrete in Tension. ACI Mater J 1998;95(6):735-739.

[19] Bischoff PH, Perry SH. Compressive behaviour of concrete at high strain rates. Mater Struct 1991;24:425-450.

[20] Schuler H. Experimentelle und numerische Untersuchungen zur Schädigung von stoßbeanspruchtem Beton (in German). Doctoral Thesis, Universität der Bundeswehr München, Freiburg (Germany): Institut Kurzzeitdynamik, Ernst-Mach-Institut, 2004. 184 pp.

[21] Brara A, Klepaczko JR. Fracture energy of concrete at high loading rates in tension. Int J Impact Engng 2007;34(3):424-435.

[22] Weerheijm J, van Doormaal JCAM. Tensile failure of concrete at high loading rates: New test data on strength and fracture energy from instrumented spalling tests. Int J Impact Engng 2007;34(3):609-626.

[23] Nyström U. Concrete Structures Subjected to Blast and Fragment Impacts, Numerical Simulations of Reinforced and Fibre-reinforced Concrete. Licentiate thesis. Department of Civil and Environmental Engineering, Structural Engineering, Concrete Structures, Göteborg (Sweden): Chalmers University of Technology, 2008. 117 pp.
[24] Boverket. Boverkets Handbok för Betongkonstruktioner BBK 04, (Boverket's handbook for Concrete Structures BBK 04, in Swedish). Boverket, Karlskrona (Sweden), 2004. 271 pp.
[25] ConWep. Collection of conventional weapon effects calculations based on TM 5-855-1, Fundamentals of Protective Design for Conventional Weapons, U. S. Army Engineer Waterboys Experiment Station, Vicksburg (VA, USA), 1992.
[26] ANSYS AUTODYN User Manual, Version 11.0. Concord (CA, USA): Century Dynamics Inc., 2007. 528 pp.
[27] Magnusson J, Hansson H. Simuleringar av explosionsbelastade betongbalkar – en principstudie (Numerical simulations of concrete beams – a principal study, in Swedish). National Defence Research Establishment (FOI), FOI Report 1686--SE, Tumba (Sweden), 2005. 55 pp.
[28] Leppänen J. Splitterbelastad betong – Experiment och numeriska analyser (Fragment Impacts into Concrete – Experiments and Numerical Analyses, in Swedish). Department of Structural Engineering and Mechanics, Division of Concrete Structures, Chalmers University of Technology, Report no. 03:6, Göteborg (Sweden), 80 pp.
[29] Riedel W. Beton unter dynamischen lasten, meso. und makromechanische modelle und ihre parameter (in German). Doctoral Thesis, Universität der Bundeswehr München, Freiburg (Germany): Institut Kurzzeitdynamik, Ernst-Mach-Institut, 2000. 210 pp.
[30] AUTODYN Theory Manual, Revision 4.3. Concord (CA, USA), Century Dynamics Inc., 2005. 227 pp.
[31] Magnusson J, Hallgren M. High Performance Concrete Beams Subjected to shock Waves from Air Blast. National Defence Research Establishment (FOA) FOA report 00-01586-311--SE, Tumba (Sweden), 2000. 86 pp.
[32] Johansson M. Stötvågsutbreding i luft (Blast wave in air, in Swedish). Swedish Rescue Services Agency, Karlstad (Sweden), 2002. 60 pp.

Appendix A

Since an ideal-plastic material behaviour was assumed for the internal resistance of the SDOF system the equation of motion used to describe the movement of the mid-point in a simply supported beam, with mass, *M*, and length, *L*, subjected to a uniformly distributed load, *q(t)*, can be simplified to:

$$\frac{2}{3} M \ddot{u} + R = q(t) \cdot L \tag{1}$$

where $\ddot{u}$ is the mid-point acceleration of the beam [6].

When assuming an ideal-plastic material behaviour, the internal resistance, *R*, in Eq. 1 equals the maximum value of the load that the beam (or wall strip) can bear, i.e. $R=R_m$ given that the displacement $u \neq 0$. Before any displacement occurs ($u=0$), if the external load is smaller than the maximum load-bearing capacity ($P(t)<R_m$), the internal resistance equals the external load ($R=P(t)$). According to [10] the dynamic internal resistance can be estimated as 1.3 times the static internal resistance, possible explanation to this is given in [23]. The increase in load-bearing capacity in the case of dynamic loading, compared to static loading, is reported in [31] where blast-loaded concrete beams are studied, and supports the value used in [10] for increased internal resistance to dynamic loads. In numerical simulations of blast-loaded walls conducted and reported by Johansson [32] an increased load-bearing capacity was observed. [32] explained this by the appearance of large normal forces, which probably can be explained by inertia effects.

The dynamic internal resistance, R_m, is for a simply supported beam with uniformly distributed load thus calculated as:

$$R_m = 1.3 \frac{8 M_{Rd}}{L} \tag{2}$$

where M_{Rd} is the static moment capacity of the beam.

Conference Paper

Numerical Studies of Projectile Impacts on Reinforced Concrete
Nyström, U. and Leppänen, J.

Proceedings of the 2nd International Concference on Design and Analysis of Protective Structures 2006, 13-15 November 2006, Singapore, pp. 310-319

2nd Design and Analysis of Protective Structures 2006
13 – 15 November 2006, Singapore

Numerical Studies of Projectile Impacts on Reinforced Concrete

Ulrika Nyström[1], Joosef Leppänen[2]

Department of Civil and Environmental Engineering, Structural Engineering, Concrete Structures, Chalmers University of Technology, SE-412 96 Göteborg, Sweden
[1] (ulrika.nystrom@chalmers.se) and [2] (joosef.leppanen@chalmers.se)

Abstract

Numerical methods are an increasingly helpful tool in studies of protective structures such as projectile impacts on concrete structures. To predict the depth of penetration of the projectile, spalling and scabbing in reinforced concrete members, material models that take into account the strain rate effect, large deformations and triaxial stresses are required.

The aim of this paper is to increase the understanding of the phenomena of projectile impacts on reinforced concrete. Numerical studies of impact on reinforced and non-reinforced concrete members were carried out where the amount, spacing and dimensions of the reinforcement were varied, showing how these variations influence the depth of penetration and diameter of spalling of concrete.

The hydrocode AUTODYN with Lagrangian solver is used in the numerical simulations. For concrete, the material model takes into account pressure hardening, crack softening and strain rate effects. For the reinforcement, von Mises' material model is used.

It is well known that reinforcement prevents spalling and scabbing in concrete structures. For plain concrete, the depth of penetration depends mainly on the compressive strength of the concrete and the shape, material properties and impact velocity of the projectile. However, in reinforced concrete, the amount, spacing and location of the reinforcement are also important parameters. The depth of penetration decreases with increasing amount of the reinforcement, and if an increased steel bar diameter is used the depth of penetration, as well as the crater size, will decrease. Furthermore, reinforcement bars that are outside the damage zone have a minor effect on the depth of penetration and cratering.

Key words: Reinforced concrete; Projectile impact; Numerical simulation; Penetration; Spalling

1. Introduction

Reinforced concrete structures are effective as protective structures. Chalmers University of Technology is collaborating with the Swedish Rescue Services Agency to study the behaviour of concrete structures subjected to blast and fragment impacts; see Ekengren [1]. In earlier research, Johansson [2] studied the effect of blast waves in reinforced concrete structures, Leppänen [3] studied fragment impacts on plain concrete, and Nyström [4] studied design with regard to explosions. The long-term aim in the collaboration between Chalmers and the Swedish Rescue Services Agency is to study the combined effects of blast and fragment impacts on reinforced concrete structures.

However, this paper aims to contribute to increasing the general understanding of phenomena during projectile impacts on reinforced concrete members. Numerical studies of impact on non-reinforced and reinforced concrete members were carried out where the reinforcement ratio, spacing and bar diameter were varied in order to examine their effect on the depth of penetration and diameter of spalling of the concrete.

Resistance of reinforced concrete structures to projectile impact is a complex problem that has been a subject of both empirical and numerical studies. The depth of penetration of a projectile

impacting on a plain concrete target is mainly dependent on the projectile form (nose shape and diameter), material properties (mass, density), impact velocity and the concrete compressive strength. These parameters are often included in the empirical equations used to estimate the depth of penetration (in plain as well as in reinforced concrete). However, when reinforcement is cast into the concrete, the reinforcement ratio, spacing and bar diameter influence the resistance of the target and these parameters are not included in the empirical equations.

2. Numerical Models of Concrete and Reinforcement

The 2D numerical analyses were made in the software AUTODYN [5]. The constitutive model for concrete used in AUTODYN was the RHT model (Riedel, Hiermaier and Thoma), developed by Riedel [6]. The model, which consists of three yield surfaces, as shown in Fig. 1, includes pressure hardening, strain hardening and strain rate hardening. Furthermore, the deviatoric section of the surfaces depends on the third invariant.

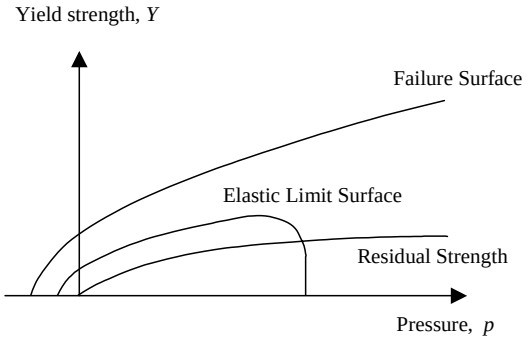

Fig. 1: The RHT model used for concrete; based on Riedel [6].

In AUTODYN a linear softening law is included to model the post-failure response of concrete in tension. Since concrete is a very brittle material and the strength decreases rapidly after the failure initiation, it would be more convenient to use a bi-linear softening law, for example the one proposed by Gylltoft [7]; see also Leppänen [3]. However, it has been assumed that the linear softening law is accurate enough to use in this work where the overall behaviour of the reinforced concrete is of interest.

In order to make a projectile stop, all its kinetic energy must be absorbed by either crushing the concrete target or creating plastic deformations in the steel. If a rigid projectile is used, all kinetic energy must be absorbed by the target, which will cause more damage to the target than if a deformable projectile is used. All parts made of steel (for example, reinforcement and projectile) were modelled with high rigidity with an elastic–perfectly plastic material model (von Mises), since the projectile does not impact on the reinforcement and therefore a less complex material model is sufficient.

3. Numerical Simulations of Projectile Impacting on Plain Concrete

The numerical simulations of reinforced concrete are compared to a numerical simulation of a plain concrete cylinder subjected to the same projectile impact. In order to verify the numerical model of the plain concrete target, the numerical results are compared to experimental results.

3.1. Experimental setup: projectile impact on plain concrete

In the experiment reported by Hansson [8], the 6.28 kg ogive-nose steel projectile used had a length of 225 mm, diameter of 75 mm, density of 7 830 kg/m3, bulk modulus of 159 GPa, shear modulus of 81.8 GPa, and yield stress of 792 MPa. The striking velocity was 485 m/s. The target was

a concrete cylinder, cast in a steel culvert, with a diameter of 1.6 m and a length of 2.0 m. The concrete cube strength was approximately 40 MPa (tested on a 150 mm cube). Two shots were fired at the same striking velocity, the first with support and the second without support at the opposite end of the target. The depth of penetration was 655 mm for the first shot and 660 mm for the second shot; the support at the backside of the target had a negligible effect on the depth of the penetration of the projectile. The diameter of the crater was approximately 800 mm.

3.2. Numerical mesh

It is well known that the size of the numerical mesh affects the results, and that the refined mesh extends the computational time. For dynamic loading, the mesh dependency is even more sensitive, since more terms are added in the constitutive models. To assess the mesh dependency, a common method is to halve the mesh size and compare the first coarse mesh with the finer mesh; and if the results differ only negligibly, the coarse mesh can be used. However, due to increased manipulation errors (caused by truncation, round-offs and insufficient numbers in input data) there is a risk of using a too fine mesh.

A good rule of thumb, according to Zucas and Scheffler [9], is to use at least three elements across the radius of the projectile in order to get reasonable results from numerical simulation of project impacts on concrete. Therefore, the mesh dependency was chosen with quadratic elements with a length of 10 mm (giving 3.75 elements across the radius of the projectile), after which the mesh was further refined to 5 mm elements. Further refined mesh was assumed not to give an increased accuracy worth the increased computational time. Here, only the final mesh used is presented.

The numerical mesh used for the plain concrete cylinder cast in a steel culvert is shown in Fig. 2. The model was axially symmetric, created by quadratic Lagrangian elements with an element length of 5 mm, totalling 400 x 160 elements. Full interaction between the concrete and the steel culvert was assumed.

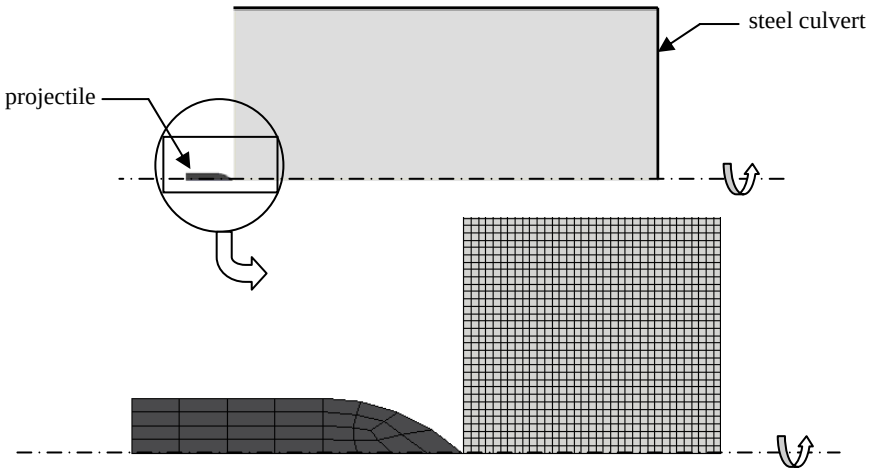

Fig. 2: Numerical mesh of projectile impacting on plain concrete cast in steel culvert.

3.3. Analyses with AUTODYN

For simplicity the same material parameters were used for all steel parts; see Section 3.1. The material parameters used in the concrete model were either determined by Leppänen [10] or default values of concrete from the material library in AUTODYN except for the erosion strain. The erosion strain coefficient, used for the Lagrangian solver technique in order to overcome problems with distortion and grid tangling due to large deformations of the mesh, was here calibrated by parametric studies so that the depth of penetration would agree with the experimental results. All material parameters used in the RHT model are shown in Table 1. Details of the material parameters shown in Table 1 are described in AUTODYN.

Table 1: Input data for concrete: RHT model, constitutive model.

Parameter	Value	Comments
Shear Modulus [kPa]	$1.433 \cdot 10^7$	a
Compressive Strength f_c [kPa]	$3.38 \cdot 10^4$	a
Tensile Strength f_t/f_c	0.078	a
Shear Strength f_s/f_c	0.18	b
Intact Failure Surface Constant *A*	2	c
Intact Failure Surface Exponent *N*	0.7	c
Tens./Compr. Meridian Ratio	0.6805	b
Brittle to Ductile Transition	0.0105	b
G(elastic)/G(elastic-plastic)	2	b
Elastic Strength/f_t	0.7	b
Elastic Strength/f_c	0.53	b
Fractured Strength Constant *B*	1.5	c
Fractured Strength Exponent *M*	0.7	c
Compressive Strain Rate Exponent α	0.032	b
Tensile Strain Rate Exponent δ	0.025	d
Maximum Fracture Strength Ratio	$1 \cdot 10^{20}$	b
Use CAP on Elastic Surface	Yes	b
Damage Constant *D1*	0.04	b
Damage Constant *D2*	1	b
Minimum Strain to Failure	0.01	b
Residual Shear Modulus Fraction	0.13	b
Tensile Failure	Hydro (P_{min})	b
Erosion Strain/Instantaneous Geometric Strain	1.5	e

a. Calculated according to CEB-FIB Model Code 1990 [11].
b. Default value in AUTODYN material library for concrete with compressive strength of 35 MPa.
c. Determined by Leppänen [3, 10] based on model proposed by Attard and Setunge [12].
d. Calibrated by parameter studies; see Leppänen [10]. This parameter cannot give a realistic description of the dynamic increase factor for concrete in tension.
e. Calibrated by parameter studies.

In AUTODYN an equation of state (EOS) is required beside the constitutive model in order to complete the description of continuum. Default values from the material library in AUTODYN were used for the material parameters describing the EOS for concrete, except for the density which was assumed to be 2 400 kg/m3. Details of the parameters shown in Table 2 are described in AUTODYN.

Table 2: Input data for concrete: equation of state (*EOS*).

Parameter	Value
Reference Density [g/cm^3]	2.75
Porous Density [g/cm^3]	2.4
Porous Sound Speed [m/s]	2920
Initial Compaction Pressure [kPa]	$2.33 \cdot 10^4$
Solid Compaction Pressure [kPa]	$6 \cdot 10^6$
Compaction Exponent	3
Solid *EOS*	Polynomial
Bulk Modulus *A1* [kPa]	$3.527 \cdot 10^7$
A2 [kPa]	$3.958 \cdot 10^7$
A3 [kPa]	$9.04 \cdot 10^6$
B0	1.22
B1	1.22
T1	$3.527 \cdot 10^7$
T2	0
Reference Temperature [K]	300
Specific Heat [J/kgK]	654
Thermal Conductivity [J/mKs]	0
Compaction Curve	Standard

3.4. Results

The depth of penetration in the numerical simulation was 654 mm and the diameter of the crater was 580 mm. It is to be observed that the measurement of the crater diameter is ambiguous. Here it was measured as the diameter of the fully damaged outermost layer; see Fig. 3, where the white areas are undamaged concrete and black indicates fully damage concrete.

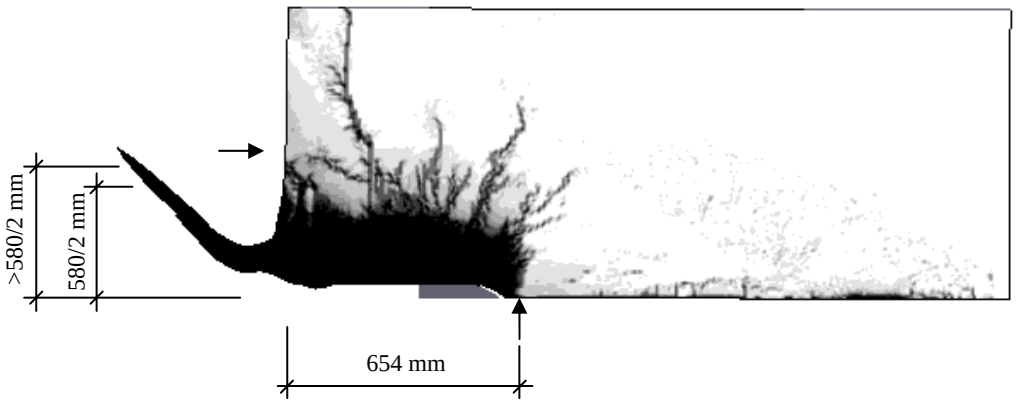

Fig. 3: Computed cratering and depth of penetration in plain concrete cylinder.
The arrows show the crater diameter and depth of penetration from experiments reported by Hansson [8].

Even though the depth of penetration agrees very well with the experimental results, the crater diameter should have been larger and the bottom of the crater should have been narrower in order to agree with the experimental results.

4. Numerical Simulations of Projectile Impacting on Reinforced Concrete

4.1. Numerical mesh

To study the effect of projectile impact on reinforced concrete, various sets of reinforcement arrangements were modelled inside the concrete cylinder. The reinforcement was modelled as reinforcement rings, with different dimensions and spacing (in both horizontal and vertical direction), cast into the concrete; see Fig. 4 and Fig. 5.

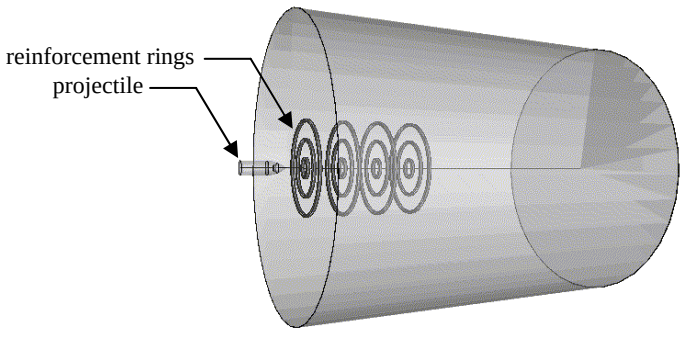

Fig. 4: Schematic figure of reinforcement arrangement (2D model rotated 360 degrees).

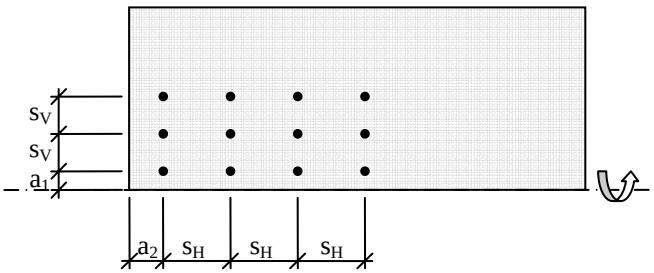

a_1 – vertical distance from impact point to the closest reinforcement ring
a_2 – horizontal distance from impact point to the closest reinforcement ring
s_H – spacing in horizontal direction
s_V – spacing in vertical direction

Fig. 5: Reinforcement arrangement.

The same numerical mesh as for the plain concrete cylinder was used here, and the reinforcement was modelled with 2 elements across the radius of the bars; see Fig. 6. Full interaction between the reinforcement and the concrete was assumed.

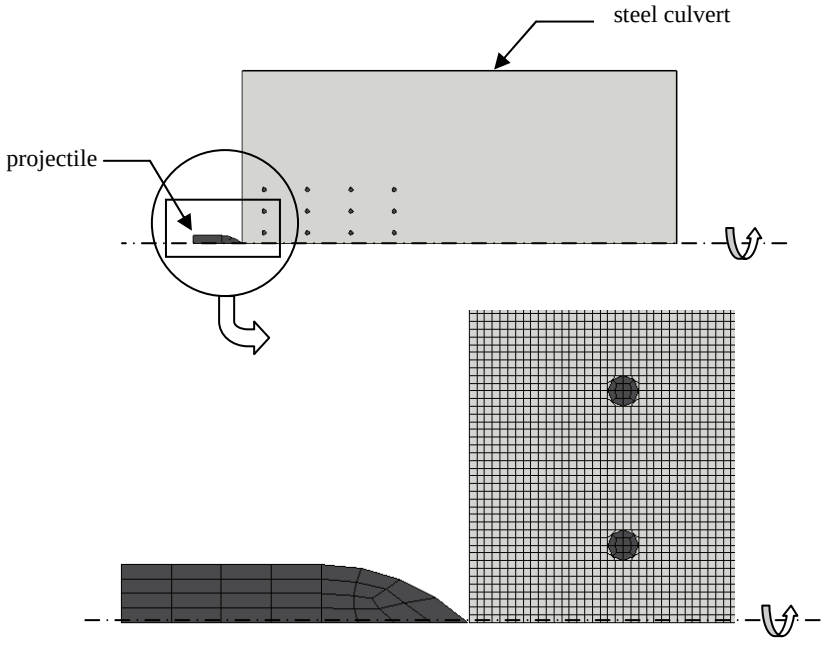

Fig. 6: Numerical mesh of projectile impacting on reinforced concrete cast in steel culvert.

4.2. Parametric Studies

4.2.1. Effect of amount of reinforcement

In order to examine the effect of the amount and position of the reinforcement, ten numerical simulations were made, using the same reinforcement bars and spacing between them, after which the depth of penetration and crater diameter were measured; see Table 3. The maximum decrease of the depth of penetration, in relation to the plain concrete cylinder, achieved in this study was about 15%. In one case the depth of penetration in the reinforced concrete exceeded the depth of penetration measured in the plain concrete, but the crater diameter was smaller; see Fig. 3 and no. 10 in Table 3. This means that more energy was consumed to crush the concrete in the longitudinal direction and less in the radial direction compared to the non-reinforced case. When a certain amount of reinforcement was used, the depth of penetration and the crater diameter decreased insignificantly, even though more reinforcement layers were modelled inside the concrete cylinder; see 1-3 and 6-8 in Table 3 and Fig. 7.

Table 3: Depth of penetration and crater diameter for various amounts of reinforcement rings.

No	ϕ_{bar} [mm]	a_1 [mm]	s_V [mm]	$\#_V$ [a]	a_2 [mm]	s_H [mm]	$\#_H$ [b]	Depth of penetration [mm]	Crater diameter[c] [mm]
0	-	-	-	0	-	-	0	654	580
1	20	50	100	5	50	100	8	555	490
2	20	50	100	4	50	100	7	555	480
3	20	50	100	4	50	100	6	560	520
4	20	50	100	4	50	100	5	600	470
5	20	50	100	4	50	100	4	605	460
6	20	50	100	3	50	100	7	563	530
7	20	50	100	2	50	100	7	562	480
8	20	50	100	1	50	100	7	570	490
9	20	50	100	3	50	100	6	560	500
10	20	150	100	3	50	100	6	670	480

a. Number of reinforcement rings in vertical direction.
b. Number of reinforcement rings in horizontal direction.
c. See comments in Section 3.4.

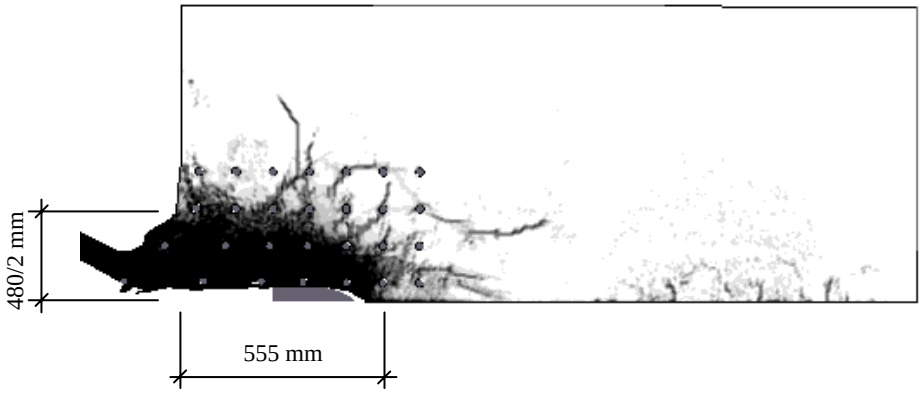

a)

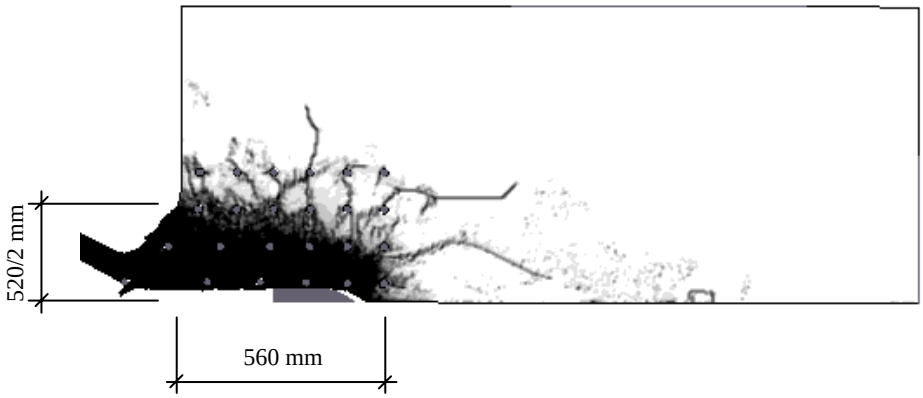

b)

Fig. 7: Damage of concrete cylinder with *(a)* 4 x 7 and *(b)* 4 x 6 reinforcement rings, respectively.

4.2.2. Effect of reinforcement spacing

The effect of the reinforcement spacing was studied by doubling the spacing in the vertical and horizontal directions, one at a time, and finally in both directions at the same time; see Table 4. If the spacing was doubled in one direction, no matter whether it was in the horizontal or the vertical direction, the depth of penetration increased by approximately 13% while the crater diameter was relatively unaffected. When the spacing was doubled in both directions, the depth of penetration increased from 560 mm to 660 mm, even deeper than for the plain concrete cylinder; see Fig. 3.

Table 4: Depth of penetration and crater diameter for various spacing between the reinforcement rings.

No	ϕ_{bar} [mm]	a_1 [mm]	s_V [mm]	$\#_V$ [a]	a_2 [mm]	s_H [mm]	$\#_H$ [b]	Depth of penetration [mm]	Crater diameter[c] [mm]
9	20	50	100	3	50	100	6	560[d]	500[d]
11	20	100	200	3	50	100	6	630	450
12	20	50	100	3	100	200	6	635	490
13	20	100	200	3	100	200	6	660	510

a. Number of reinforcement rings in vertical direction.
b. Number of reinforcement rings in horizontal direction.
c. See comments in Section 3.4.
d. The same data as in Table 3.

4.2.3. Effect of dimension of reinforcement

In order to examine the influence of the reinforcement bar diameter, two different dimensions were used in the numerical studies, 10 and 20 mm; see Table 5. Different numbers of reinforcement layers were also used in order to see if the possible influence differed when changing the amount of reinforcement. The results show that the decrease of bar diameter affected the depth of penetration, which increased by approximately 10 to 15% when the diameter was halved, and the crater diameter increased by 10 to 13 % or, in one case, not at all. When using bars with 10 mm diameter the depth of penetration is almost unaffected compared to the unreinforced case; see Table 3.

Table 5: Depth of penetration and crater diameter for various bar diameters.

No	ϕ_{bar} [mm]	a_1 [mm]	s_V [mm]	$\#_V$ [a]	a_2 [mm]	s_H [mm]	$\#_H$ [b]	Depth of penetration [mm]	Crater diameter[c] [mm]
14	10	50	100	5	50	100	8	640	540
1	20	50	100	5	50	100	8	555 [d]	490[d]
15	10	50	100	4	50	100	7	640	640
2	20	50	100	4	50	100	7	555 [d]	480[d]
16	10	50	100	4	50	100	5	660	470
4	20	50	100	4	50	100	5	600 [d]	470 [d]

a. Number of reinforcement rings in vertical direction
b. Number of reinforcement rings in horizontal direction
c. See comments in Section 3.4
d. The same data as in Table 3.

5. Discussion

The amount of fully damaged concrete was greater in the plain concrete cylinder than in the reinforced concrete cylinders. A probable explanation is that some of the energy applied to the reinforced target is absorbed when deforming the reinforcement bars. In the reinforced concrete cylinders, more and finer cracks, which also are more concentrated around the crater, have formed than in the plain concrete target. This is probably because the crack formation also absorbs energy, indicating another reason why the projectile caused less damage in the reinforced concrete cylinders than in the plain concrete cylinder.

The improved resistance of the concrete cylinder when reinforced with steel rings can plausibly be explained by the increased confinement due to the reinforcement. This resistance would probably not be achieved if straight reinforcement bars were cast into the concrete instead of the steel rings, even if the same amount of reinforcement had been used. Numerical studies on penetration of reinforced concrete targets, where straight bars have been used, indicate that the presence of reinforcement does not increase the penetration resistance itself as long as the projectile does not strike the steel, Huang *et al* [13].

There seems to be an effective length (longitudinal direction) within which the reinforcement affects the depth of penetration and the crater diameter. If reinforcement rings are placed outside this

effective length, they have little or no effect on these variables. The number of reinforcement layers in the radial direction seems to have less influence on the depth of penetration and crater diameter than does the distance from the symmetry axis of the cylinder to the first layer of reinforcement rings in the radial direction. A probable explanation is that the confinement effect decreases with increasing distance.

Further, decreasing the diameter of the bars or increasing the spacing between them has a negative effect on the depth of penetration. The crater diameter seems to be less influenced by these parameters. Since thinner or more widely spaced bars mean a lower proportion of steel in the volume around the impact area, there should be less resistance to compression by the concrete giving way beneath the projectile, resulting in deeper penetration.

6. Conclusions

It is clear that the amount and position of reinforcement influence the depth of penetration and crater size. In this study, the reinforcement has a local effect; as long as the reinforcement is inside the damage zone and a sufficient amount of reinforcement is used, the depth of penetration and crater diameter are affected noticeably.

The distance between the centre line of the cylinder and the first layer of reinforcement is an important factor for the depth of penetration, which increases with an increasing distance.

When the spacing between the reinforcement bars was increased in one direction, the depth of penetration increased; and when the spacing was increased in both vertical and horizontal directions, the depth of penetration increased even more. However, the spacing has a minor effect on the crater diameter.

The depth of penetration is also affected by the bar size. A decreased reinforcement bar diameter resulted in both increased depth of penetration and crater diameter.

Acknowledgement

For the research presented in this paper financial support was obtained from the Swedish Rescue Services Agency. The authors would like to thank Professor Kent Gylltoft, at Chalmers, and the members of the reference group for the project “Concrete structures subjected to blast and fragment impacts: dynamic behaviour of reinforced concrete”: Björn Ekengren, M.Sc., at the Swedish Rescue Services Agency, and Morgan Johansson, Ph.D., at Reinertsen AB.

References

[1] Ekengren, B., *Skyddsrum, SR 06*, (*Civil Defence Shelters*, in Swedish), B54-141/06, Swedish Rescue Services Agency, Karlstad, Sweden, 2006. 114pp.

[2] Johansson, M., *Structural behaviour in concrete frame corners of civil defence shelters*, Doctoral Thesis, Department of Structural Engineering, Division of Concrete Structures, Chalmers University of Technology, Göteborg, Sweden, 2000. 204pp.

[3] Leppänen, J., *Concrete structures subjected to fragment impacts: Dynamic behaviour and material modelling*, Doctoral Thesis, Department of Structural Engineering and Mechanics, Division of Concrete Structures, Chalmers University of Technology, Göteborg, Sweden, 2004. 61pp.

[4] Nyström, U., *Design with regard to explosions*, Master's Thesis, Department of Civil and Environmental Engineering, Division of Structural Engineering, Concrete Structures, Chalmers University of Technology, Göteborg, Sweden, 2006. 205pp.

[5] AUTODYN Manuals; v6.1, Century Dynamics Inc., 2005.
[6] Riedel, W., *Beton under dynamischen Lasten Meso- und makromechanische Modelle und ihre Parameter* (in German), Doctoral Thesis, Fakultät für Bauingenieur- und Vermessungswesen, Universität der Bundeswehr München, Freiburg, Germany, 2000. 210pp.
[7] Gylltoft, K., *Fracture mechanics models for fatigue in concrete structures*, Doctoral Thesis, Department of Structural Engineering, Luleå Univeristy of Technology, Luleå, Sweden, 1983. 210pp.
[8] Hansson, H., *Numerical simulation of concrete penetration*, FOA-R-98-00816-311--SE, Defence research establishment, Weapons and Protection Division, Tumba, Sweden, 1998. 17pp.
[9] Zukas, J.A. and Scheffler, D.R., *Practical aspects of numerical simulation of dynamic events: Effects of meshing*, International Journal of Impact Engineering, Vol.24, No.9, pp.925-945, 2000.
[10] Leppänen, J., *Dynamic behaviour of concrete structures subjected to blast and fragment impacts*, Licentiate Thesis, Department of Structural Engineering, Division of Concrete Structures, Chalmers University of Technology, Göteborg, Sweden, 2002. pp.71.
[11] *CEB-FIP model code 1990. Design code*, 1993, T. Telford, Lausanne; Switzerland 1993. 437pp.
[12] Attard, M.M. and Setunge, S., *Stress-strain relationship of confined and unconfined concrete*, ACI Materials Journal, Vol.93, No.5, pp.432-442, September-October 1996.
[13] Huang, F., Wu, H., Jin, Q. and Zhang, Q., *A numerical simulation on the perforation of reinforced concrete targets*, International Journal of Impact Engineering, Vol.32, pp.173-187, 2005.

Licentiate Theses and Doctoral Theses, Concrete Structures,

Chalmers University of Technology, 1990-

90:1 Stig Öberg: Post Tensioned Shear Reinforcement in Rectangular RC Beams. Publication 90:1. Göteborg, April 1990. 603 pp. (No. 1021). Doctoral Thesis.

90:2 Johan Hedin: *Långtidsegenskaper hos samverkanskonstruktioner av stål och betong (Long Time Behaviour of Composite Steel Concrete Structures).* Publication 90:2. Göteborg, August 1990. 53 pp. (No. 1079). Licentiate Thesis.

92:1 Björn Engström: *Ductility of Tie Connections in Precast Structures*. Publication 92:1. Göteborg, October 1992. 368 pp. (Nos. 936, 999, 1023, 1052). Doctoral Thesis.

93:1 Mario Plos: *Shear Behaviour in Concrete Bridges - Full Scale Shear Test. Fracture Mechanics Analyses and Evaluation of Code Model*. Publication 93:1. Göteborg, April 1993. 70 pp. (Nos. 1088, 1084). Licentiate Thesis.

93:2 Marianne Grauers: *Composite Columns of Hollow Steel Sections Filled with High Strength Concrete*. Publication 93:2. Göteborg, June 1993. 140 pp. (No. 1077). Doctoral Thesis.

93:4 Li An: *Load Bearing Capacity and Behaviour of Composite Slabs with Profiled Steel Sheet*. Publication 93:4. Göteborg, September 1993. 134 pp. (No. 1075). Doctoral Thesis.

93:5 Magnus Åkesson: *Fracture Mechanics Analysis of the Transmission in Zone in Prestressed Hollow Core Slabs*. Publication 93:5. Göteborg, November, 1993. 64 pp. (No 1112). Licentiate Thesis.

95:1 Christina Claeson: *Behavior of Reinforced High Strength Concrete Columns*. Publication 95:1. Göteborg, June 1995. 54 pp. (No. 1105). Licentiate Thesis.

95:2 Karin Lundgren: *Slender Precast Systems with Load-Bearing Facades*. Publication 95:2. Göteborg, November 1995. 60 pp. (No. 1098). Licentiate Thesis.

95:3 Mario Plos: *Application of Fracture Mechanics to Concrete Bridges. Finite Element Analysis and Experiments*. Publication 95:3. Göteborg, November 1995. 127 pp. (Nos. 1067, 1084, 1088, 1106). Doctoral Thesis.

96:1 Morgan Johansson: *New Reinforcement Detailing in Concrete Frame Corners of Civil Shelters. Non-linear Finite Element Analyses and Experiments*. Publication 96:1. Göteborg, November 1996. 77 pp. (No. 1106). Licentiate Thesis.

96:2 Magnus Åkesson: *Implementation and Application of Fracture Mechanics Models for Concrete Structures*. Publication 96:2. Göteborg, November 1996. 159 pp. (No. 1112). Doctoral Thesis.

97:1 Jonas Magnusson: *Bond and Anchorage of Deformed Bars in High-Strength Concrete*. Publication 97:1. Göteborg, November 1997. 234 pp. (No. 1113). Licentiate Thesis.

98:1 Christina Claeson: *Structural Behavior of Reinforced High-Strength Concrete Columns*. Publication 98:1. Göteborg 1998. 92 pp + I-IV, 75 pp. (No. 1105). Doctoral Thesis.

99:1 Karin Lundgren: *Three-Dimensional Modelling of Bond in Reinforced Concrete. Theoretical Model, Experiments and Applications*. Publication 99:1. Göteborg, November 1999. 129 pp. (No. 37). Doctoral Thesis.

00:1 Jonas Magnusson: *Bond and Anchorage of Ribbed Bars in High-Strength Concrete*. Publication 00:1. Göteborg, February 2000. 300 pp. (No. 1113). Doctoral Thesis.

00:2 Morgan Johansson: *Structural Behaviour in Concrete Frame Corners of Civil Defence Shelters*. Publication 00:2. Göteborg, March 2000. 220 pp. (No. 1106). Doctoral Thesis.

00:3 Rikard Gustavsson: *Static and Dynamic Finite Element Analyses of Concrete Sleepers*. Publication 00:3. Göteborg, March 2000. 58 pp. (No. 41). Licentiate Thesis.

00:4 Mathias Johansson: *Structural Behaviour of Circular Steel-Concrete Columns. Non-linear Finite Element Analyses and Experiments*. Publication 00:4. Göteborg, March 2000. 64 pp. (No. 48). Licentiate Thesis.

01:3 Gunnar Holmberg: *Fatigue of Concrete Piles of High Strength Concrete Exposed to Impact Load*. Publication 01:3. Göteborg, August 2001. 69 pp. (No. 55). Licentiate Thesis.

02:1 Peter Harryson: *Industrial Bridge Construction – merging developments of process, productivity and products with technical solutions*. Publication 02:1. Göteborg, January 2002. 90 pp. (No. 34). Licentiate Thesis.

02:2 Ingemar Löfgren: *In-situ concrete building systems – developments for industrial constructions*. Publication 02:2. Göteborg, March 2002. 125 pp. (No. 35). Licentiate Thesis.

02:4 Joosef Leppänen: *Dynamic Behaviour of Concrete Structures subjected to Blast and Fragment Impacts.* Publication 02:4. Göteborg, April 2002. 78 pp. (No. 31). Licentiate Thesis.

02:5 Peter Grassl: *Constitutive Modelling of Concrete in Compression*. Publication 02:5. Göteborg, May 2002. 95 pp. (No. 37). Licentiate Thesis.

02:6 Rikard Gustavson: *Structural Behaviour of Concrete Railway Sleepers*. Publication 02:6. Göteborg, September 2002. 180 pp. (No. 32). Doctoral Thesis.

02:8 Mathias Johansson: *Composite Action and Confinement Effects in Tubular Steel-Concrete Columns*. Publication 02:8. Göteborg, November 2002. 173 pp. (No. 33). Doctoral Thesis.

03:1 Per-Ola Svahn: *Impact-Loaded Concrete Piles – Theoretical and experimental study of load effects and capacity*. Publication 03:1. Göteborg, May 2002. 99 pp. (No. 38). Licentiate Thesis.

04:3 Peter Grassl: *Plasticity and Damage Mechanics for Modeling Concrete Failure*. Publication 04:3. Göteborg, September 2004. 159 pp. Doctoral Thesis.

04:4 Joosef Leppänen: *Concrete Structures Subjected to Fragment Impacts – Dynamic Behaviour and Material Modelling*. Publication 04:4. Göteborg, October 2004. 125 pp. (No. 31). Doctoral Thesis.

2005 Helen Broo: *Shear and Torsion Interaction in Prestressed Hollow Core Slabs.* Lic 2005:2. Göteborg 2005. 83 pp. Licentiate Thesis.

2005 Per-Ola Svahn: *Dynamic Behaviour of Reinforced Concrete Structures: Analyses with a Strong Discontinuity Approach.* Ny serie nr 2366. Göteborg 2005. 159 pp. Doctoral Thesis.

2005 Ingemar Löfgren: *Fibre-reinforced Concrete for Industrial Construction – a fracture mechanics approach to material testing and structural analysis.* Ny serie nr. 2378. Göteborg 2005. pp 243. Doctoral Thesis.

2006 Rasmus Rempling: *Constitutive Modelling of Concrete Subjected to Tensile Monotonic and Cyclic Loading*. Lic 2006:4. Göteborg 2006. 59 pp. Licentiate Thesis.

2008 Anette Jansson: *Fibres in Reinforced Concrete Structures – analysis, experiments and design*. Lic 2008:3. Göteborg 2008. 84 pp. Licentiate Thesis.